UNIVERSIDADE FEDERAL DO CEARÁ
CENTRO DE TECNOLOGIA
DEPARTAMENTO DE ENGENHARIA HIDRÁULICA E AMBIENTAL
PROGRAMA DE PÓS-GRADUAÇÃO EM ENGENHARIA CIVIL

SOFIA MIDAUAR GONDIM ROCHA

ASSESSMENT OF THE SPATIAL DISTRIBUTION OF LAKE EVAPORATION WITH 3D HYDRODYNAMIC MODELING

FORTALEZA
2022

SOFIA MIDAUAR GONDIM ROCHA

ASSESSMENT OF THE SPATIAL DISTRIBUTION OF LAKE EVAPORATION WITH 3D HYDRODYNAMIC MODELING

Dissertação apresentada ao Programa de Pós-Graduação em Engenharia Civil da Universidade Federal do Ceará, como requisito parcial à obtenção do título de Mestre em Engenharia Civil. Área de concentração: Recursos Hídricos.

Advisor: Prof. Iran Eduardo Lima Neto, PhD.
Co-advisor: Dr. Ernesto Molinas.

FORTALEZA
2022

Dados Internacionais de Catalogação na Publicação
Universidade Federal do Ceará
Biblioteca Universitária
Gerada automaticamente pelo módulo Catalog, mediante os dados fornecidos pelo(a) autor(a)

R576a Rocha, Sofia Midauar Gondim.
ASSESSMENT OF THE SPATIAL DISTRIBUTION OF LAKE EVAPORATION WITH 3D HYDRODYNAMIC MODELING / Sofia Midauar Gondim Rocha. – 2022.
95 f. : il. color.

Dissertação (mestrado) – Universidade Federal do Ceará, Centro de Tecnologia, Programa de Pós-Graduação em Engenharia Civil: Recursos Hídricos, Fortaleza, 2022.
Orientação: Prof. Dr. Iran Eduardo Lima Neto.
Coorientação: Prof. Dr. Ernesto Molinas.

1. Delft3D. 2. Evaporation. 3. Hydrodynamics. 4. Remote sensing. I. Título.
CDD 627

SOFIA MIDAUAR GONDIM ROCHA

ASSESSMENT OF THE SPATIAL DISTRIBUTION OF LAKE EVAPORATION WITH 3D HYDRODYNAMIC MODELING

Dissertação apresentada ao Programa de Pós-Graduação em Engenharia Civil da Universidade Federal do Ceará, como requisito parcial à obtenção do título de Mestre em Engenharia Civil. Área de concentração: Recursos Hídricos.

Aprovada em: 11/03/2022

BANCA EXAMINADORA

____
Prof. Iran Eduardo Lima Neto, PhD (Advisor)
Universidade Federal do Ceará (UFC)

____
Dr. Ernesto Molinas (Co-advisor)
Acquatool Consultoria S/S LTDA

____
Prof. Dr. Francisco de Assis de Souza Filho
Universidade Federal do Ceará (UFC)

____
Prof. Sergio Koide, PhD
Universidade de Brasília (UnB)

A Deus.

Aos meus pais, Maria e Maia.

ACKNOWLEDGMENTS

Agradeço inicialmente à minha família, em especial aos meus pais, Maria e Maia, aos meus irmãos, Bruno e Vitor, e ao meu melhor amigo e companheiro, Juan. Obrigada por terem me apoiado incondicionalmente, mesmo nos momentos mais difíceis, e por terem sido Fortaleza para mim durante esses dois anos de mestrado concomitante a uma pandemia.

Em seguida, dedico este documento à minha dupla Luísa Ciríaco, que me acompanha e incentiva desde a preparação para a prova de ingresso neste curso. Também não poderia deixar de agradecer aos amigos João e Lara, por deixarem o caminho mais leve. Vocês todos são parte desta conquista.

Sou imensamente grata ao meu orientador, professor Iran, que tenho a sorte de ter como guia há tantos anos. Obrigada por todo o pronto suporte. Agradeço também ao meu co-orientador, Ernesto, parte chave deste trabalho em sua presente forma.

Por fim, agradeço ao Ítalo Sampaio pelas valiosas contribuições, as quais possibilitaram o pleno desenvolvimento do estudo comparativo realizado. A todos que, direta ou indiretamente, se fizeram presentes em minha vida neste intenso período de mestrado, o meu muito obrigada.

Este estudo foi financiado pelo Conselho Nacional de Desenvolvimento Científico e Tecnológico – CNPq, por meio de bolsa de mestrado.

“Via graça em tudo que fazia, ao contrário de só querer fazer o que via graça.” (Carla Madeira em *Tudo é Rio*, 2014).

RESUMO

Em regiões áridas e semiáridas as taxas evaporativas são uma importante perda hídrica. Essa situação é ainda mais relevante no nordeste brasileiro, visto que esta é uma das regiões semiáridas mais populosas do mundo. Em uma realidade de baixa disponibilidade hídrica, avançar no conhecimento das complexidades envolvidas nas perdas de água superficiais junto aos processos que ocorrem na coluna d'água dos reservatórios é de extrema importância. O objetivo deste estudo é calibrar a estrutura térmica do reservatório Pentecoste, localizado no semiárido brasileiro, além de avaliar a variabilidade das taxas evaporativas na superfície utilizando o modelo tridimensional Delft3D-FLOW. Junto a isso, os resultados da espacialização da evaporação obtidos com o modelo 3D são comparados com aqueles estimados por uma técnica de sensoriamento remoto (SR). Os resultados da calibração mostraram uma reprodução precisa da variação do nível d'água (r^2 de 0.997), junto a resultados satisfatórios para a estrutura térmica do reservatório (métricas para toda a coluna d'água: MAE = 0.539 °C, RMSE = 0.572 °C e NMAE = 0.008). Curvas relacionando a taxa evaporativa mensal com temperatura do ar e velocidade do vento foram propostas, apresentando forte coeficientes de correlação ($r^2 = 0.736$ para temperatura do ar e 0.853 para velocidade do vento). A taxa de evaporação média diária modelada pelo Delft3D diferiu em menos de 5% dos resultados obtidos pelo SR. Com relação aos resultados da espacialização, foi observado que o critério de alagamento do modelo impacta a distribuição de calor no reservatório, com a retenção dessa energia na região adjacente à área molhada do lago. Essa condição se mostrou mais relevante para os dias com menor nível d'água. Para o dia com maior volume, a espacialização da evaporação simulada pelo modelo 3D foi semelhante à obtida por SR, dado que não há interferência na transferência de calor do modelo. No que tange à estrutura térmica, a anomalia da energia potencial (PEA) indicou a ocorrência de estratificação no período chuvoso (r^2 calculado para PEA e profundidade igual a 0.33), a qual provavelmente não foi causada pelo aquecimento da superfície, mas sim pelo esfriamento da camada de fundo causado pelas baixas temperaturas da vazão de entrada. Nesse contexto, a evaporação obteve correlação negativa com PEA, apresentando um baixo coeficiente de correlação ($r^2 = 0.24$), o que pode indicar uma alternância de correlação positiva/negativa variando com os períodos seco e chuvoso da região. Por fim, este estudo propõe uma abordagem inovadora que pode ser utilizada para otimizar a localização de técnicas de redução de evaporação, como difusores de ar, estruturas de sombreamento da superfície e painéis solares flutuantes, de forma a ser uma ferramenta no processo de fortalecimento da disponibilidade hídrica para a população.

Palavras-chave: Delft3D; evaporação; hidrodinâmica; sensoriamento remoto.

ABSTRACT

In arid and semiarid environments, the evaporation rates are a main water loss. This condition is specially concerning in the Brazilian Northeast region, as this is one of the most populous semiarid areas in the planet. In a reality of poor water availability, fully understanding the complexities involved in surface water losses along with the vertical process in a reservoir is of great importance. This study aims to calibrate the thermal structure of Pentecoste reservoir, located in the Brazilian semiarid region, and assess the variability of evaporation rates on its surface by using the tridimensional model Delft3D-FLOW. Additionally, the spatial distribution results obtained by the 3D model are compared with those estimated by a remote sensing technique (RS). The calibration results showed an accurate reproduction of the water level variability (r^2 of 0.997), along with a satisfactory calibration of the reservoir's thermal structure for the full water column (MAE of 0.539 °C, RMSE of 0.572 °C, and NMAE of 0.008). Curves relating monthly evaporation rates with air temperature and wind speed showed strong correlation between those variables (r^2 of 0.734 for air temperature and 0.853 for wind speed). Also, the averaged evaporation rates modeled by Delft3D were less than 5% different from those estimated by the RS. Regarding the spatial distribution results, it was found that the drying and flooding criteria of Delft3D impacted the heat distribution in the water body, with the adjacent cells substantially retaining heat. This condition was found more relevant on the days with notably low water level. For the day with higher volume, the spatial distribution of evaporation rates was similar to that of RS, due to the occurrence of heat transfer. Regarding the thermal structure, the potential energy anomaly (PEA) results indicated stratification condition in the wet season (r^2 between PEA and water depth of 0.33), which was probably induced not by the heating of the water surface, but by the cooling of the bottom layer caused by low temperature inflow. In fact, evaporation rates showed negative correlation with PEA with a relatively low coefficient of correlation (r^2 of 0.24), which could indicate alternating negative/positive correlation depending on the season. To conclude, this study brings an innovative approach which may be used to optimize the location for techniques that lower evaporation rates, such as air diffusers, shading structures, and floating solar panels, and therefore be a tool in the process of enhancing water availability for the population.

Keywords: Delft3D; evaporation; hydrodynamics; remote sensing.

LIST OF FIGURES

LIST OF TABLES

CONTENTS

1 INTRODUCTION

Evaporation is a main water loss in arid and semiarid environments (ALI *et al*., 2008, HELFER *et al.,* 2018, MESQUITA *et al*., 2020, SHALABY *et al*., 2021). In the Ceará state, located on the semiarid region of Brazil, this problem is of particular interest, as the human water supply basically comes from reservoirs and this is the most populous semiarid area in the planet (CAMPOS, 2015, SACRAMENTO *et al*., 2015, de ARAÚJO *et al*., 2018, RABELO *et al*., 2021, RAULINO *et al*., 2021). In fact, there are over 48,000 reservoirs in the mentioned region, from which over 26,000 have a surface area of more than 1.0 ha (SIRH/Ce, 2020), and the evaporation losses are as high as 2,000 mm per year (de ARAÚJO; PIEDRA, 2009, MAMEDE *et al*., 2012, CAMPOS *et al*., 2016). Figure 1 illustrates the water bodies of Ceará state.

Figure 1 - Map of water bodies at Ceará state

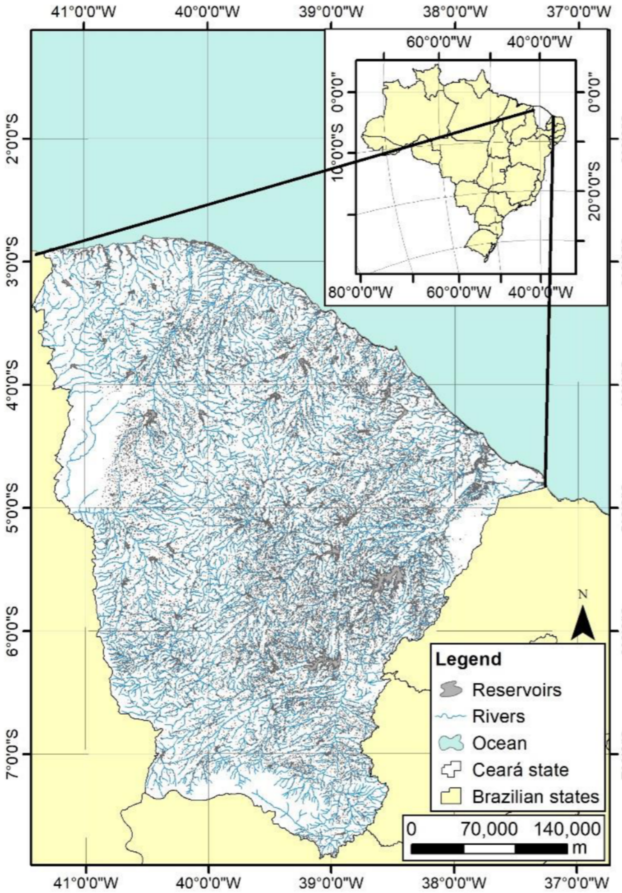

In this context, when looking into future perspectives and considering climate change scenarios, evaporation rates tend to increase as air and water temperatures go higher (DIJK; van VUUREN, 2009, LOWE *et al*., 2009, BIGLARBEIGI *et al*., 2018, LIMA NETO, 2019, AZADI *et al*., 2021). Thus, water availability is expected to decrease especially in the already vulnerable regions (KROL *et al*., 2011, EHSANI *et al*., 2017). Historically, locations that suffer with water scarcity and badly distributed rainfall events tend to store water in reservoirs, which, as lentic environments, are susceptible to high evaporation rates and strong water level oscillations (COSTA *et al*., 2021, WIEGAND *et al*., 2021, LIMA NETO *et al*., 2022). Further understanding of these patterns is necessary in order to strengthen water management and enhance water availability for the population.

Different equipment exist to measure evaporation rates, e.g., class A pans and eddy covariance devices, but they are often expensive to install and maintain and are not common in most of the water systems (MORTON, 1994, ALTHOFF *et al.*, 2019). Additionally, different indirect methods are applied to estimate evaporation, e.g., Penman, Penman-Monteith, Priestley-Taylor, etc., but the estimated values show a high discrepancy and the most accurate ones require detailed meteorological information (WANG *et al*., 2014, TANNY *et al*., 2008, ALAZARD *et al*., 2015). These techniques are not capable of identifying the surface distribution of evaporation rates, and understanding this variability along with averaged evaporation patterns is a key factor in managing water resources (ZHAO; GAO, 2019, RODRIGUES *et al*., 2021b).

On this basis, modeling approaches are a valuable tool to understand the surface water loss distribution. These estimations usually require techniques based on satellite images at low cost (LINACRE, 1977, ZHANG *et al*., 2017, ZHAO; GAO, 2019, RODRIGUES *et al*., 2021a, GHAHREMAN; RAHIMZADEGAN, 2022). Among those techniques, the evaporation model of Linacre (1977) shows advantage as the input data are restricted to air and dew point temperatures, and it registers good accuracy in semiarid regions (BENZAGHTA *et al*., 2012, RODRIGUES *et al*. 2021b). Remote sensing techniques provide information on the spatial distribution of evaporation, but they may not be available for a continuous period due to the interference of cloud cover on radars images, and they capture only the surface layer of water bodies.

Another potential tool for understanding the complexities of the spatial distribution of evaporation rates is tridimensional numerical modeling, although they are not often used for this purpose. Such models are usually applied to lakes and reservoirs successfully reproducing their thermal structure and hydrodynamics (CHANUDET *et al*., 2012, NAKHAEI *et al*., 2019, DISSANAYAKE *et al*., 2019, AMORIM *et al*., 2021, PICCIONI *et al*., 2021, PLEC *et al*., 2021), which influence the evaporation patterns (ELHAKEEM *et al*., 2015, FRIEDRICH *et al*., 2018). To the author's knowledge, 3D hydrodynamic and water quality models have not yet been used to model reservoirs located in the Brazilian semiarid region.

Evaporation losses can also be assessed by two dimensional vertical (2DV) models, but they do not provide information on the reservoir surface variabilities (LEE *et al*., 2018, MESQUITA *et al*., 2020). In this context, 3D models are a tool that allows the study of both spatial distribution of evaporation and how the vertical mixing patterns of the lake influence on it. Additionally, those models can be used to investigate the impacts of different strategies for reducing evaporation rates on the water bodies, such as lake surface coverages (MADY *et al*., 2021, SHALABY *et al*., 2021), artificial aeration/destratification (HELFER *et al*., 2018, LIMA NETO, 2019) and solar panels (PEREZ *et al*., 2018, RODRIGUES *et al*., 2020), as well as to optimize their location.

Additionally, in order to fully understand the complexities of a water impoundment and its patterns, the assessment of the hydrodynamics and thermal structure is central. Actually, the stratification of the water column in a reservoir is a determinant factor for the dynamics of water quality (CHUNG *et al*., 2014; YANG *et al*., 2018; SOARES *et al*., 2019; ZIAIE *et al*., 2019; SHILEI *et al*., 2020; BARBOSA *et al*., 2021). It is caused by a temperature gradient resulting in density differences between the surface and bottom layers.

With the aim to study and further understand the stratification process, there are several numbers that estimate the stability of the water column based on its physical parameters and the local meteorological characteristics, namely the Richardson's number, Lake Number, Wedderburn number, Schmidt Stability number, and also the Potential Energy Anomaly (PEA) (SIMPSON *et al*., 1977; IMBERGER and HAMBLIN, 1982; KIRILIN and SHATWELL, 2016; ZHAO *et al*., 2018; ISHIKAWA *et al*., 2021). Among those, PEA is a very useful index, as it measures the required energy for the complete mixing of the water column (HOFMEISTER *et al*., 2009). PEA is measured in unit of energy per unit of volume, and it gets higher with higher density gradients. Thus, high PEA indicates a stable thermal stratification.

2 OBJECTIVES

2.1 Main objective

This study aims to assess the spatial distribution of evaporation rates in a semiarid reservoir by using both 3D modeling and remote sensing techniques along with its thermo and hydrodynamic behavior.

2.2 Specific objectives

- Calibrate the hydrodynamic module of Delft3D for Pentecoste reservoir, in the State of Ceará, Brazil, in order to reproduce its thermal structure;
- Evaluate the mixing patterns of the reservoir;
- Compare the average evaporation results from Delft3D and remote sensing;
- Analyze the spatial distribution of the evaporation rates in the reservoir.

3 THEORETICAL BACKGROUNDS

In fluid mechanics, reproducing the underlying processes of water impoundments is very important on the context of understanding the environmental complexities. Figure 2 brings an overview of a reservoir's simulation domain from the General Lake Model (Hipsey *et al*., 2019).

Figure 2 - The General Lake Model representation of a reservoir's simulation domain

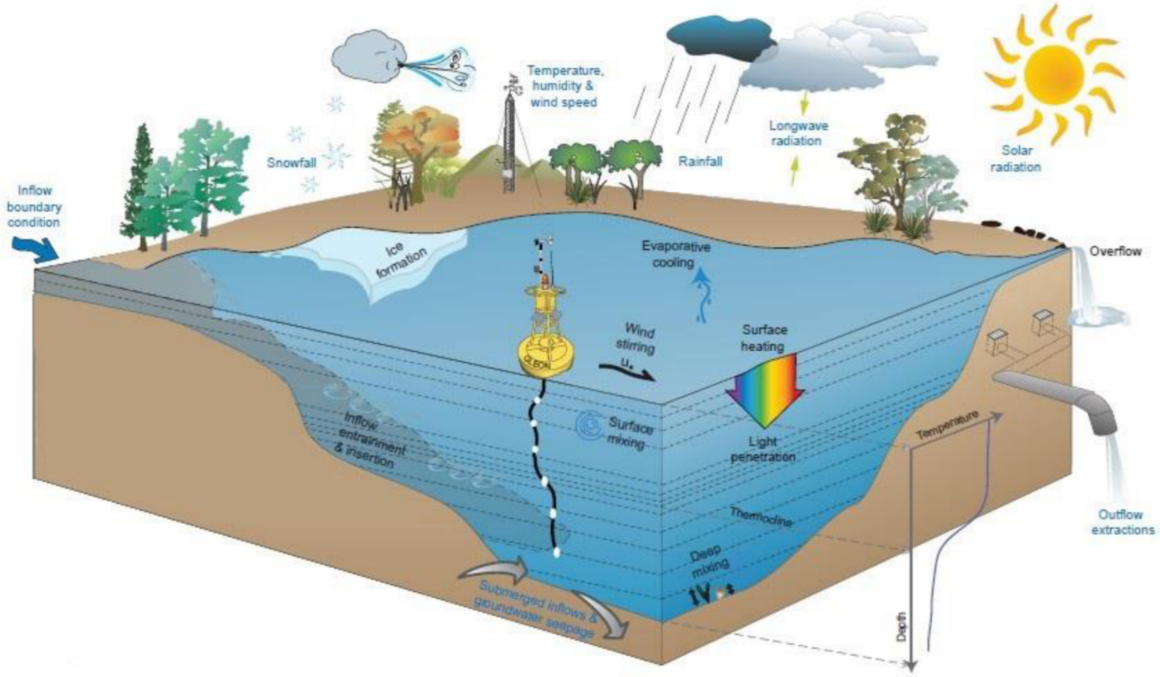

Source: adapted from Hipsey *et al*. (2019)

3.1 Conservation laws

With the increasing of water availability problems, the interest in understanding and reproducing the environmental processes by researchers has grown. As a consequence, equations were developed to reproduce the governing principles in fluid mechanics, including the conservation laws for mass, momentum, and energy (KUNDU, 2016). The equations for each of those principles are presented as follows, both in their integral and differential forms.

As described by Kundu (2016), Equation 1 shows the statement of conservation of mass for an arbitrary moving control volume (see Figure 3).

Figure 3 - Geometry depiction of an arbitrary moving control volume

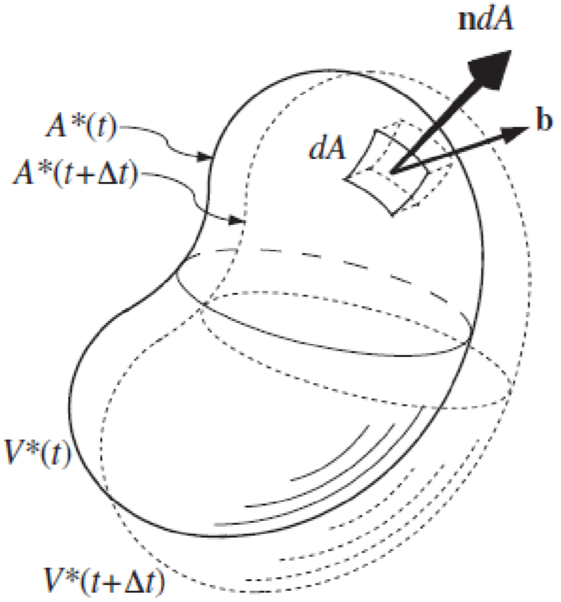

Source: Kundu (2016)

$$\frac{d}{dt}\int_{V^*(t)} \rho(x,t)dV + \int_{A^*(t)} \rho(x,t)(\boldsymbol{u}(x,t) - \boldsymbol{b}) \cdot \boldsymbol{n} dA = 0 \quad (1)$$

Where $V^*(t)$ is the control volume, $A^*(t)$ is the surface of the control volume, ρ is the water density, t is time, **u** is the local fluid velocity, **b** is the control surface velocity, and **n** is the outward normal on $A^*(t)$.

Equation 2 is the differential form of Equation 1, and this relationship is known as the *continuity equation.*

$$\frac{\partial \rho}{\partial t} + \frac{\partial}{\partial x_i}(\rho u_i) = 0 \quad (2)$$

The second term in Equation 2 is the divergence of the mass-density flux and can be interpreted as the net loss at a point due to divergence of a flux, and it is also called transport term (KUNDU, 2016).

In the same direction, Equation 3 presents the general integral statement of momentum conservation for an arbitrarily moving control volume (KUNDU, 2016).

$$\frac{d}{dt}\int_{V^*(t)} \rho(x,t)\boldsymbol{u}(x,t)dV + \int_{A^*(t)} \rho(x,t)(\boldsymbol{u}(x,t) - \boldsymbol{b}) \cdot \boldsymbol{n} dA = \int_{V^*(t)} \rho(x,t)\boldsymbol{g} dV + \int_{A^*(t)} \boldsymbol{f}(\boldsymbol{n},x,t)dA \quad (3)$$

Where $\rho\boldsymbol{u}$ is the momentum per unit volume of the flowing fluid, **g** is the body force per unit mass acting on the fluid within V(t), **f** is the surface force per unit area acting on A(t), and **n** is the outward normal on A(t).

The momentum conservation equation for Newtonian fluids, that are fluids that follow the simplest possible linear constitutive equation, is described by Equation 4. This is the Navier-Stokes momentum equation (KUNDU, 2016).

$$\rho\left(\frac{\partial u_j}{\partial t} + u_i \frac{\partial u_j}{\partial x_i}\right) = -\frac{\partial p}{\partial x_j} + \rho g_j + \frac{\partial}{\partial x_i}\left[\mu\left(\frac{\partial u_j}{\partial x_i} + \frac{\partial u_i}{\partial x_j}\right) + \left(\mu_v - \frac{2}{3}\mu\right)\frac{\partial u_m}{\partial x_m}\delta_{ij}\right] \quad (4)$$

Where p is the thermodynamic pressure, μ_v is the coefficient of bulk viscosity, μ is the viscosity, and δ_{ij} is the second-order isotropic sensor *Kronecker delta* $\delta_{ij} = \begin{Bmatrix} 1 \; if \; i = j \\ 0 \; if \; i \neq j \end{Bmatrix}$.

The viscosities μ and μ_v for Equation 4 depend on the thermodynamic state, and the viscosity μ displays a strong dependence on temperature. For liquids, μ decreases with an increase in temperature (KUNDU, 2016).

Consequently, by analyzing both the equations of conservation of mass and momentum, there are five dependent variables that, combined with adequate boundary conditions, issue a complete description of fluid dynamics when ρ is a known constant or is a known relationship with p. When the latter relationship also includes the temperature, the thermal energy of the fluid has to be considered and then a third equation representing conservation of energy is needed (KUNDU, 2016). Equation 5 shows the integral form of the conservation of energy for an arbitrarily moving control volume.

$$\frac{d}{dt}\int_{V^*(t)} \rho \left(e + \frac{1}{2}|\boldsymbol{u}|^2\right) dV + \int_{A^*(t)} \left(\rho e + \frac{\rho}{2}|\boldsymbol{u}|^2\right)(\boldsymbol{u} - \boldsymbol{b}) \cdot \boldsymbol{n} dA = \int_{V^*(t)} \rho \boldsymbol{g} \cdot \boldsymbol{u} dV + \int_{A^*(t)} \boldsymbol{f} \cdot \boldsymbol{u} dA - \int_{A^*(t)} \boldsymbol{q} \cdot \boldsymbol{n} dA \tag{5}$$

Where e is the thermal energy of the fluid, and $\boldsymbol{q}$ is the heat flux vector.

The differential form of Equation 5 is obtained by collecting all terms under the same volume integration, and the result is expressed as Equation 6.

$$\frac{De}{Dt} = -p\frac{Dv}{Dt} + \frac{1}{p}\tau_{ij}S_{ij} - \frac{1}{\rho}\frac{\partial q_i}{\partial x_i} \tag{6}$$

Where τ_{ij} is the fluid-dynamic stress, and S_{ij} is the strain rate tensor $S_{ij} = \frac{1}{2}\left(\frac{\partial u_i}{\partial x_j} + \frac{\partial u_j}{\partial x_i}\right)$.

In Equation 6, the first two terms on the right are the pressure and viscous work while the final term represents heat transfer from the fluid particle. As stated in Kundu (2016), the viscous term is the kinetic energy dissipation rate per unit mass ε, and it represents the irreversible conversion of mechanical energy to thermal energy through the action of viscosity. Additionally, ε is essential for the physics of turbulent flow and its description.

3.2 Heat balance and water balance

When analyzing reservoirs, there are three main disturbing influences that impact lake’s thermodynamic and, as a consequence, water balance. The first influence is the meteorological forcing that will determine the energy transfers in the air-water interface, and they may consist of thermal exchanges due to radiation, sensible heat transfer and evaporation, or mechanical energy transfer due to wind. Second, the inflows may transmit kinetic and potential energy to the water column. Finally, the third is the outflow, which may alter the kinetic energy of the lake (FISCHER, 1979). Figure 4 shows a schematic representation of possible mixing mechanisms acting in lakes or reservoirs.

Figure 4 - Heat exchange in lakes and reservoirs

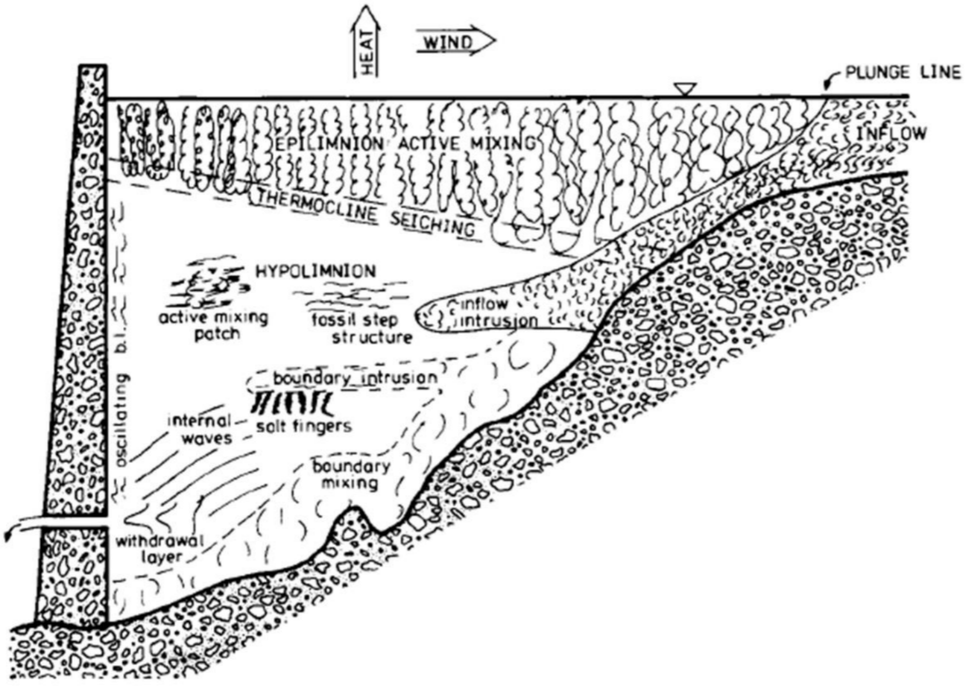

Source: Fischer (1979).

The high variability and usually low quality of meteorological data complicate the estimation of thermal transfer of heat by evaporation, radiation, and conduction (FISCHER, 1979). The sensible heat transfer H_s (heat flux due to conduction) and the loss of heat due to evaporation H_L may be written as given by Equations 7 and 8 (FISCHER, 1979).

$$H_S = C_S \rho_A C_P U (T_0 - T) \tag{7}$$

$$H_L = C_L \rho_A L_W U (Q_0 - Q) \tag{8}$$

Where C_S and C_L are the coefficients incorporating all the variability induced by other influences, C_P is the specific heat of air, T_0 the water surface temperature, T the temperature at 10 m, L_W the latent heat of evaporation, Q_0 the saturation specific humidity at T_0, and Q the specific humidity at 10 m.

Thus, the heat exchange between the atmosphere and the water column is given in Equation 9 (NIÑO; TAMBURRINO, 2004).

$$H_n = H_{sw} + H_H - H_B - H_L - H_s \tag{9}$$

Where H_n is the heat flux from the atmosphere to the water body per unit area, H_{sw} is the heat flux due to short wave radiation from the sun, H_H is the heat flux from clouds and atmosphere in general, and H_B is the heat flux due to black-body radiation from the free surface.

Figure 5 illustrates the heat exchanges on the water surface of a reservoir.

Figure 5 - Components of the surface heat exchange

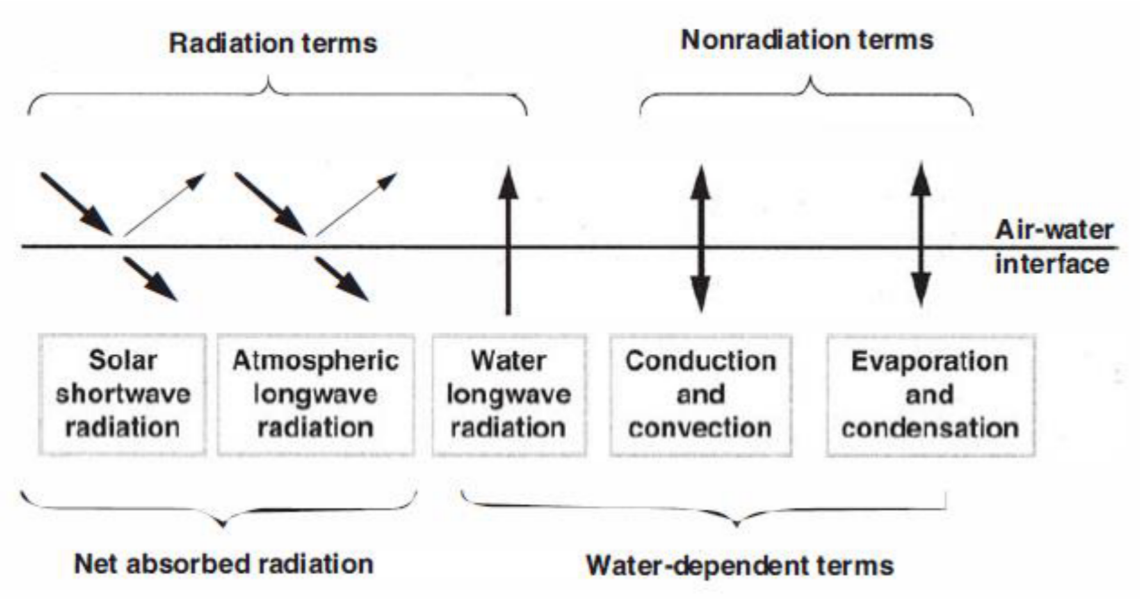

Source: Chapra (1997).

Hence, by following the idea of the conservation laws, the variability of a lake's volume with time may be estimated by a water balance of the reservoir given the known processes of water intakes and losses. The water balance of a reservoir can be written as Equation 10 (CHAPRA, 1997), which is an extension of Equation 2.

$$S = \frac{dV}{dt} = Q_{in} - Q_{out} + G + PA_S - EA_S \tag{10}$$

Where S is the storage [m³ d^{-1}], V is the volume [m³], t is time [d], Q_{in} is the inflow [m³ d^{-1}], Q_{out} is the outflow [m³ d^{-1}], G is the groundwater flow [m³ d^{-1}], P is precipitation [m d^{-1}], E is evaporation [m d^{-1}], and A_S is the surface area [m²].

In addition, in order to represent the thermal stratification of the water column, the heat transfer through advection and diffusion in a turbulent flow needs to be represented. The governing equation for this process is given after the description of turbulent flows, as those principles are used in the general form of the advection-diffusion transport equation.

3.3 Mechanical energy transfer due to wind

Wind forcing directly influences the mixing patterns of a water body, as it exerts a drag force on the lake surface. The stress in the water surface is dependent on the wind strength, the stability of the meteorological boundary layer over the surface, the variability of the wind speed, and the length of fetch, as well as the degree of wave development and the amount of wave energy dissipation at the shores of the lake (FISCHER, 1979). The formula of the stress exerted by the wind on the water surface is given by Equation 11 following Fischer (1979).

$$\tau = C_D \rho_A U^2 \tag{11}$$

Where C_D is the drag coefficient, ρ_A is the air density, and U is the wind speed at 10 meters above the water surface. The drag coefficient ranges from 1.0 x 10^{-3} to 1.5 x 10^{-3} (FISCHER, 1979).

3.4 Computational fluid dynamics (CFD)

Together, conservation principles, constitutive assumptions for viscous forces and heat conduction should make it possible to reproduce fluid motions in all circumstances. Even though theoretically true, analytical solutions exist only for very simple cases (KUNDU, 2016). In this sense, computational fluid dynamics (CFD) are defined by Kundu as the search of numerical solutions for the Navier-Stokes equations in two or three dimensions. Figure 6 brings the approximation of a flow field on a discrete grid, which is the base mesh of computational models as they solve the conservation equations for each control volume.

Figure 6 - Approximation of a flow field on a discrete grid

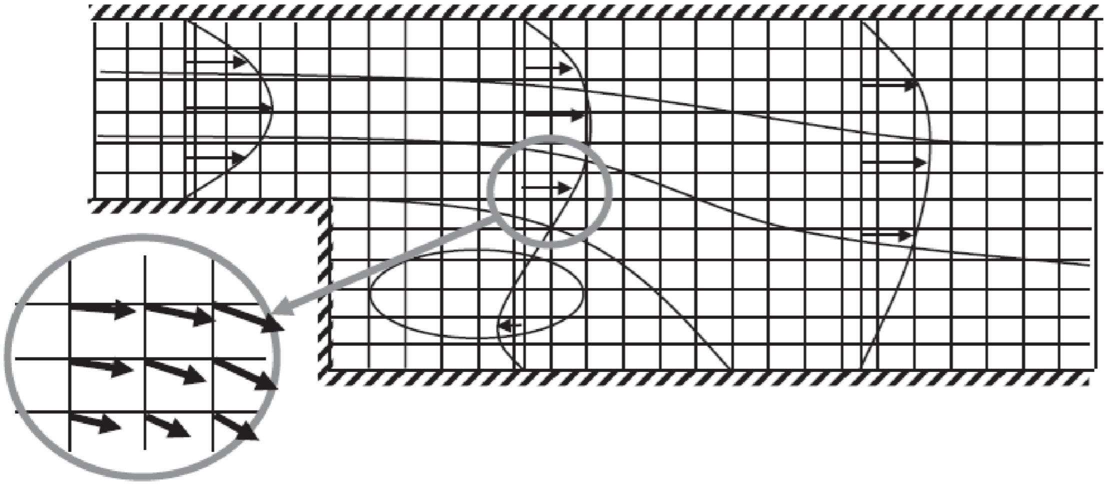

Source: Kundu (2016).

There are different methods for approximating flow fields. Kundu (2016) brings two approaches of finite volume and finite difference as the main ones. In the finite difference method, the equations are calculated for each grid point, while for the finite volume approach the principles of conservation are applied in each control volume, that would be the center of the cells in Figure 6 (KUNDU, 2016).

3.4.1 Turbulent flow

In practice, nearly all flows in the natural world and in engineering practice are turbulent. A turbulent fluid velocity field conserves mass, momentum, and energy, which is why it is not the same as randomness (KUNDU, 2016). Turbulence involves fluctuations that are unpredictable in detail, and it has a few generic characteristics, named fluctuations, nonlinearity, vorticity, dissipation, and diffusivity. Kundu (2016, p. 605) gives a simple definition of turbulence as “a dissipative flow state characterized by nonlinear fluctuating three-dimensional vorticity”.

Moreover, an important definition regarding turbulence are the eddies, which are identifiable structures in a turbulent flow, as they always have a range of eddy sizes. Figure 7 brings a typical large eddy of size l, while δ is the average layer thickness. In most turbulent flows the size of the largest eddies is comparable to the overall layer thickness (KUNDU, 2016).

Figure 7 - Turbulent flow scheme illustrating large eddy

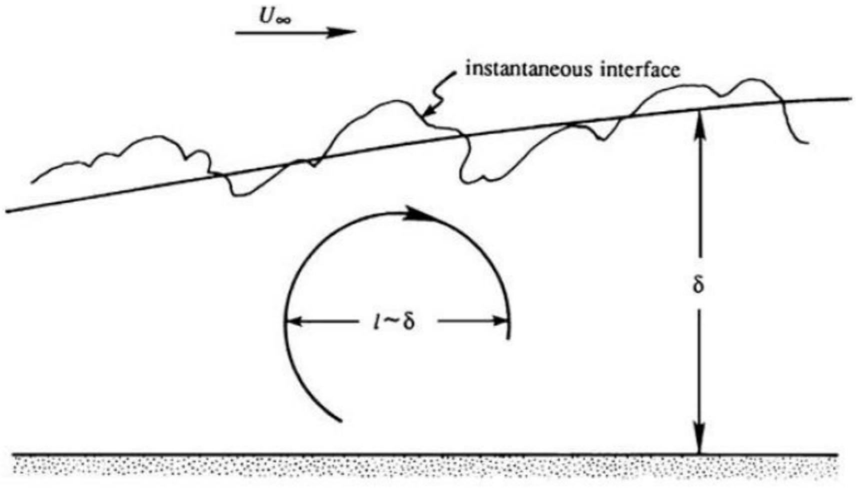

Source: Kundu (2016).

In a turbulent flow, there is always a spectrum of eddy sizes as the large ones continuously break down onto smaller ones. Eventually, the viscosity of the flow takes over as the eddies become small enough, so the energy is converted into heat and called dissipation. The length scale of the eddies in which turbulent energy is converted to heat is called the Kolmogorov scale L_K, that depends on the rate of dissipation and on the viscosity (CHAPRA, 1997).

In the following, Osborne Reynolds developed a dimensionless number to describe whether a flow is turbulent or not, lately named the Reynolds number. In fact, one of the main contributions of Reynolds to describing turbulent flows was when he separated turbulent flow-dependent variables into mean and fluctuating components, bringing the concept of turbulent stress, which is known as the *Reynolds decomposition* (KUNDU, 2016). By doing that, a closure problem arises, as it doubles the number of dependent variables and no analytical solution for the equations exist. When applying the Reynolds averaging into the Navier-Stokes equations, they become the commonly known *RANS equations*, that have, as a primarily problem, more unknowns than equations.

Furthermore, for assessing the closure problem there many approaches, among which Kundu (2016) brings the most popular RANS closure modeling, direct numerical simulations (DNS), and large-eddy simulation (LES). Thus, the more widely applied method is the RANS closure model k-ε, which is briefly described in the following section.

3.4.2 Closure model k-ε

As stated by Kundu (2016), the main purpose of a turbulent-mean-flow closure model is to relate the Reynolds stress correlations ($\overline{u_i u_j}$) to the mean-velocity field (U_i). The closure model k-ε has turbulence kinetics energy and diffusivity variables in order to provide the vertical turbulent diffusion coefficients necessary to represent vertical diffusive mass transport (JI, 2008).

The relationship between the Reynolds stress correlations to the mean-velocity field are described by semi-empirical theories, which are based on developing an analogy between molecular-motion-based laminar momentum and scalar transport, and eddy-motion-based momentum and scalar transport. Those models typically have an eddy viscosity ν_T and eddy diffusivities κ_T and κ_{mT} for the equations. In fact, ν_T, κ_T, and κ_{mT} are properties of the flow, not the fluid, and this transport-flow relationship must be modeled (KUNDU, 2016).

3.4.3 The turbulent advective diffusion equation

The Fick's law gives an expression for the flux of mass due to the process of diffusion, but there is still the need for an equation that predicts the change in concentration of the diffusing heat over time (CHAPRA, 1997). Then, in order to develop this equation for turbulent flows, the Reynolds decomposition is used for the advective and diffusion terms. The final form of the turbulent advective diffusion equation of heat is expressed as Equation 12.

$$\frac{\partial T}{\partial t} + u\frac{\partial T}{\partial x} + v\frac{\partial T}{\partial y} + w\frac{\partial T}{\partial z} = \frac{\partial}{\partial x}\left(D_{t_x}\frac{\partial T}{\partial x}\right) + \frac{\partial}{\partial y}\left(D_{t_y}\frac{\partial T}{\partial y}\right) + \frac{\partial}{\partial z}\left(D_{t_z}\frac{\partial T}{\partial z}\right) \qquad (12)$$

Where T is temperature, u, v, w are the velocities in the x, y, z directions, respectively, and D_{t_x}, D_{t_y}, D_{t_z} are the turbulent diffusion coefficients in the x, y, z directions, respectively. The turbulent diffusion coefficient is usually much greater than its molecular component, therefore the latter is neglected.

3.5 Hydrodynamic modeling

In order to study the hydrodynamics of a reservoir, different numerical and multidimensional models are available (SOARES; CALIJURI, 2021; MAN *et al*., 2021; POLLI;

BLENINGER, 2019; VINÇON-LEITE; CASENAVE, 2019). These models can be unidimensional, bidimensional, and tridimensional.

With 1-D models, it is possible to analyze the vertical processes of a point in the reservoir, and they are usually applied for larger-scale studies, i.e. long periods or many reservoirs (BRUCE *et al.*, 2018; SOARES *et al.*, 2020). Despite its simplicity, they are often applied to model water quality. Wang et al. (2009) assessed the impact of hydrodynamics processes in the algal proliferation by applying the 1-D simplification and obtained satisfactory validation. Also, other studies coupled 1-D configurations with models of phosphorus and sediment transport (HUANG *et al.*, 2015a, b). Moreover, some examples of the mentioned approach are the General Lake Model (GLM) and the Dynamics Reservoir Simulation Model (DYRESM). Figure 8 gives the schematic of mixing processes using GLM (HIPSEY *et al.*, 2019).

Figure 8 - Schematic of mixing processes using GLM

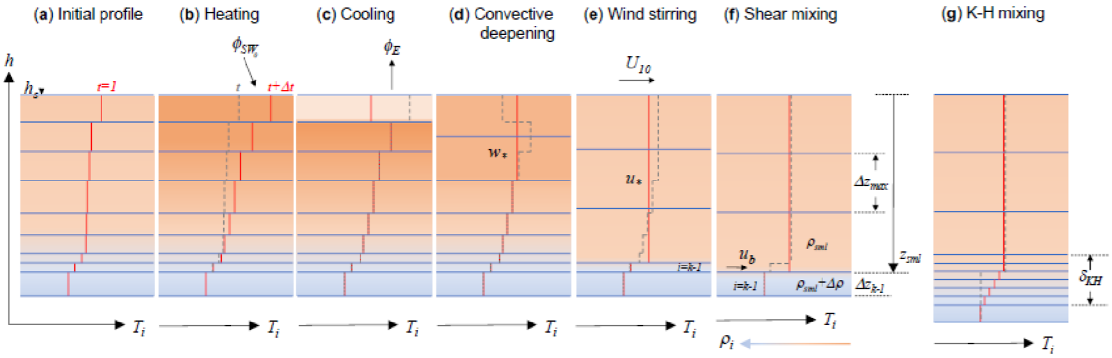

Source: Hipsey *et al.*, (2019)

On the other hand, 2-D models allow the simulation of a plane in the reservoir, making it possible to simulate horizontal and vertical transport processes, although needing more computational effort than the first one (ISHIKAWA *et al.*, 2021). Among those, the hydrodynamic and water quality model CE-QUAL-W2 is an example of a vertical 2-D approach (ROCHA *et al.*, 2020, MESQUITA *et al.*, 2020), while the Basic Environmental Hydrodynamic System (SisBaHiA, in portuguese Sistema Base de Hidrodinâmica Ambiental) represents horizontal 2-D model (DE FRANÇA *et al.*, 2021, PALMAN *et al.*, 2021). Figure 9 gives an example of a bidimensional grid representation (ROCHA, 2019).

Figure 9 - Example of a bidimensional grid representation using CE-QUAL-W2

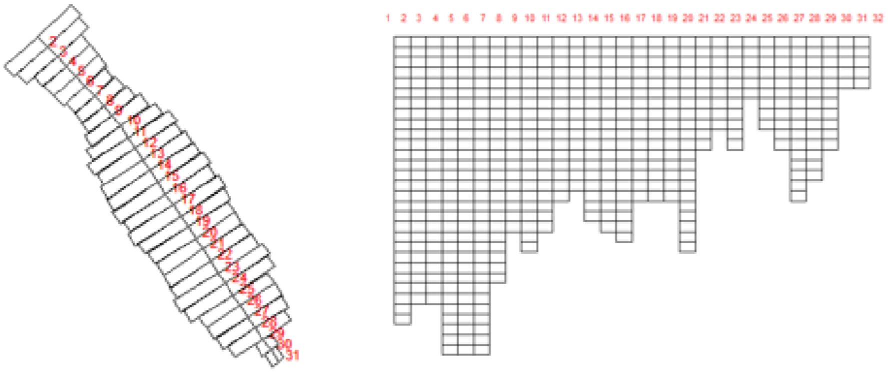

Source: ROCHA (2019)

Finally, 3-D models represent all three dimensions of a water body, but the computational effort is high, with simulations usually taking days to finish (GOLYJESWSKI, 2020; POLLI; BLENINGER, 2019). Examples of 3-D models are Delft3D, Estuary, Lake and Coastal Ocean Model (ELCOM) and Environmental Fluid Dynamics Code (EFDC), the latter can be applied in the preferred dimensionality. Among the available 3D models, Delft3D is a free source software widely applied in multiple water systems, e.g. estuaries, ponds, reservoirs, and rivers (MOLINAS *et al*., 2020, POLLI; BLENINGER 2019, OUNI *et al*., 2020, REY *et al*., 2021, SHARAF *et al*., 2021, XU *et al*. 2021). Figure 10 gives an example of outputs from tridimensional models (REY *et al*., 2021). Thus, Delft3D was chosen for this research knowing it allows the analysis of the spatial distributions of modeled variables, such as water temperature, evaporation rates, velocity, and others, and it will be further descripted in the following section.

Figure 10 - Example of a 3-D model output, here different scenarios of modeled velocities at the surface are given

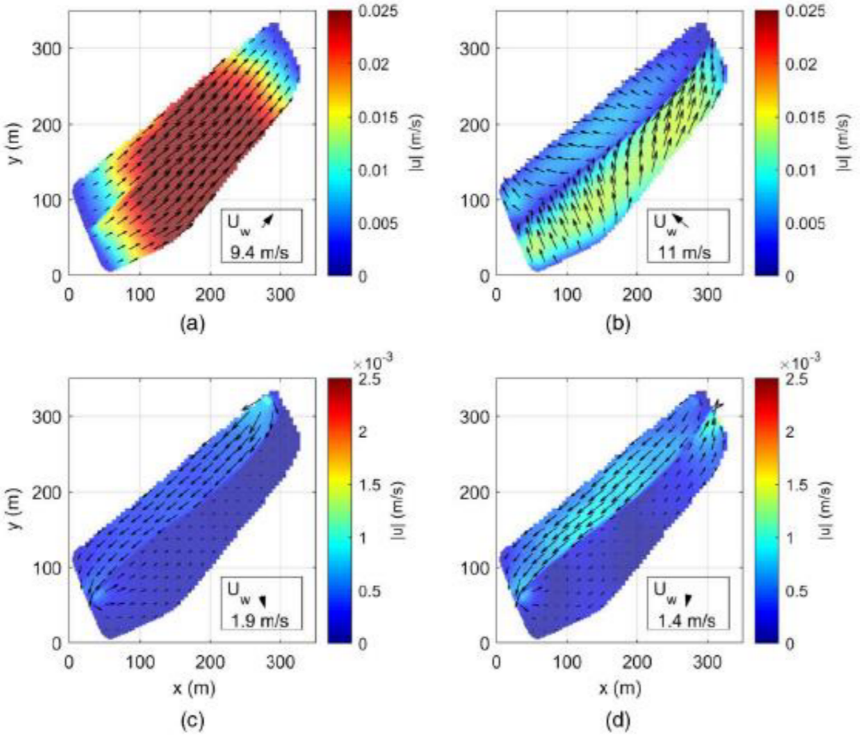

Source: REY *et al.*, (2021)

3.5.1 Delft3D hydrodynamic model

Delft3D is suitable for reproducing environmental processes of surface waters, and it is based on the Reynolds Averaged Navier-Stokes equations (DELTARES, 2020).

3.5.1.1 Governing equations

The system of equations in Delft3D consists of the continuity equation (mass balance), momentum equation, and transport equation (DELTARES, 2020). Equation 13 describes the continuity equation and Equation 14 gives the contribution per area due to discharge or withdrawal.

$$\frac{\partial \zeta}{\partial t} + \frac{\partial}{\partial x}\int_{-d}^{\zeta} u dz + \frac{\partial}{\partial y}\int_{-d}^{\zeta} v dz = 0 \tag{13}$$

Where ζ is the difference from the water level to the reference, and d is the depth.

$$Q = H \int_{-1}^{0} (q_{in} - q_{out}) d\sigma + P - E \tag{14}$$

Where q_{in} and q_{out} are local sinks and sources of water per unit of volume, P is precipitation and E is evaporation.

When applying the z-model in order to capture non-hydrostatic flow, the set of equations presented below is used. For small density differences, the RANS equation may be written as (Deltares, 2020):

$$\frac{\partial u_i}{\partial t} + u_i \frac{\partial u_j}{\partial x_i} + \frac{1}{\rho_0} \frac{\partial P}{\partial X_i} - \frac{1}{\rho_0} \frac{\partial \tau_{ij}}{\partial X_j} + \varepsilon_{ijk} 2\Omega_j u_k = \frac{\rho}{\rho_0} g \delta_{i3} \tag{15}$$

Where δ_{ij} is the Kronecker delta, ε_{ijk} is the permutation symbol, Ω_j is the planetary vorticity and τ_{ij} are the turbulent stresses. The pressure p can be split into a hydrostatic ($\rho g z$) and hydrodynamic (q) part:

$$p = p_{atm} + g \int_{z}^{\zeta} \rho dz' + q \tag{16}$$

Using Equation 16 the momentum equations in the x, y, and z-direction are given by Equations 17, 18, and 19, respectively:

$$\frac{\partial u}{\partial t} + \frac{1}{\rho_0} \frac{\partial}{\partial x} \int_{z}^{\zeta} \rho g dz' + \frac{1}{\rho_0} \frac{\partial q}{\partial x} = RHS_x \tag{17}$$

$$\frac{\partial v}{\partial t} + \frac{1}{\rho_0} \frac{\partial}{\partial y} \int_{z}^{\zeta} \rho g dz' + \frac{1}{\rho_0} \frac{\partial q}{\partial y} = RHS_y \tag{18}$$

$$\frac{\partial w}{\partial t} + \frac{1}{\rho_0} \frac{\partial q}{\partial z} = RHS_z \tag{19}$$

Where the term RHS_i contains the acceleration due to advection, turbulent stresses and Coriolis effect.

Regarding the turbulence closure model, Delft3D allows the user to choose among a constant one, an algebraic one, k-ε or k-L. For the k-ε, transport equations must be solved for both the turbulent kinetic energy k and for the energy dissipation ε. The mixing length L is determined from k and ε according to Equation 20 (DELTARES, 2020).

$$L = c_D \frac{k\sqrt{k}}{\varepsilon} \tag{20}$$

Where c_D is a constant.

Two assumptions are made in the transport equations: the production, buoyancy, and dissipation terms are the dominating terms, as stated by Deltares (2020). The transport equations for k and ε are given by Equations 21 and 22, respectively.

$$\frac{\partial k}{\partial t} + \frac{u}{\sqrt{G_{\xi\xi}}}\frac{\partial k}{\partial \xi} + \frac{v}{\sqrt{G_{\eta\eta}}}\frac{\partial k}{\partial \eta} + \frac{\omega}{d+\zeta}\frac{\partial k}{\partial \sigma} = \frac{1}{(d+\zeta)^2}\frac{\partial}{\partial \sigma}\left(D_k \frac{\partial k}{\partial \sigma}\right) + P_k + P_{kw} + B_k - \varepsilon \tag{21}$$

$$\frac{\partial \varepsilon}{\partial t} + \frac{u}{\sqrt{G_{\xi\xi}}}\frac{\partial \varepsilon}{\partial \xi} + \frac{v}{\sqrt{G_{\eta\eta}}}\frac{\partial \varepsilon}{\partial \eta} + \frac{\omega}{d+\zeta}\frac{\partial \varepsilon}{\partial \sigma} = \frac{1}{(d+\zeta)^2}\frac{\partial}{\partial \sigma}\left(D_\varepsilon \frac{\partial \varepsilon}{\partial \sigma}\right) + P_\varepsilon + P_{\varepsilon w} + B_\varepsilon - c_{2\varepsilon}\frac{\varepsilon^2}{k} \tag{22}$$

With $D_k = \frac{v_{mol}}{\sigma_{mol}} + \frac{v_{3D}}{\sigma_k}$ and $D_\varepsilon = \frac{v_{3D}}{\sigma_\varepsilon}$.

Where v_{3D} is the vertical eddy viscosity, P_k and P_ε are production terms, P_{kw} is the turbulent energy production due to wave action, $P_{\varepsilon w}$ is the energy dissipation due to waves, B_k is the buoyancy term, B_ε is the buoyancy flux, and $c_{2\varepsilon}$ is a calibration constant of the model equal to 1.92.

3.5.1.2 Heat balance

The heat exchange module of Delf3D at the free surface is estimated by taking into account separate effects of solar (short wave) and atmospheric (long wave) radiation, and the heat loss due to back radiation, evaporation and convection (DELTARES, 2020). The governing formulation is presented below. Equation 23 shows the total heat flux through the free surface.

$$Q_{tot} = Q_{sn} + Q_{an} - Q_{br} - Q_{ev} - Q_{co} \tag{23}$$

Where Q_{sn} is the net incident solar radiation (short wave), Q_{an} is the net incident atmospheric radiation (long wave), Q_{br} is the back radiation (long wave), Q_{ev} is the evaporative heat flux (latent heat), and Q_{co} is the convective heat flux (sensible heat).

Equation 24 shows the change in temperature in the top layer T_s [°C].

$$\frac{\partial T_s}{\partial t} = \frac{Q_{tot}}{\rho_w c_p \Delta z_s} \tag{24}$$

Where Q_{tot} is the total heat flux through the air-water surface [J m^{-2}s], ρ_w is the specific density of water [kg m^{-3}], c_p is the specific heat capacity of sea water [= 3,930 J kg^{-1}K], and Δz_s is the thickness of the top layer [m].

In Figure 11 the heat exchange mechanisms at the surface of the reservoir can be seen.

Figure 11 - Scheme of the heat exchange mechanism at the surface

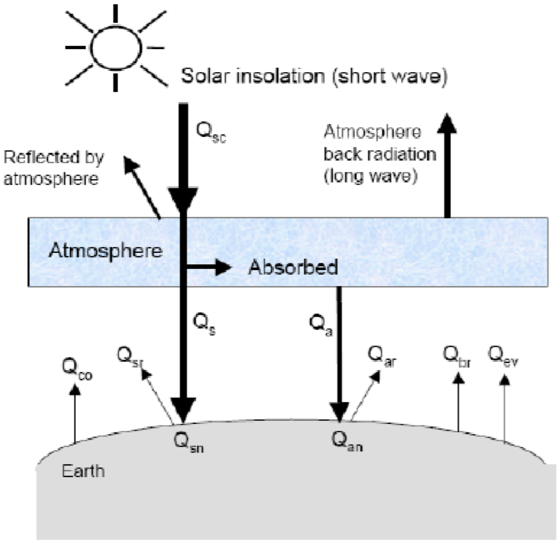

Source: Deltares (2020).

3.5.1.3 Heat flux model

When including temperature process, the user can specify how the heat exchange through the free surface is modelled. There are six different options available: no flux, absolute flux (total solar radiation), absolute flux (net solar radiation), excess temperature, Murakami, and Ocean. Detailed information on each model can be found in the Delft3D-FLOW User Manual (DELTARES, 2020). The Ocean heat flux model will be further described, as it is the most complete heat flux model offered by Delft3D-FLOW, and it is used in reservoir studies (ELHAKEEM *et al.*, 2015, PLEC *et al.*, 2021, SHARAF *et al.*, 2021).

For the Ocean heat flux model not all the radiation is absorbed at the water surface, some of it is transmitted to the deeper water. Thus, the incoming solar radiation is separated into the longer wave portion, which is absorbed at the surface, and the reminder part that goes to the deeper water. Equation 25 shows the absorption of heat in the water.

$$Q_{sn}(h) = \frac{\gamma e^{-\gamma h}}{1-e^{-\gamma H}}(1-\beta)Q_{sn} \tag{25}$$

Where β is part of Q_{sn} absorbed at the water surface which is a function of the wavelength, γ is the extinction coefficient in m^{-1}related to the Secchi-depth $\gamma = \frac{1.7}{H_{Secchi}}$, h is the distance to the water surface [m], and H is the total water depth.

In the Ocean heat flux model, the solar radiation flux is computed dependent on the geographical position and the local time. The incoming energy flux at the water surface depends on the angle between the incoming radiation and the Earth's surface (DELTARES, 2020). Furthermore, a part of the radiation that reaches the water surface is reflected, and the fraction reflected (surface albedo) is dependent on latitude and season. The surface albedo is considered constant and equal to 0.06.

3.5.1.4 Evaporative heat flux for the Ocean model

The evaporation depends on the conditions both in the water near the surface and the air above it. This type of water loss is strongly related to meteorological factors, especially wind-driven convection, and vapor pressures (DELTARES, 2020). The equations regarding the description of this process are presented below:

The evaporative heat flux Q_{ev} is defined in Equation 26.

$$Q_{ev} = L_v E \tag{26}$$

Where L_v is the latent heat of vaporization in J/kg water $L_v = 2.5 \cdot 10^6 - 2.3 \cdot 10^3 T_s$, T_s is the water surface temperature, and E is defined as the mass of water evaporated per unit area per unit time.

Equation 27 shows some form of the Dalton's law of mass transfer used to estimate E.

$$E = f(U_{10})(e_s - e_a) \tag{27}$$

Where U_{10} is the wind velocity measured at 10 m from the water surface, e_s is the saturated vapor pressure, and $e_a$is the actual vapor pressure.

For the Ocean heat flux method, the vapor pressures are computed as described by Equations 28 and 29.

$$e_s = 10^{\frac{0.7859+0.03477T_s}{1.0+0.00412T_s}} \tag{28}$$

$$e_a = r_{hum} 10^{\frac{0.7859+0.03477T_a}{1.0+0.00412T_a}} \tag{29}$$

Where r_{hum} is the relative humidity [-], and T_a is the air temperature.

In the Ocean heat flux model, the evaporation rate is computed from the difference in relative humidity, rather than from the difference in vapor pressure. The contribution to the evaporative heat flux (Q_{ev}) is split in a contribution by forced convection ($Q_{ev,forced}$) and a contribution by free convection ($Q_{ev,free}$), as given by Equation 30. The first is driven by the wind, while the second is driven by buoyant forces due to density differences creating unstable conditions in the atmospheric boundary layer. The effective back radiation and the heat losses due to evaporation and convection are computed by the model (DELTARES, 2020).

$$Q_{ev} = Q_{ev,forced} + Q_{ev,free} \tag{30}$$

Therefore, the latent heat flux due to forced convection is expressed as Equation 31.

$$Q_{ev,forced} = L_V \rho_a f(U_{10})\{q_s(T_s) - q_a(T_a)\} \tag{31}$$

With q_s and q_a the specific humidity of respectively saturated air and remote air (10 meters above water level), as described in Equations 32 and 33.

$$q_s(T_s) = \frac{0.62 e_s}{P_{atm} - 0.38 e_s} \tag{32}$$

$$q_a(T_a) = \frac{0.62 e_a}{P_{atm} - 0.38 e_a} \tag{33}$$

The wind function from Equation 27 is given by Equation 34.

$$f(U_{10}) = c_e U_{10} \tag{34}$$

Where c_e is the Dalton number, a calibration parameter.

In the following, loss of heat due to evaporation also occurs by free convection, which is important in circumstances where inverse temperature/density gradients are present and wind speeds are almost negligible so that the amount of force convection is small (Deltares, 2020). The latent heat flux due to free convection is expressed as Equation 35.

$$Q_{ev,free} = k_s L_V \overline{\rho_a}(q_s - q_a) \tag{35}$$

With the average air density $\overline{\rho_a} = \frac{\rho_{a0} + \rho_{a10}}{2}$.

The heat transfer coefficient is defined as Equation 36.

$$k_s = \begin{cases} 0 & if\ \rho_{a10} - \rho_{a0} \leq 0 \\ c_{fr.conv} \left\{ \frac{g\alpha^2}{v_{air}\overline{\rho_a}}(\rho_{a10} - \rho_{a0}) \right\}^{1/3} & if\ \rho_{a10} - \rho_{a0} \geq 0 \end{cases} \tag{36}$$

Where the coefficient of free convection $c_{fr.conv}$ was calibrated as 0.14 (Deltares, 2020), the viscosity of air v_{air} is assumed 16.0 x 10^{-6} m^2/s, and the molecular diffusivity of air α is $\alpha = {}^{v_{air}}/_{\sigma}$ with $\sigma = 0.7$ the Prandtl number.

The saturated air density ρ_{a0} is expressed as Equation 37 and the remote air density ρ_{a10} is given by Equation 38.

$$\rho_{a0} = \frac{\frac{100P_{atm} - 100e_s}{R_{dry}} + \frac{100e_s}{R_{vap}}}{T_s + 273.15} \tag{37}$$

$$\rho_{a10} = \frac{\frac{100P_{atm} - 100e_a}{R_{dry}} + \frac{100e_a}{R_{vap}}}{T_{air} + 273.15} \tag{38}$$

Where R_{dry} is the gas constant for dry air (287.05 J/kg K) and R_{vap} is the gas constant for water vapor (461.495 J/kg K).

In addition, there is also the convective heat flux, which is split in two parts as the evaporative heat flux: a contribution by forced convection ($Q_{co,forced}$) and a contribution by free convection ($Q_{co,free}$), as expressed in Equation 39 (Deltares, 2020).

$$Q_{co} = Q_{co,forced} + Q_{co,free} \tag{39}$$

The sensible heat flux due to forced convection is given by Equation 40.

$$Q_{co,forced} = \rho_a c_p g(U_{10})(T_s - T_a) \tag{40}$$

Where c_p is the specific heat of air, considered to be 1,004.0 J/(Kg K). The wind-speed function $g(U_{10})$ is expressed as Equation 41.

$$g(U_{10}) = c_H U_{10} \tag{41}$$

Where c_H is the Stanton number, a calibration parameter.

Equation 42 describes the heat transfer for free convection.

$$Q_{co,free} = k_s \overline{\rho_a} c_p (T_s - T_a) \tag{42}$$

3.5.1.5 Transport equation

The transport equation formulated in a conservative form in Cartesian co-ordinates is given by Equation 43 (Deltares, 2020).

$$\frac{\partial(\Delta z_{m,n,k}c)}{\partial t}+\frac{1}{\Delta x\Delta y}\left\{\partial_x\left(uc\Delta y\Delta z_{m,n,k}\right)+\partial_x\left(vc\Delta x\Delta z_{m,n,k}\right)\right\}+(wc)_{m,n,k}-(wc)_{m,n,k-1}=$$
$$\frac{1}{\Delta x\Delta y}\left\{\partial_x\left[D_H\Delta y\Delta z_{m,n,k}\frac{\partial c}{\partial x}\right]+\partial_y\left[D_H\Delta x\Delta z_{m,n,k}\frac{\partial c}{\partial y}\right]\right\}+\left[D_V\frac{\partial c}{\partial z}\right]_{m,n,k}-\left[D_V\frac{\partial c}{\partial z}\right]_{m,n,k-1}-$$
$$\lambda_d\Delta z_{m,n,k}c+S \tag{43}$$

Where c is the matter or heat, λ_d represents the first order decay process and S the source and sink terms per unit area. Δx and Δy are the grid spaces in the physical space. D_H is the horizontal diffusion coefficient, and D_V is the vertical diffusion coefficient.

3.5.1.6 Drying and flooding criteria

Correctly reproducing the covering or uncovering of water level oscillations is an important feature of numerical flow models. When studying reservoirs that experience high water level variabilities, reproducing this oscillatory pattern is similar to those tidal movements, even though the temporal scale differs considerably. In order to represent this water level variabilities, numerical models remove or add grid cells based on drying criteria or on rising of the water.

For Delft3D, based on the value of the wetting threshold a drying one is settled, so changes of state in two consecutive time steps are avoided. Therefore, the user may specify the retention volume, which is the thickness of the water layer of a dry cell (Deltares, 2020).

3.6 Remote sensing evaporation model

Another tool available for evaporation analysis, aside from multidimensional models, are the techniques based on radar imaging (LINACRE, 1977, ZHANG *et al.*, 2017, ZHAO; GAO, 2019, RODRIGUES *et al.*, 2021a, GHAHREMAN; RAHIMZADEGAN, 2022). Multiple techniques are available, among those the Linacre (1977) model outstands as it can be used in a wide variety of climates to estimate evaporation and requires only two parameters: average air temperature (T) and dew point (T_d) (Equation 44). The T_d is obtained according to the relationship between air temperature and relative humidity, the second can be taken from the nearest weather station. According to Benzaghta *et al.* (2012), the Linacre equation (1977) tends to present better accuracy under semiarid conditions.

$$E = \frac{K_1 * \frac{Tm}{K_2 - A} + K_3 * (T - T_d)}{(K_4 - T)} \tag{44}$$

In Equation 36, Tm = T + 0.006*h, h is the altitude (m), A is the latitude in degrees, and K_1, K_2, K_3 and K_4 are parameters calibrated by Linacre (1977), their values being 700, 100, 15 and 80, respectively.

3.7 Stratification

Another fundamental process in reservoirs is the stratification of the water column as a result of temperature differences between surface and bottom layers. This process can be assessed by estimating the Potential Energy Anomaly (PEA) as described in Simpson *et al*., (1977). Overall, the power of analyzing PEA is that it can be applied both for outputs from multidimensional models and to measured data (DE BOER *et al*., 2008). The formulation used to estimate PEA is given in Equation 45. When PEA is a positive value, it indicates a stable stratification with the scalar representing the amount of energy per unit volume necessary to fully mix the water column, while a zero value means that the water column is fully mixed and negative values represent unstable stratification (HOFMEISTER *et al*., 2009), although the latter is not common in nature.

$$\varphi = \frac{1}{H}\int_{-h}^{\eta} (\bar{\rho} - \rho) gzdz \tag{45}$$

Where φ is the potential energy anomaly, ρ is the vertical density profile over the water column of depth H, given by $H = \eta + h$, η the free surface, h the location of bed, $\bar{\rho}$ the depth averaged density, z the vertical co-ordinate and g the gravitation acceleration.

4 MATERIALS AND METHODS

4.1 Study site

The study site of this work is Pentecoste reservoir (-39.3 °W -3.8 °S, weir crest elevation: 62 m), located in the Northeast region of Brazil in a semiarid climate (HASTENRATH, 2012), given by Figures 12 and 13.

Figure 12 - Image of Pentecoste reservoir (view of the East bank)

Source: Google Earth (2022)

Figure 13 - Image of Pentecoste reservoir (view of the West bank)

Source: Water Resources Management Company of Ceará State (COGERH)

This reservoir was selected because it has measurements of water level and temperature profiles available for calibration, along with a consistent bathymetry made by the Water Resources Management Company of Ceará State (COGERH). The field campaigns were made by COGERH using a YSI multiparameter probe between June 2012 and February 2013 every two weeks in the morning period, resulting in 18 days of dissolved oxygen, pH, salinity, total dissolved solids, water temperature, and Secchi depth measurement. No nictemeral campaigns were performed. Secchi depth ranged from 0.5 to 1.0 between 2012 and 2013. Water level and outflow measurements are available daily, and COGERH also performs sampling for water quality analysis every three months since 2008. Figure 14 brings all data of Total Phosphorus and Chlorophyll a concentration available for Pentecoste reservoir. The lake remains with high nutrient concentration with an increase in those measurements after 2012, which is the first year of an extended drought in this region (PONTES FILHO *et al*., 2020).

Figure 14 - Total Phosphorus and Chlorophyll a concentration at Pentecoste reservoir

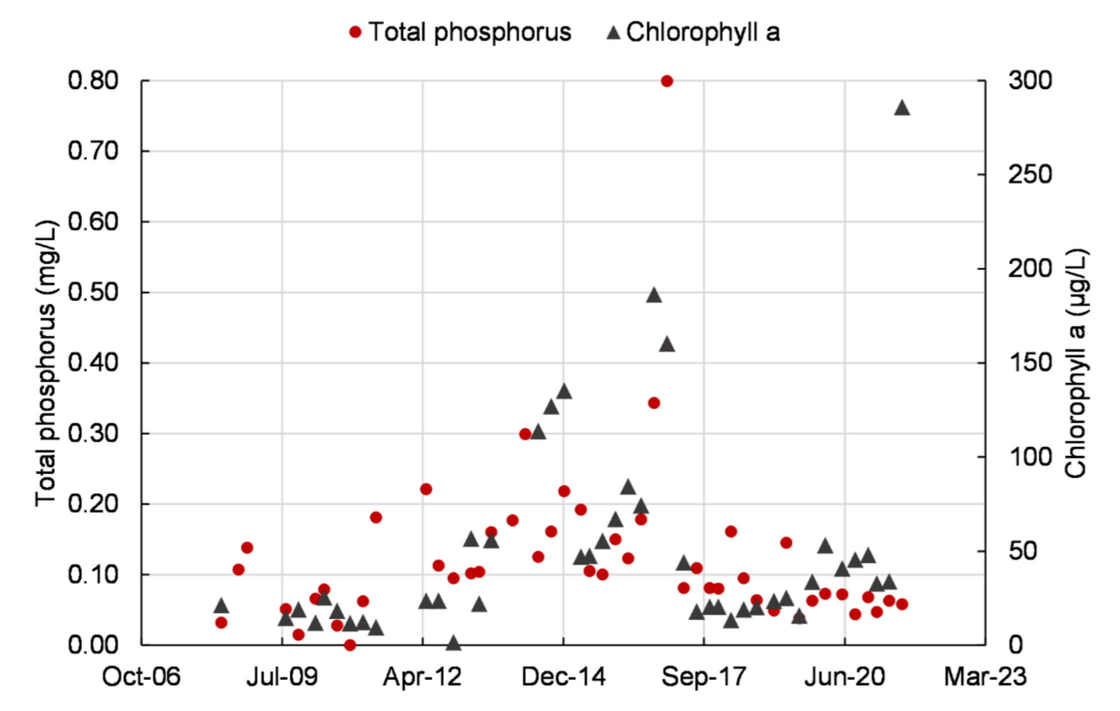

Regarding nutrient inlet from the surrounding environment, the catchment area of Pentecoste reservoir covers five different municipalities, namely Pentecoste (37,900 pop), Canindé (77,244 pop), Caridade (22,782 pop), Paramoti (12,252 pop), and Apuiarés (14,672 pop), which register livestock and farming non-industrial activities (IBGE, 2020). Most of the region is not covered by sewage systems (SNIS, 2020), therefore rivers and lakes receive this untreated inflow.. Different studies are developed in order to understand the inlet characteristics of reservoirs in Ceará state, along with modeling of water quality based on both measurement and hydrodynamics information such as residence time (LIMA NETO *et al*., 2022, ROCHA; LIMA NETO, 2021, 2022a,b).

Pentecoste reservoir is approximately 80 km west of the capital of Ceará State, Fortaleza, and it has multiple uses. Figure 15 shows the location of the study site. This reservoir has a maximum capacity of 360 hm³, a surface area of 46.64 km², maximum depth of 19.8 m, a mean depth of 6.5 m, and a catchment area of 3,090 km². Figure 16 gives a local description with elevation data, catchment area, and the nearest meteorological station from which data was collected. The area-volume-elevation curves are expressed as Figure 17.

Figure 15 - Study site scheme

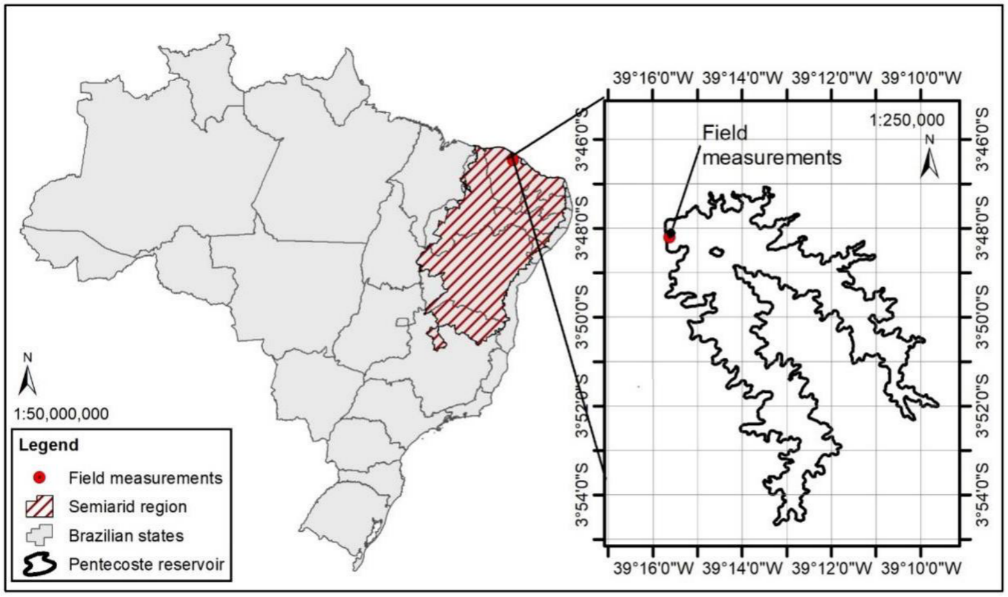

Figure 16 - Catchment area of Pentecoste reservoir and local elevation

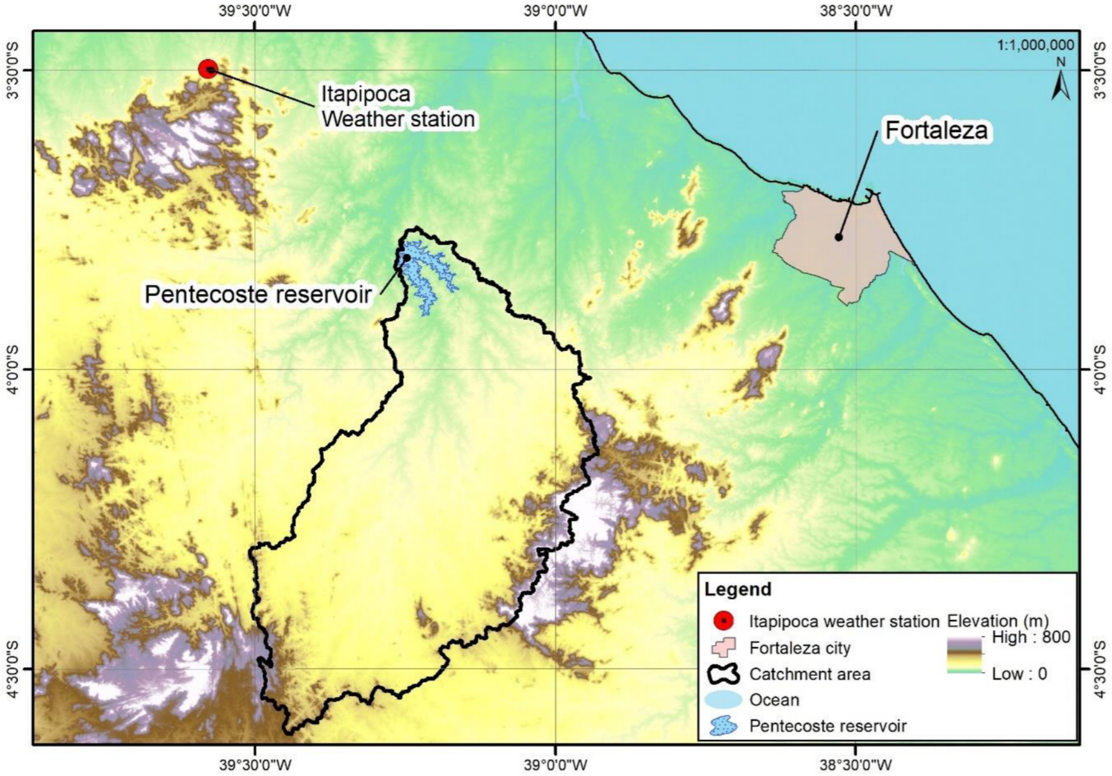

Figure 17 - Area-Volume-Elevation curve of Pentecoste reservoir

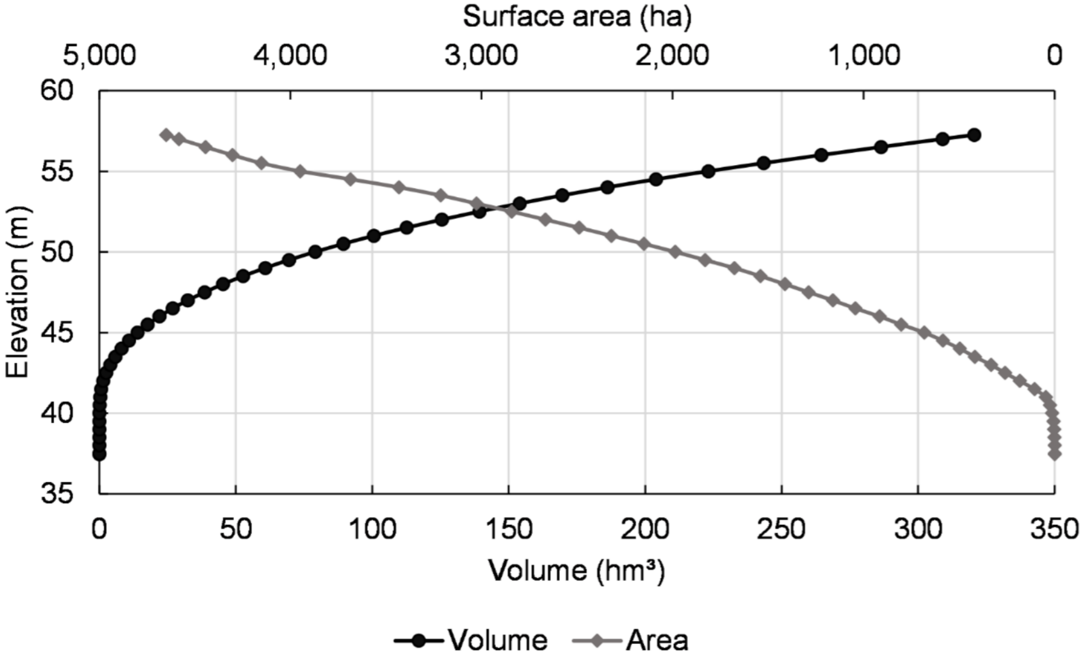

In addition, the integrated (zero dimensional) residence time of Pentecoste is approximately 13 months, and it has two main branches that come from intermittent rivers, named Canindé and Salgado, respectively West and East tributaries. In this region, the rainfall is typically concentrated between February and May (wet season), and the mean annual precipitation is of 820 mm. The mean air temperature is 27°C. Additionally, the wind speed, air temperature, rainfall, net radiation, inflow and outflow time series of the region are given by Figure 18. The 30-day moving average was plotted in order to elucidate seasonality. Figure 19 brings the wind rose from the nearest meteorological station, while Figure 20 gives the evaporation from a class A pan located in Fortaleza (80km from the reservoir).

Figure 18 - Meteorological conditions

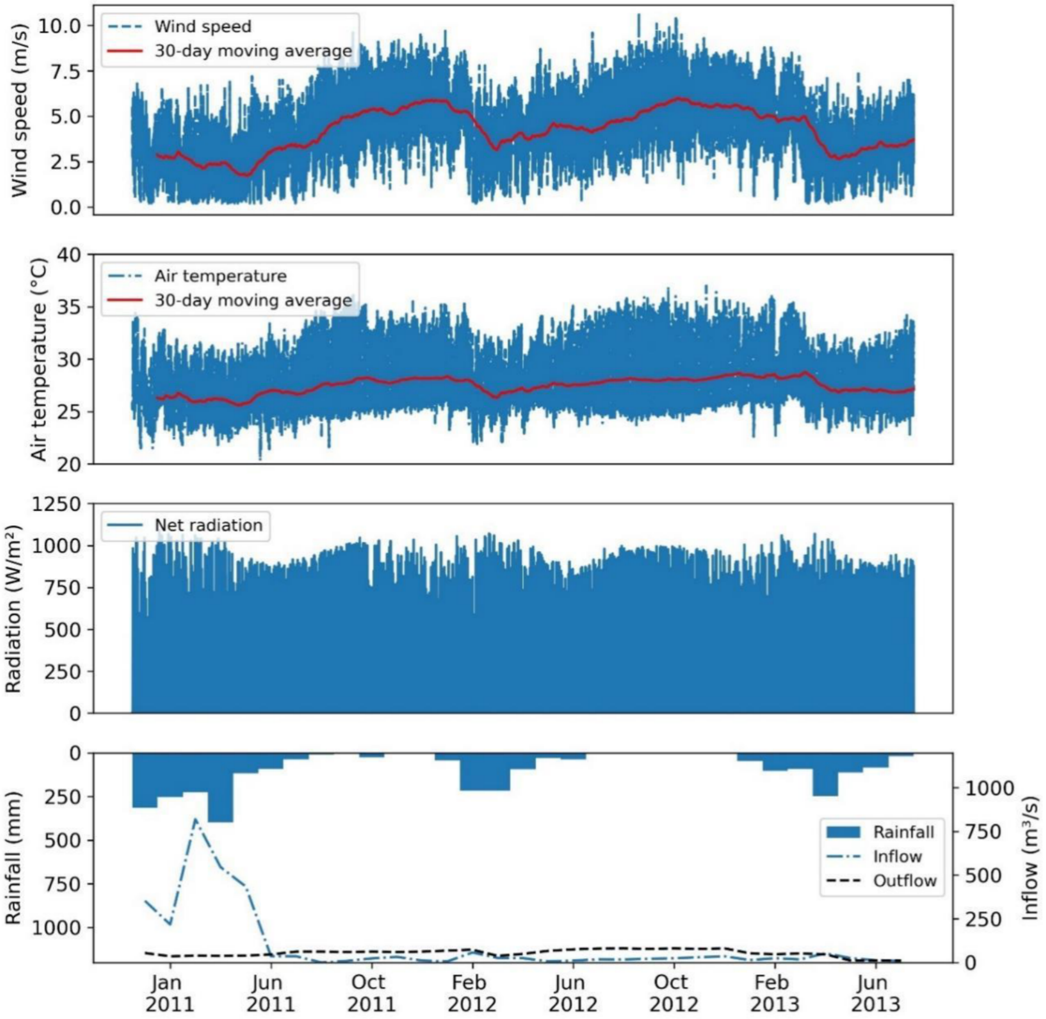

Figure 19 - Wind rose from the nearest meteorological station

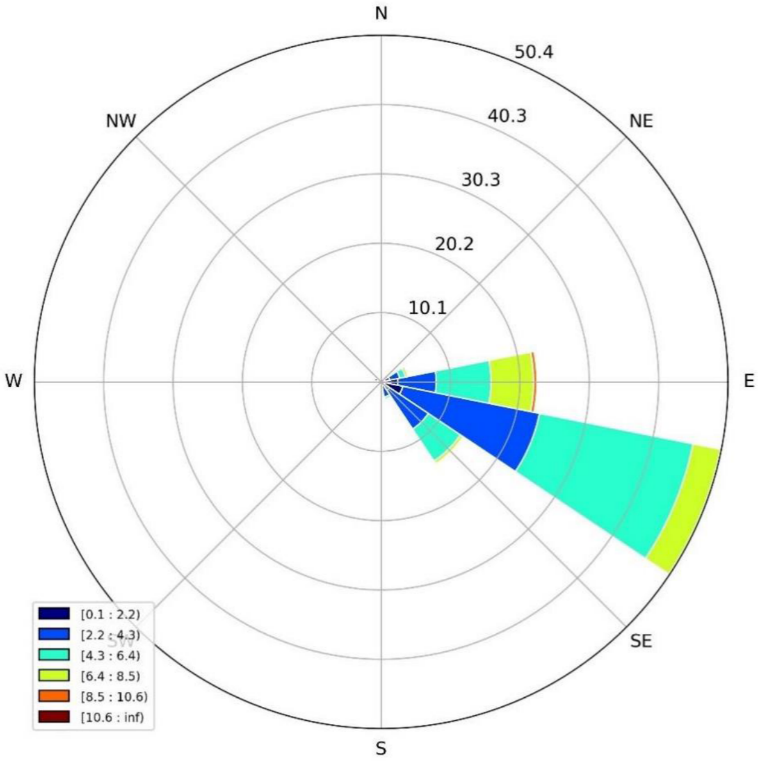

Figure 20 - Class A pan evaporation rate from the meteorological station of Fortaleza (80 km from Pentecoste reservoir)

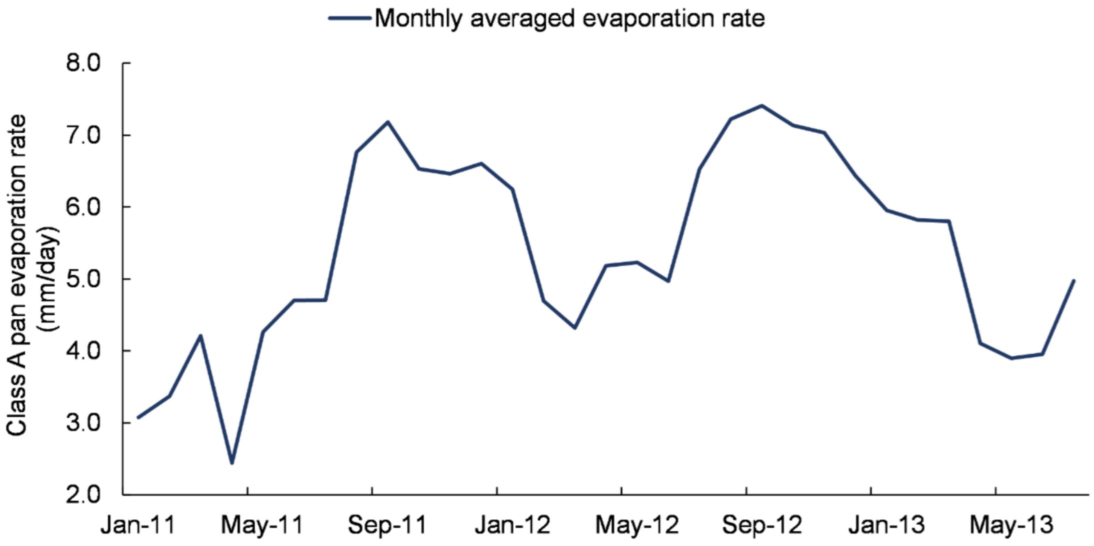

4.2 Delft3D description

Delft3D-FLOW (DELTARES, 2020) is a hydrodynamic model that can simulate bi and tridimensional unsteady flow or transport phenomena. It is suitable for flows with horizontal length and time scales much larger than vertical scales (DELTARES, 2020), and it is largely applied to lakes and reservoirs (DISSANAYAKE *et al*., 2019, OUNI *et al*., 2020, AMORIM *et al*., 2021, PICCIONI *et al*., 2021, PLEC *et al*., 2021, SHARAF *et al*., 2021). The numerical hydrodynamic modeling system solves the unsteady equations in two or three dimensions derived from the Reynolds Averaged Navier-Stokes equations for incompressible free surface flow. The vertical heat transport is a function of the depth and is calculated by taking into account the penetration of the short-wave radiation through the water column.

4.3 Delft3D model configuration

First, the simulation period was defined based on the availability of field measurement, warming phase, and amount of time needed for each run. This period begins in January 2011, which is one and a half year before the first campaign, and finishes in July 2013. Then, the reservoir's 2D mesh was created using a curvilinear grid (Figure 21), resulting in 184 points in M direction and 120 points in N direction with a uniform configuration. The Z model was chosen for the study as it is adequate for weakly forced stratified water systems (DELTARES, 2020). A maximum of 19 layers was set up with vertical layers with approximately 1 meter, and the difference between the expected and modeled volumes was of 2%.

Numerical stability was reached with a timestep of 1.5 min. The initial conditions were set up as uniform according to the measurement of water level in the first simulation day, and to the mean air temperature of the simulation period for water temperature. Salinity was set to the mean of the available measurements. Bottom roughness was computed using Chézy's formulation with the default coefficient value of 65 $m^{1/2}s^{-1}$ (Deltares, 2020). Background vertical viscosity and diffusivity were set to zero, so the model computes the values from the turbulence model (Deltares, 2020). The background horizontal viscosity and diffusivity were set to 1 m^2s^{-1} and 2 m^2s^{-1}, respectively, in order to achieve a turbulent Schmidt number of 0.5, knowing this is in the expected range for water (LIN; SHIONO, 1995, TOMINAGA; STATHOPOULOS, 2007, GUALTIERI *et al*., 2017) and that those are computed values by

Delft3D. The k-ε closure model was used to compute turbulent eddy viscosity and diffusivity. Also, the default threshold value for the drying and flooding criteria of 0.1m was used.

As for the heat fluxes, the Ocean model was chosen and it requires as input the time series for relative humidity [-], air temperature [°C], cloud coverage [-], and solar radiation [W m^{-2}]. Secchi depth was set as the mean value of the measurements. Dalton and Stanton numbers are calibration parameters.

Figure 21 - 3D model setup

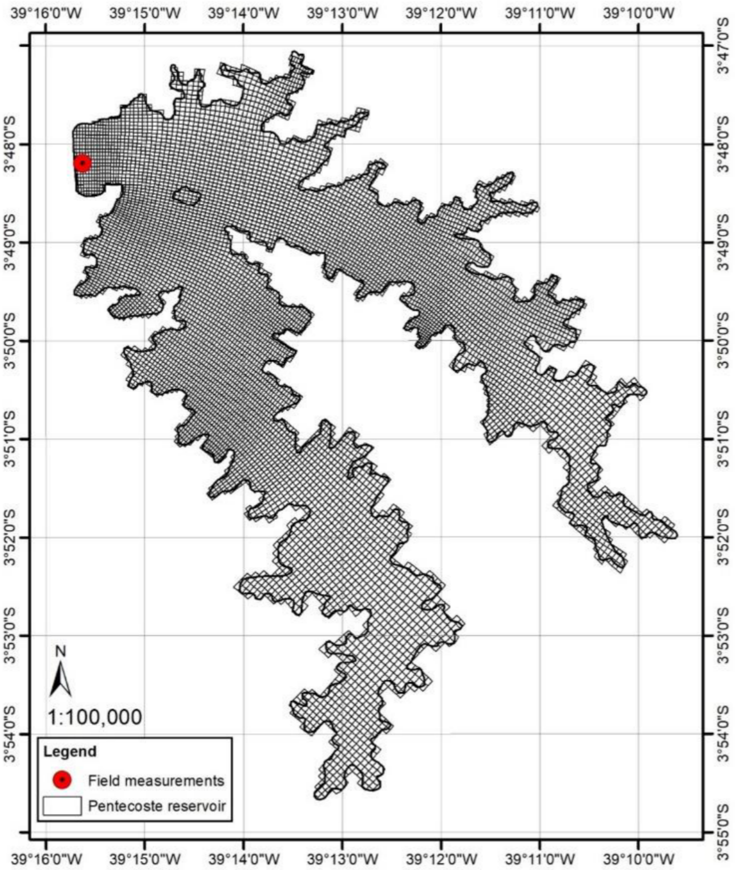

4.4 Delft3D processing time and post-processing tools

Regarding processing time, each model run took 1 day and 15 hours to finish, using a computer with an Intel(R) Core (TM) i5-8265U CPU @ 1.60 GHz processor with 8GB of RAM in a 64-bit operational system. The relation between simulation period and processing time is approximately 580, meaning one day of processing is needed to run 580 days of simulation. It was necessary to run the model around 35 times in order to achieve acceptable results. The post-processing of data was made using both Quickplot from Delft3D and a routine in Python.

4.5 Delft3D Input data

The meteorological forcing for this study comes from an automated meteorological station located 52 km from the study area and operated by the National Meteorological Institute (INMET). The data consisted of hourly time series of wind speed [m s^{-1}], wind direction [°], relative humidity [-], air temperature [°C], and solar radiation [W m^{-2}]Cloud cover is already accounted in the solar radiation time series, so it was set to zero. Solar radiation data was increased by 15% in order to correctly calibrate the water budget. Data gaps were less than 1% for all the variables and they were filled with mean values of each forcing. The inflow temperature was estimated as the mean air temperature of the region (27.4 °C).

The Water Resources Management Company of Ceará State (COGERH) daily gathers and processes data for estimating the reservoir's inflow by the water budget equation. In addition to that, as the inflow for the reservoir comes from two main rivers, it is necessary to make an estimation of how much of the total inflow enters the lake from each branch. For that, a weighting using rainfall and catchment area was developed (Equation 44). Each tributary was implemented in Delft3D as a single discharge. The rainfall was estimated by the Thiessen Method using a R routine, and the gaps were filled using linear regression. The rain gauges with over 5% of gaps were excluded from the analysis. Knowing that the study site is located in a semiarid region where in the majority of days no rainfall is noted, the weigh was developed monthly.

$$Q_{river\_i} = Q_{total} \cdot \left(\frac{A_{catchment\_i} \cdot P_{catchment\_i}}{A_{total} \cdot P_{total}}\right) \tag{44}$$

Where Q_{river_i} is the inflow from the analysed river [m^3 s^{-1}], Q_{total} is the total inflow [m^3 s^{-1}], $A_{catchment\_i}$ is the catchment area of the analysed river [km^2], $P_{catchment\_i}$ is the precipitation of the analysed catchment area [mm], A_{total} is the total catchment area of Pentecoste reservoir [km^3], and P_{total} is the precipitation of the total catchment area of Pentecoste reservoir.

4.6 Accuracy evaluation for Delft3D

Calibration was performed manually with the performance of the model verified with field data of water level and temperature profiles, when available. Water level measurements were available daily for all the simulation period, without gaps. As for temperature profiles, eighteen field campaigns were made every two weeks between June 2012 and February 2013, with measurements at each 0.5 m.

Multiple goodness of fit methods were used to compare modeled and measured data: root mean square error (RMSE), mean square error (MAE), normalized mean square error (NMAE), and coefficient of determination (r^2), respectively Equations 45, 46, 47 and 48. Knowing that the aim of the study is to understand the hydrodynamics’ processes and to compare the evaporation results for the simulation period, along with the limited days of temperature profiles measurements, all the measured data was used for calibration.

$$RMSE = \sqrt{\frac{1}{n}\sum_{i=1}^{n}(x_i - \widehat{x_i})^2} \tag{45}$$

$$MAE = \frac{\sum_{i=1}^{n}|(x_i - \widehat{x_i})|}{n} \tag{46}$$

$$NMAE = \frac{\sum_{i=1}^{n}|(x_i - \widehat{x_i})/\widehat{x_i}|}{n} \tag{47}$$

$$r^2 = \frac{\left[\sum_{i=1}^{n} x_i\widehat{x_i} - \frac{(\sum_{i=1}^{n} x_i)(\sum_{i=1}^{n} \widehat{x_i})}{n}\right]^2}{\left[\sum_{i=1}^{n} x_i{}^2 - \frac{\left(\sum_{i=1}^{n} x_i\right)^2}{n}\right]\left[\sum_{i=1}^{n} \widehat{x_i}{}^2 - \frac{\left(\sum_{i=1}^{n} \widehat{x_i}\right)^2}{n}\right]} \tag{48}$$

Where x_i is the predicted value, $\widehat{x_i}$ is the measured value, and n is the number of observations.

Furthermore, the evaporation rates modelled by Delft3D and the evaporation model of Linacre (1977) were compared by relative deviation, as the evaluation is made for averaged evaporation rates in each of the analyzed days.

4.7 Evaporation model of Linacre (1977)

For the estimation of evaporation by the Linacre (1977) model, altitude data was obtained by using the *Shuttle Radar Topography Mission* (SRTM). In order to apply the evaporation model, air temperature calculations were divided into two stages, i) calculation of the surface temperature (AVDAN; JOVANOVSKA, 2016; MALARET *et al*., 1985) and later of the ii) air temperature (DUGDALE *et al*., 2017).

The algorithm of Malaret *et al*. (1985) was used for the Landsat 5, while the one developed by Avdan and Jovanovska (2016) was employed for Landsat 8. Both algorithms estimate the surface temperature, but Linacre (1977) requires air temperature as one of the input data. According to Dugdale *et al*. (2017), air temperature (T) can be assumed to be 20% higher than water temperature in equatorial regions, and this recommendation was adopted.

4.8 Comparison of evaporation models of Delft3D and Linacre (1977)

The evaporation model of Linacre (1977) uses satellite images taken at 12:30 pm, while the Delft3D has an output at each 2 hours, therefore the results were obtained for 12:00 pm. For this study three days in the simulation period are available for comparison, those being April 7th, 2011, May 30th, 2013, and July 1st, 2013.

Based on this, the evaluation was made both for the averaged evaporation losses and for the spatial distribution of evaporation rates for those days. For proceeding with the daily averaged evaporation rate comparison between the models, it is necessary to calculate the mean value of the evaporation rates estimated for each model cell when analyzing the Delft3D output, and for each pixel value regarding the remote sensing result.

4.9 Estimation of Potential Energy Anomaly

The potential energy anomaly (PEA) of the water column was calculated for the point in which the field measurements were performed, in order to compare the results from modeling with the ones from the measurements. A discrete formulation of Equation 43 was applied, with the water density as an output of Delft3D and being estimated from temperature for the measurements, the latter following Dingjman (2015), Equation 49.

$$\rho = 1{,}000 - 0.019549 \cdot |T - 3.98|^{1.68} \tag{49}$$

Where ρ is the water density [kg/m³], and T is the water temperature [°C].

5 RESULTS AND DISCUSSION

5.1 Accuracy evaluation – Delft3D

The parameters adjusted for representing Pentecoste reservoir are described by Table 1 along with their default values. Figure 22 shows the results for calibration of the water level. The water budget of Pentecoste reservoir was reproduced as a high coefficient of correlation indicates that all level variation throughout the simulation period was noted, and both RMSE and MAE low values confirm the good adherence of the model to the measurements, similar to that of Sharaf *et al*. (2021) and Wang *et al.* (2022). Accordingly to Sharaf *et al*. (2021), a good model representation of the water levels of a reservoir is crucial to accurately reproducing its thermal structure.

Additionally, the high oscillation observed in the water level of Pentecoste reservoir follow the expected from semiarid reservoirs, as this region has a known characteristic that almost all the annual rainfall is concentrated in a few months of the year (HASTENRATH, 2012; HOUNOU-GBO *et al*., 2019). Interestingly, water level is only lowering after the rainfall events of 2011, with a discrete maintenance of the level in the beginning of 2012. This fact is explained by the extended drought that started in 2012 for this region (PONTES FILHO *et al*., 2020), considerably affecting the inflow of the reservoir.

Table 1 - Default and calibrated parameters used in the hydrodynamic model

Parameter	Default value	Calibrated value
Wind drag coefficient [-]	6.30E-04	6.30E-04
Horizontal eddy viscosity [m²/s]	10.00	1.00
Horizontal eddy diffusivity [m²/s]	10.00	2.00
Vertical eddy viscosity [m²/s]	1.00E-06	0.00
Vertical eddy diffusivity [m²/s]	1.00E-06	0.00
Secchi depth [m]	2.00	0.60
Dalton number [-]	1.30E-03	1.50E-03
Stanton number [-]	1.30E-03	5.00E-03

Figure 22 - 3D model water level accuracy evaluation

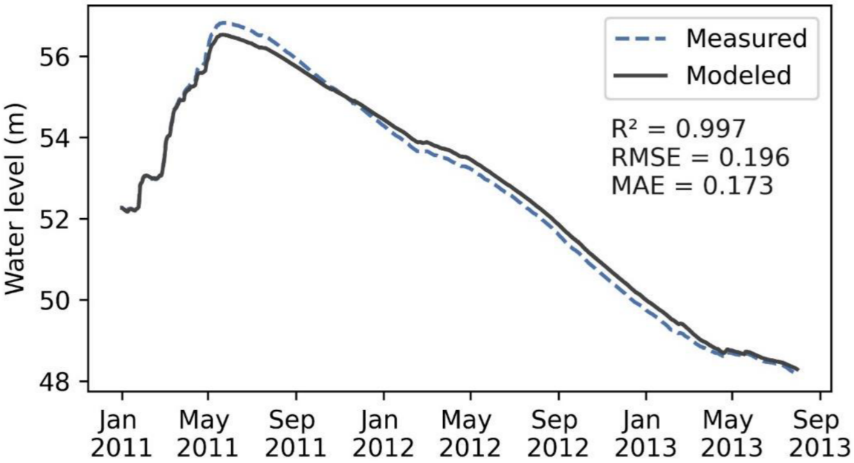

When analyzing the meteorological time series for this period (see Figure 18) along with the water level, it is notable that, for the second semester of 2012 (dry season), the region registered higher wind velocities and lower water levels than in the wet period, which favors the mixing of the water column. This is in agreement with Curtarelli *et al*. 2014, that found surface circulation driven by wind force (reservoir located in the center region of Brazil with surface area of 814 km² and maximum depth of 78 m), and Valdespino-Castillo *et al*. 2014, who found mixing enhancement of a water body under strong water level fluctuation in the central Mexican highlands with surface area of 18.55 km² and mean depth of 21.1 m. Also, Zhang *et al*., (2020) assessed the thermal structure of a water body and showed that it depends on both the water depth and wind conditions (reservoir located in Australia with 3.6 km² surface area and maximum depth of 23 m). Therefore, a mixed water column condition is expected to occur in the dry season in Pentecoste reservoir, with low temperature differences between surface and bottom layers.

Figure 23 shows the comparison between modeled and measured temperature profiles of Pentecoste reservoir while in Table 2 the goodness of fit methods are presented in comparison with other studies (see DISSANAYAKE *et al.*, 2019, POLLI; BLENINGER, 2019, ZHANG *et al*., 2020, AMORIM *et al*., 2021, PICCIONI *et al*., 2021, PLEC *et al*., 2021). The calibration results for the multiple goodness of fit methods are as follows for the full water column: MAE of 0.539 °C, RMSE of 0.572 °C, and NMAE of 0.008. For water surface temperature the mean values are: MAE of 0.618 °C, RMSE of 0.491 °C, and NMAE of 0.021. For the bottom temperature the results are: MAE of 0.534 °C, RMSE of 0.355 °C, and NMAE of 0.019. It can be observed that the model begins with accurate reproduction of the thermal structure, as stratification processes are noted along with different moments of thermocline breakdowns (see days in July and September of Figure 23). Contrastingly, in the last days of the calibration period the model is colder than the observed measurements, with the temperature differences between surface and bottom layers no longer fairly reproduced. This fact is further discussed in Section 5.3.

In Table 2 it can be seen that the overall results from this research are in agreement with other studies, even though the r^2 from surface and water temperatures do not show high correlation. This might be due to the cooling of the water column as the water level diminishes, knowing that the temperature time series from Delft3D starts to lower and stabilize at a certain point of the simulation, while by analyzing the measurements the tendency in the same period is marked by a discrete increase. Figure 24 shows the surface and bottom temperature evolution from Delft3D and measurements, where the previous discussion can be clearly observed.

Figure 23 - Typical modeled and measured temperature profiles for Pentecoste reservoir

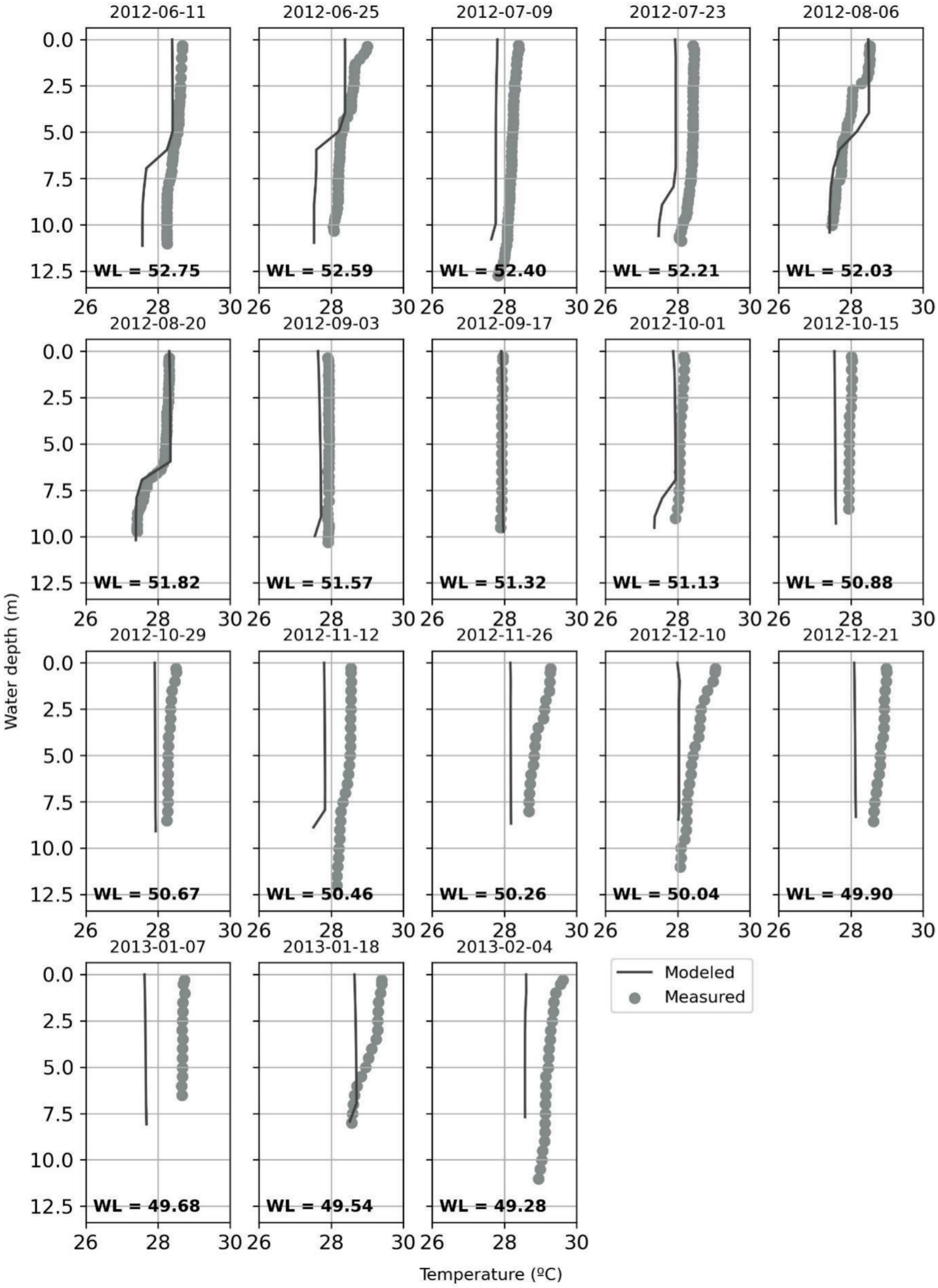

Table 2 - Comparison of the goodness of fit methods with other studies

Study	**Lake**	**Location**	**Maximum depth [m]**	**Surface area [km²]**	**Analysis**	**Metric**	**Result**	**This study**
AMORIM *et al*. (2021)	Hedberg Lake	Brazil	5.00	0.26	Surface temperature (Validation period)	RMSE	0.86 [°C]	0.4900
AMORIM *et al*. (2021)	Hedberg Lake	Brazil	5.00	0.26	Bottom temperature (Validation period)	RMSE	0.43 [°C]	0.3600
AMORIM *et al*. (2021)	Hedberg Lake	Brazil	5.00	0.26	Surface temperature (Validation period)	NMAE	0.32 [-]	0.0203
AMORIM *et al*. (2021)	Hedberg Lake	Brazil	5.00	0.26	Bottom temperature (Validation period)	NMAE	0.28 [-]	0.0154
AMORIM *et al*. (2021)	Billings Reservoir	Brazil	18.00	127.00	Surface temperature (Validation period)	RMSE	0.39 [°C]	0.4900
AMORIM *et al*. (2021)	Billings Reservoir	Brazil	18.00	127.00	Bottom temperature (Validation period)	RMSE	0.45 [°C]	0.3600
AMORIM *et al*. (2021)	Billings Reservoir	Brazil	18.00	127.00	Surface temperature (Validation period)	NMAE	0.0015 [-]	0.0203
AMORIM *et al*. (2021)	Billings Reservoir	Brazil	18.00	127.00	Bottom temperature (Validation period)	NMAE	0.005 [-]	0.0154
POLLI and BLENINGER (2019)	Vossoroca Reservoir	Brazil	17.00	3.30	Full water column temperature	MAE	0.50 +- 0.31 [°C]	0.54+- 0.23
DISSANAYAKE *et al*. (2019)	Upper Lake Constance	Germany	252.00	470.00	Full water column temperature (ELCOM)	RMSE	0.58 [°C]	0.5721
DISSANAYAKE *et al*. (2019)	Upper Lake Constance	Germany	252.00	470.00	Full water column temperature (DELFT)	RMSE	0.49 [°C]	0.5721
PICCIONI *et al*. (2021)	Lake Champs-sur-Marne	France	3.50	0.12	Surface temperature (Validation period)	RMSE	1.00 [°C]	0.4900
PICCIONI *et al*. (2021)	Lake Champs-sur-Marne	France	3.50	0.12	Bottom temperature (Validation period)	RMSE	0.96 [°C]	0.3600
PLEC *et al*. (2021)	Lake Pampulha	Brazil	16.00	2.00	Surface temperature (Validation period)	RMSE	0.45 [°C]	0.4900

Study	Lake	Location	Maximum depth [m]	Surface area [km²]	Analysis	Metric	Result	This study
PLEC *et al*. (2021)	Lake Pampulha	Brazil	16.00	2.00	Bottom temperature (Validation period)	RMSE	0.24 [°C]	0.3600
PLEC *et al*. (2021)	Lake Pampulha	Brazil	16.00	2.00	Surface temperature (Validation period)	r^2	0.63 [-]	0.4500
PLEC *et al*. (2021)	Lake Pampulha	Brazil	16.00	2.00	Bottom temperature (Validation period)	r^2	0.81 [-]	0.5600
ZHANG *et al*. (2020)	Tarago Reservoir	Australia	23.00	3.60	Surface temperature	RMSE	0.689 [°C]	0.4900
ZHANG *et al*. (2020)	Tarago Reservoir	Australia	23.00	3.60	Surface temperature	r^2	0.963 [-]	0.4500
ZHANG *et al*. (2020)	Tarago Reservoir	Australia	23.00	3.60	Bottom temperature	RMSE	0.614 [°C]	0.3600
ZHANG *et al*. (2020)	Tarago Reservoir	Australia	23.00	3.60	Bottom temperature	r^2	0.949 [-]	0.5600

Figure 24 - Surface and bottom temperatures for calibration period

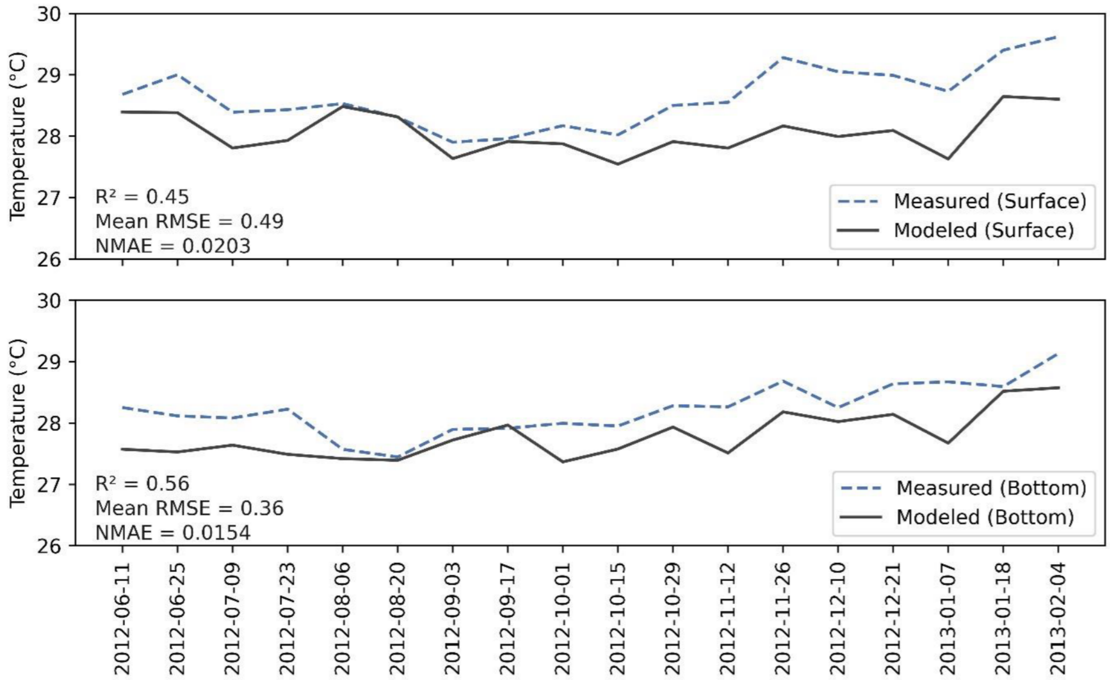

5.2 Average evaporation rates

Figure 25 shows the monthly averaged evaporation rates at the sampling point, which is located near the dam. The seasonal pattern shows higher evaporation rates consistently observed in the dry period, when higher wind velocities and air temperatures are noted (see meteorological conditions in Figure 18). This pronounced seasonality is expected for semiarid regions, with similar pattern noted by Alazard *et al*. (2015) in a Tunisian reservoir and in Benzaghta *et al*. (2012) results in a Libyan lake, where the seasonal patterns in evaporation rates is notable.

Figure 25 - Monthly averaged evaporation rates at the sampling point in Pentecoste reservoir

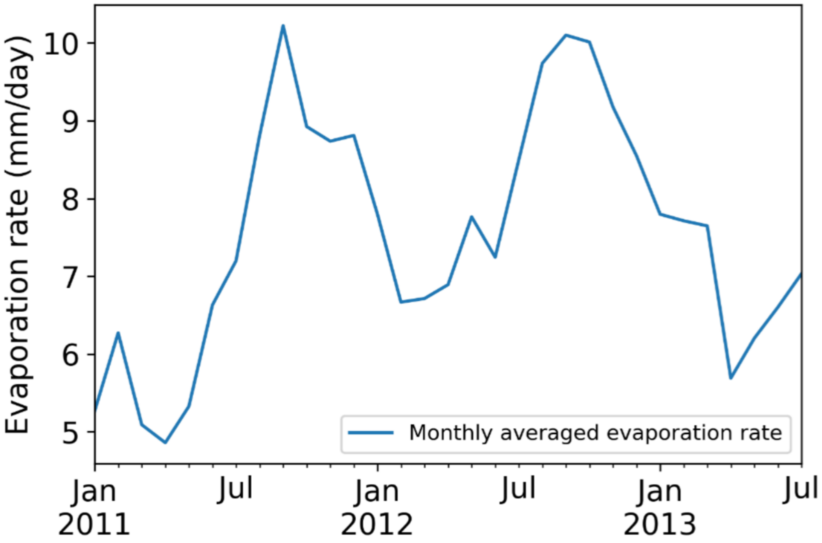

In Figure 26 the correlation between evaporation rates and both air temperature and wind speed are presented. Based on the evaluation criteria for field scale proposed by Moriasi *et al*. (2015) at a monthly temporal scale, the coefficient of correlation between evaporation rates and air temperature (r^2 of 0.736) is classified as satisfactory, while for wind speed (r^2 of 0.853) the classification is very good. In agreement to this result, Ghahreman and Rahimzadegan (2022) discusses that, for two reservoirs located in arid environment, wind speed is a main driver for evaporation as, with the increase of water vapor in the evaporating surface, the surrounding air becomes saturated and then wind speed moves the humidity bringing the drier air. On the other hand, Mesquita *et al*. (2020) found no relevant correlation between the Class A pan coefficient and the climate of a tropical reservoir in a seasonal scale, although on the annual evaluation correlation was noted. Also, Rodrigues et al. (2021a) found low correlations between evaporation and air temperature, with r^2 ranging from 0.09 to 0.14 for the four analyzed water bodies in the semiarid region of Brazil, while for wind speed those correlations were moderate, ranging from 0.37 to 0.42.

In this context, the results of Pentecoste reservoir indicate a strong correlation between evaporation rates and meteorological conditions of air temperature and wind speed. This is a potential tool for water management, as the equations proposed can be used by the local agency COGERH to better understand the evaporation losses, since periodic field campaigns are performed by the Company in order to monitor in-lake water quality and surrounding conditions.

Figure 26 - Scatter plot and coefficient of correlation between monthly evaporation rates and (a) air temperature and (b) wind speed

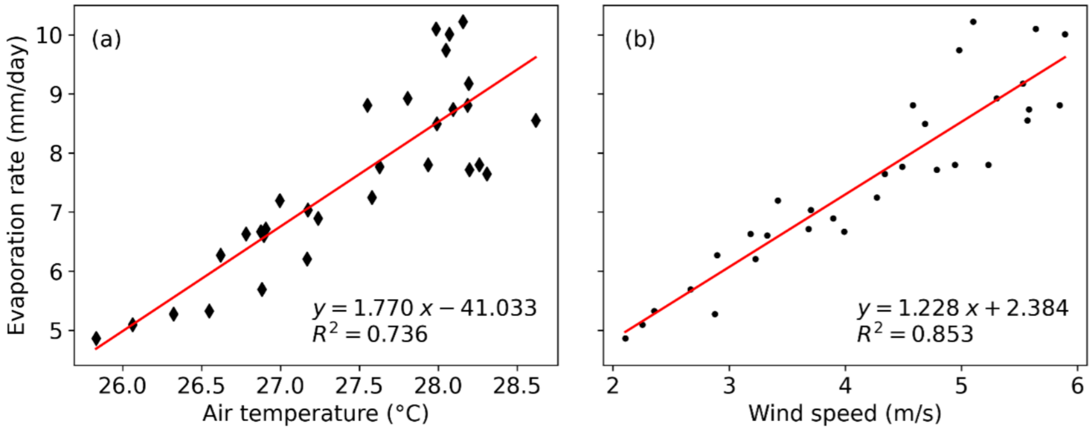

Furthermore, in this study the evaporation model of Linacre (1977) is used as the reference method since Rodrigues *et al.* (2021a) demonstrated good results for the Brazilian semiarid region. In this document the use of the abbreviation RS stands for remote sensing and is referring to the Linacre (1977) evaporation model. Figure 27 shows the comparison between evaporation rates estimated by Delft3D and RS. This is an innovative evaluation not found in previous studies. Actually, Sharaf *et al*. (2021) made a combined evaluation of the thermal regime of a semiarid reservoir located in Lebanon using remote sensing and tridimensional modeling approaches, but evaporation rates were not assessed. Also, Curtarelli *et al*. (2014) applied remote sensing techniques in order to estimate inflow temperatures to improve the setup of a tridimensional model, although no comparisons of the results were assessed.

Additionally, multiple studies investigate surface water temperatures by using remote sensing data in order to estimate evaporation rates and its spatial distribution on the reservoir (ZHANG *et al.*, 2017, ZHAO; GAO, 2019, RODRIGUES *et al*., 2021a, RODRIGUES *et al*., 2021b, GHAHREMAN; RAHIMZADEGAN, 2022), but few apply multidimensional models for this purpose. Among these, Mesquita *et al.* (2020) and Lee *et al*. (2018) evaluated the evaporation rates in tropical lakes using a bidimensional model, but it does not allow the study of spatial distribution. On a different way, Elhakeem *et al*. (2015) assessed the seasonal surface variability of evaporation in a marine system, but, contrastingly to this study, the time series of evaporation rates was a model input. No other study that applies multidimensional models to simulate evaporation rates on reservoirs was found in the literature. Figure 27 brings the comparison of the total evaporation rates estimated by Delft3D and RS. Both models showed very close estimations for daily evaporation rates, with the higher deviation being noted in 30-May-2013. It can be seen that the two different models based on different principles accomplished to find similar results for the same parameter, which elucidates the accuracy of both methods.

Figure 27 - Comparison between RS and Delft3D estimated daily evaporation

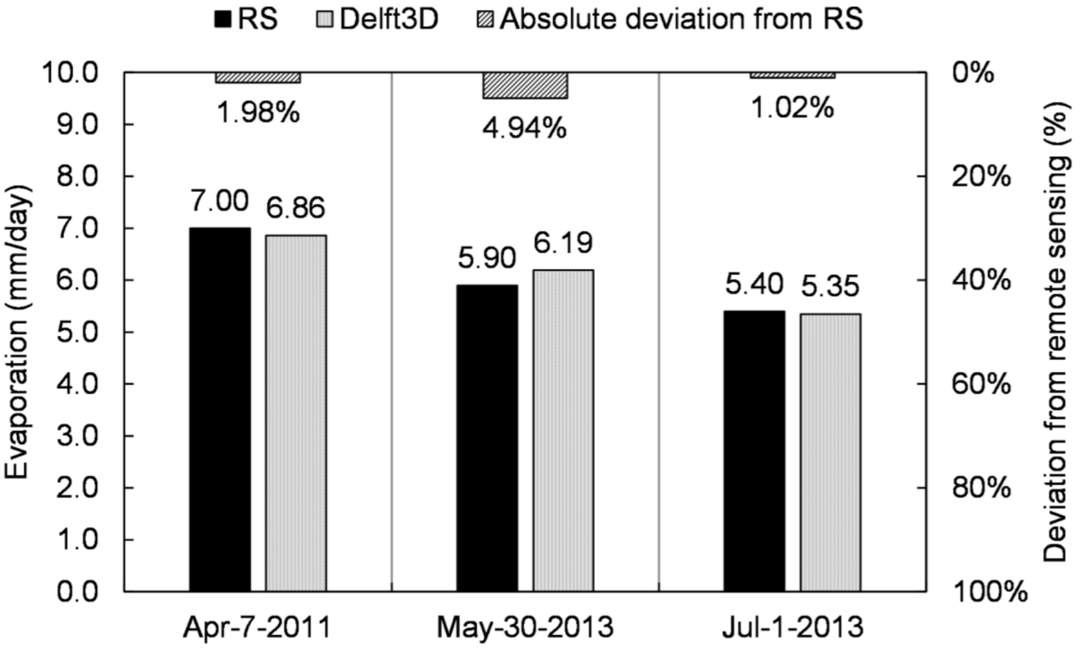

Figure 28 shows the monthly rainfall from the nearest meteorological station highlighting the months in which evaporation rates were analyzed. Seasonality is evident, with almost all the precipitation events concentrated in the first months of each year. From the observed days, 7-Apr-2011 is in the wet season, while 30-May-2013 is already in the end of the rainfall period, and 1-Apr-2013 is in the dry period. Notably low precipitation events occur due to the drought period that started in 2012 and ended in 2018 for this region (PONTES FILHO *et al*., 2020).

Additionally, another important information is the water level of the lake on the analyzed days. A significant drop in the water level of Pentecoste reservoir occurs between April of 2011 and May of 2013 (see Figure 22), as it fell from 55.2 m in April to 48.7 m in May, representing a drawdown of 6.5 m on the water level followed by a 60% drop on the surface area and 74% on the lake's volume. Contrastingly, Valdespino-Caspillo *et al*. (2014) observed a 10 m drop on the water level of a Mexican reservoir with maximum depth of 35 m, which highlights the relevance of Pentecoste's water level drawdown.

Figure 28 - Monthly rainfall with highlights on the months of interest

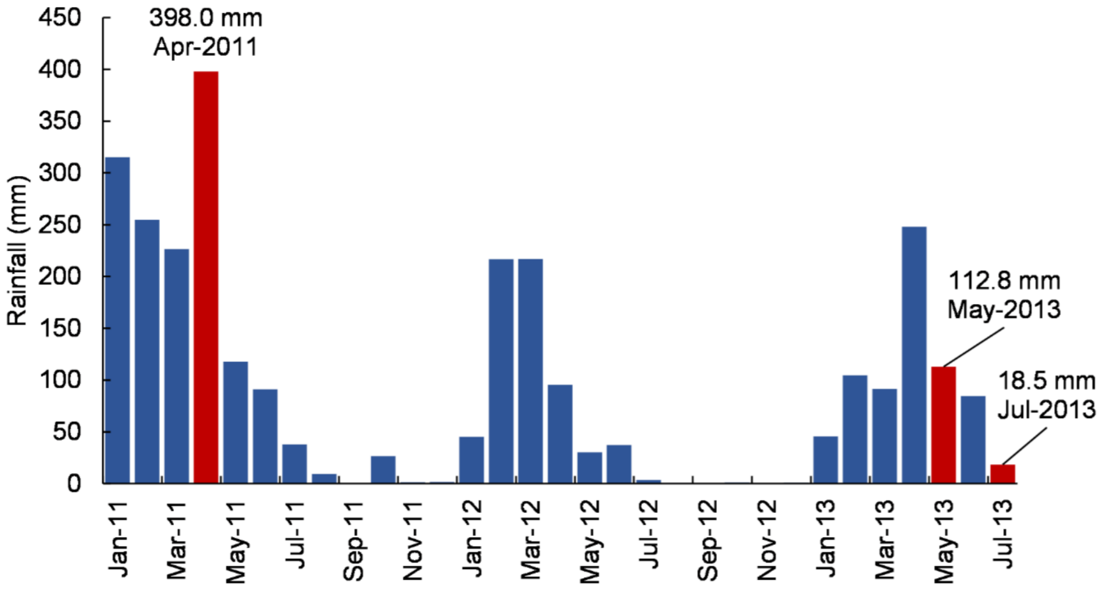

5.3 Spatial distribution of evaporation rates

Figure 29 gives the temporal evolution of the surface distribution of evaporation rates from Delft3D, and Figure 30 compares the spatial distribution of evaporation results between Delft3D and RS. On the Delft3D maps the boundary of the water surface area from the RS model is plotted. Here, an interesting fact was noted on the Delft3D modeling results. From a model perspective, Delft3D assumes that, when the water level of a given layer cell is under a threshold value, no velocities, hence no momentum, is transferred laterally between two adjacent cells. In this condition, the water can only move out of the so-called inactive cell by the surface layer, i. e. by evaporation. Therefore, inactive cells containing water may exist in the model and they are part of the water balance. In practice, they may be interpreted as moisture in the soil adjacent to the lake itself. Those cells tend to retain more heat and register higher evaporation rates than those in the deeper region of the reservoir, as shallower regions are susceptible to faster heating (BIGLARBEIGI *et al*., 2018, FRIEDRICH *et al*., 2018). This process is seen in Figure 29 and Figure 30 (a.i), (b.i) and (c.i), as it gets more intense for the days with the lower water levels, knowing that the lower the water surface area, the more energy is retained in the borders.

Figure 29 - Temporal evolution of the surface distribution of evaporation rates

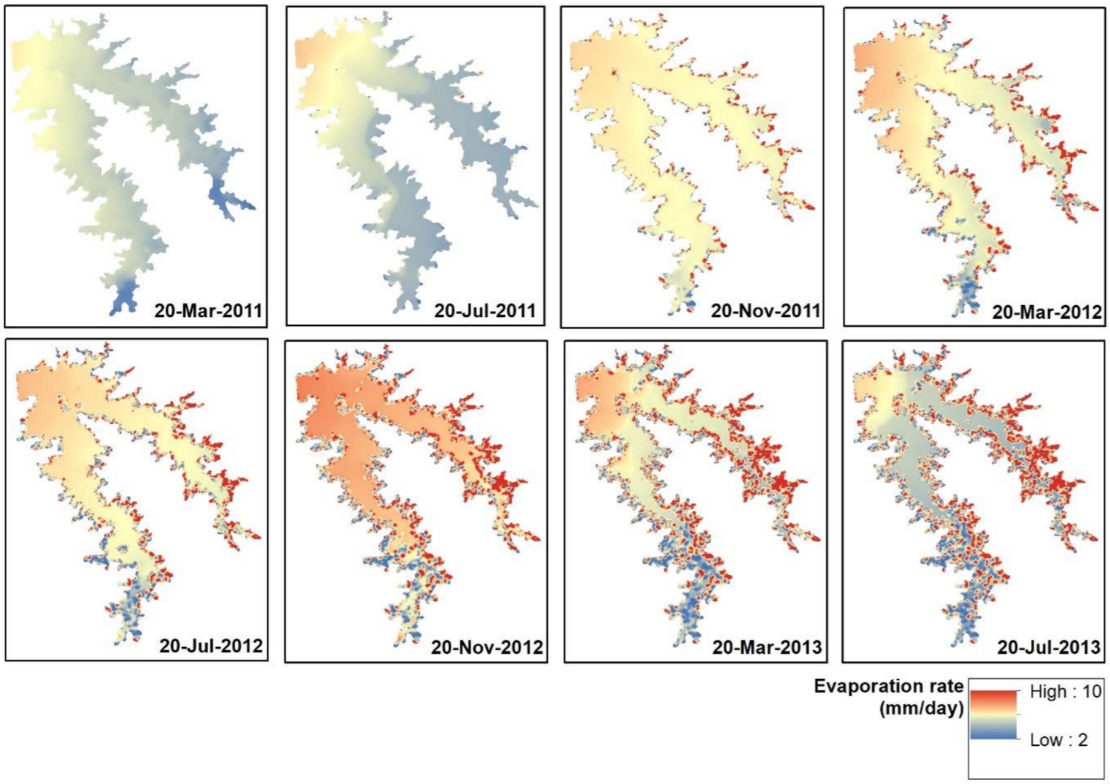

Figure 30 - Spatialized evaporation rates from (a.i), (b.i), (c.i) Delft3D and (a.ii), (b.ii), (c.ii) RS

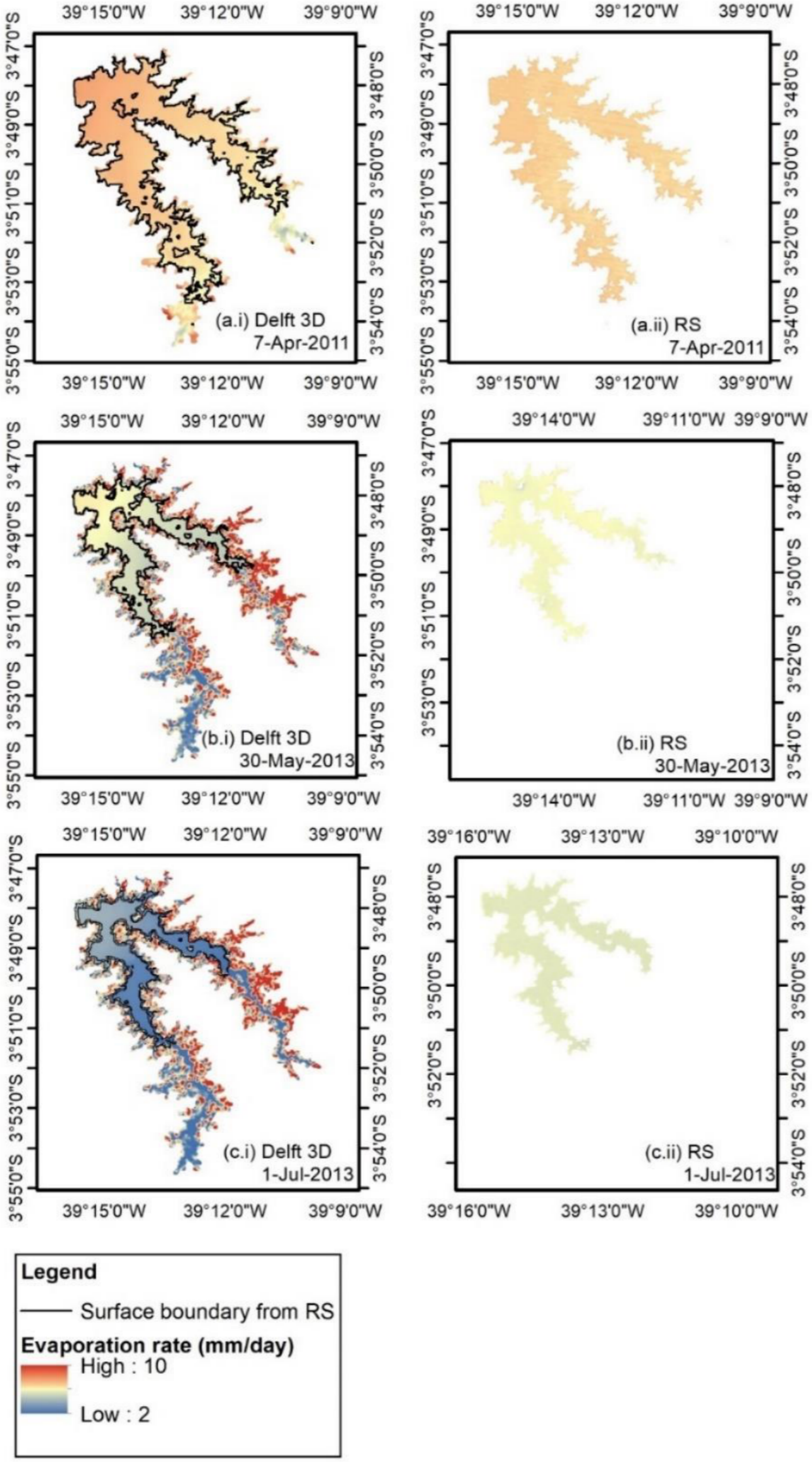

In the following, the hotter water in the inactive cells may not be transferred for the lacustrine region of the reservoir, retaining heat on the adjacent region of the lake. This process becomes more evident as the water level lowers, notably in Figure 30 (c), when the evaporation rates of the active water surface are remarkably lower than the ones estimated by RS. Interestingly, the averaged evaporation from both models is practically the same in all three days (see Figure 27). In contrast, the spatial distribution of evaporation is more similar only for 7-Apr-2011, notably a day with higher water level and therefore no retained heat in the borders. In agreement, the surface water temperature distribution on the active cells of the reservoir (see Figure 31) shows a cooling pattern among the observed days with no meteorological reason, even though no significant variability was noted in this period (see Figure 18).

Basically, the reservoir is losing heat for the inactive cells when the heat is not transferred to its downstream region, which affects all the thermal structure of the water body. As a consequence of that, the water column of the lake remains fully mixed even though the measurements indicate a small but existing temperature difference between surface and bottom (see Figure 31). This condition was not found until the end of the calibration, which indicates that, in order to prevent the retaining of heat in the modeling, a possible solution would be to use the threshold value as a calibration parameter. By doing this, heat would be transferred throughout the reservoir and the thermal processes better reproduced. An optimal value between numerical stability and calibration of thermal structure would be obtained. In the present study, the calibration of the water budget by adjusting the Dalton's coefficient led to a higher error on the thermal structure. This was noted because a cooling of the water column occurred with heat losses for the evaporation process. As the main objective was to reproduce evaporation patterns, the water budget prevailed with better calibration goodness of fit metrics.

Figure 31 - Surface temperature distribution modeled by Delft3D for (a) 7-Apr-2011, (b) 30-May-2013, and (c) 1-Jul-2013

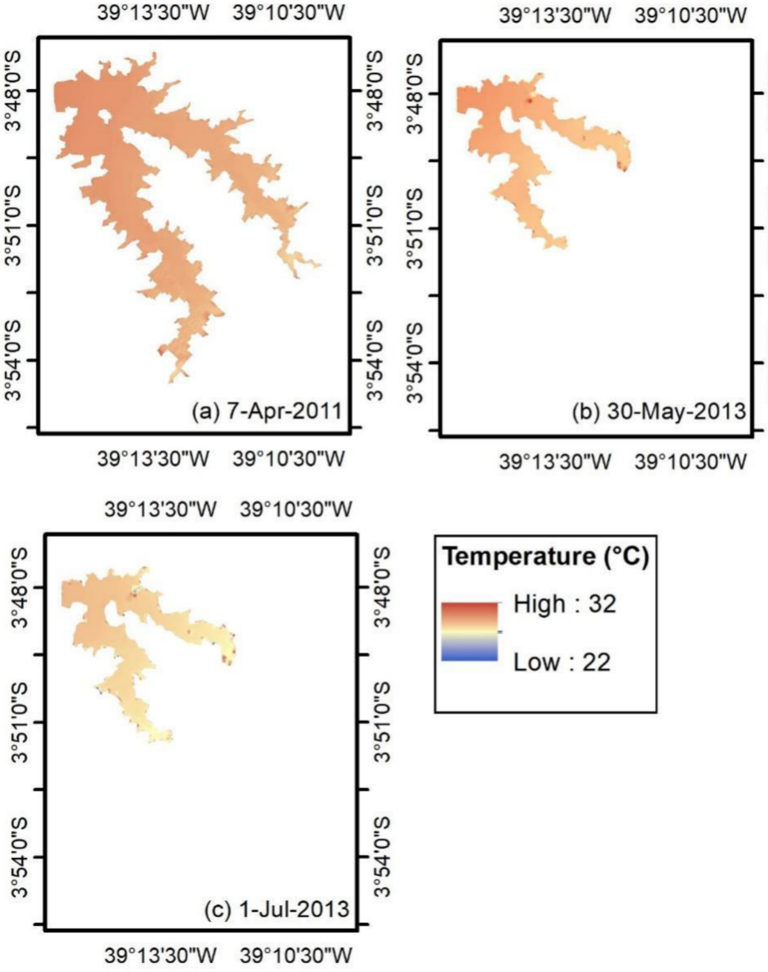

By analyzing the results from Delft3D and RS in Figure 30, similar evaporation surface distribution is noted for 7-Apr-2011, which is the day with the higher water level and in the month with the higher rainfall event among those observed (see Figure 28). Even though the surface pattern is generally the same, the results from Delt3D show only slightly higher losses than RS. Based on the fact that the RS depends on air and water temperatures, this may indicate that, for the wet season, the main driver for evaporation is water temperature. Regarding the other day of the analysis, Delft3d evaporation pattern differs from RS results on 7-Apr-2011 due to the retained heat in model's inactive cells.

The pattern observed in the RS evaporation rates shows higher stability for all the reservoir's surface in May and July (Figure 30), which can be associated to the absence of rain in that period of the year. This scenario favors the homogeneous evaporation of the water body, in agreement with Rodrigues *et al*. (2021b). However, Delft3D results indicate that the absence of rain not solely explains the surface distribution of the evaporation rates, even though it is a potential factor. Delft3D does not account for the effects of precipitation directly on the water body, hence changes in the evaporation pattern may be caused by the increased inflow on the wet season, in agreement with Elhakeem *et al.* (2015).

Additionally, Figure 30 shows higher evaporation rates at the boundaries of the reservoir considering the RS model, although no boundary pattern is present in the active cells of Delft3D results. In agreement to that, Ghahreman and Rahimzadegan (2022) also showed higher evaporation losses on the borders of two reservoirs in Iran, where wind speed, along with radiation, is a main driver for evaporation. However, Rodrigues *et al*. (2021a) found lower evaporation losses in the boundary of the studied reservoirs located in the Brazilian semiarid region, mainly due to influence of riparian vegetation. In fact, Pentecoste reservoir has no vegetation near the lake and a heating of the water column in the borders occur, generating higher evaporation rates in this region.

5.4 Thermal structure

In Figure 32 (a) the time series from PEA is observed, along with its correlation with water depth in the analyzed point and the PEA estimated from the measurements. Initially, it can be seen that the energy necessary for complete mixing the water column is high for the beginning of 2011, and it shows lower values in the dry period of that year. After that, a small rainfall event happens in 2012, when the PEA consistently increases. Continuing in the simulation period, 2013 is another year of drought, and here the rainfall is even lower than that of 2012 with barely no difference noted on PEA. In addition, the correlation coefficient between Delft3D results PEA and the water depth indicates that 33% of the variation in PEA is explained by its relationship with water depth. This result indicates that wet periods have a stable stratification of the water column, which may cause worse water quality.

Accordingly to that, Li *et al*. (2010) assessed the hydrodynamics of a lake located in the US and also found that water level drawdown is a main factor in thermal stratification and water movement during receding water levels. Also, Xing *et al*. (2018) discussed that higher and more uniform wind are related to mixing events. In fact, the thermal structure of a reservoir is a result of multiple driving forces, namely meteorological conditions and in-lake features.

In this context, in Figure 32 (b) a comparison between estimated PEA from Delft3D and from measurements for each calibration day is given. Here, it is notable that, for the first days, the model is sensible to the temperature differences and reproduces the thermal stability until the thermocline breakdown in October. After that, the thermal stability is reestablished, as described by PEA from measurements, but the model remains completely mixed. This enhances the previous discussions regarding the lack of heat in the middle of the reservoir, which is evidenced as the water level drops substantially.

Figure 32 - Comparison between PEA of the calibration cell from Delft3D and from measurements (a) for all the simulation period along with water depth, and (b) for calibration period

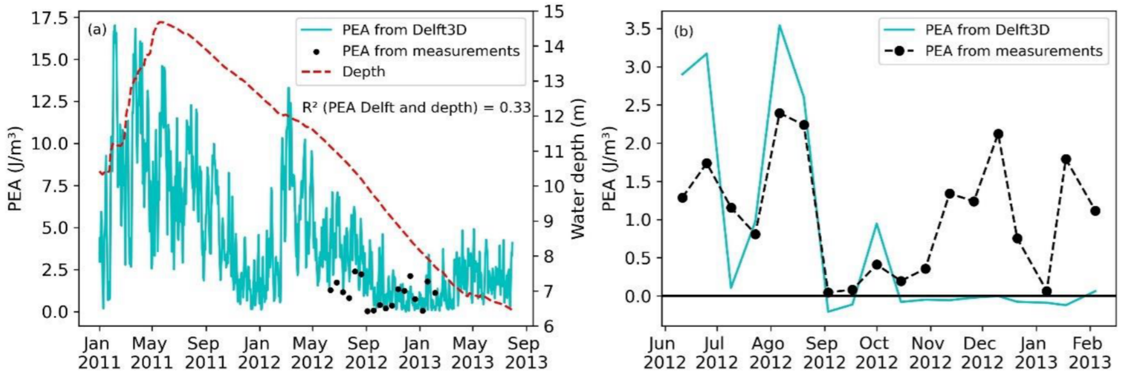

On this basis, inflow temperatures in the wet season tend to be lower than the water temperature of the reservoirs, which may induce an underflow in the lake. This condition develops a temperature gradient in the water column and contributes for a stratification state generated not by additional heating of the surface layer, but by a cooling of the deeper region. Following this logic, the stratification of Pentecoste reservoir showed higher stability in the wet season, as the inflows were not strong enough to generate turbulent mixing in the water column in addition to their lower temperatures. Figure 33 gives the longitudinal-vertical section location for branches (a) West and (b) East, while Figures 34 and 35 give the magnitude of water density, temperature, and velocity for typical periods, where the previous discussion is better observed. Additionally, in the Appendix this condition is given for days along all the simulation period, and it is more evident in the wet season of the drier years, i.e. 2012 and 2013.

Accordingly to that, Plec *et al*. (2020) found underflow conditions in a tropical reservoir, although the underflow occurred even for high flow state. Also, Curtarelli *et al*. (2014) found higher temperature differences in the river-reservoir transition zone, indicating river inflow as a contributor to the water column's stability. The relevance of this discussion is supported by Chung *et al*. (2014), that found increasing of cyanobacterial blooms during warmer and drought years, when a submerged flow followed by a surface layer deepening and stratification is noted.

Figure 33 - Location of longitudinal-vertical sections in (a) West and (b) East branches for hydrodynamic plot

Figure 34 - Magnitude of water density, temperature, and velocity in a typical day of March, 2012 for (a.i), (b.i), (c.i) West and (a.ii), (b.ii), (c.ii) East branches

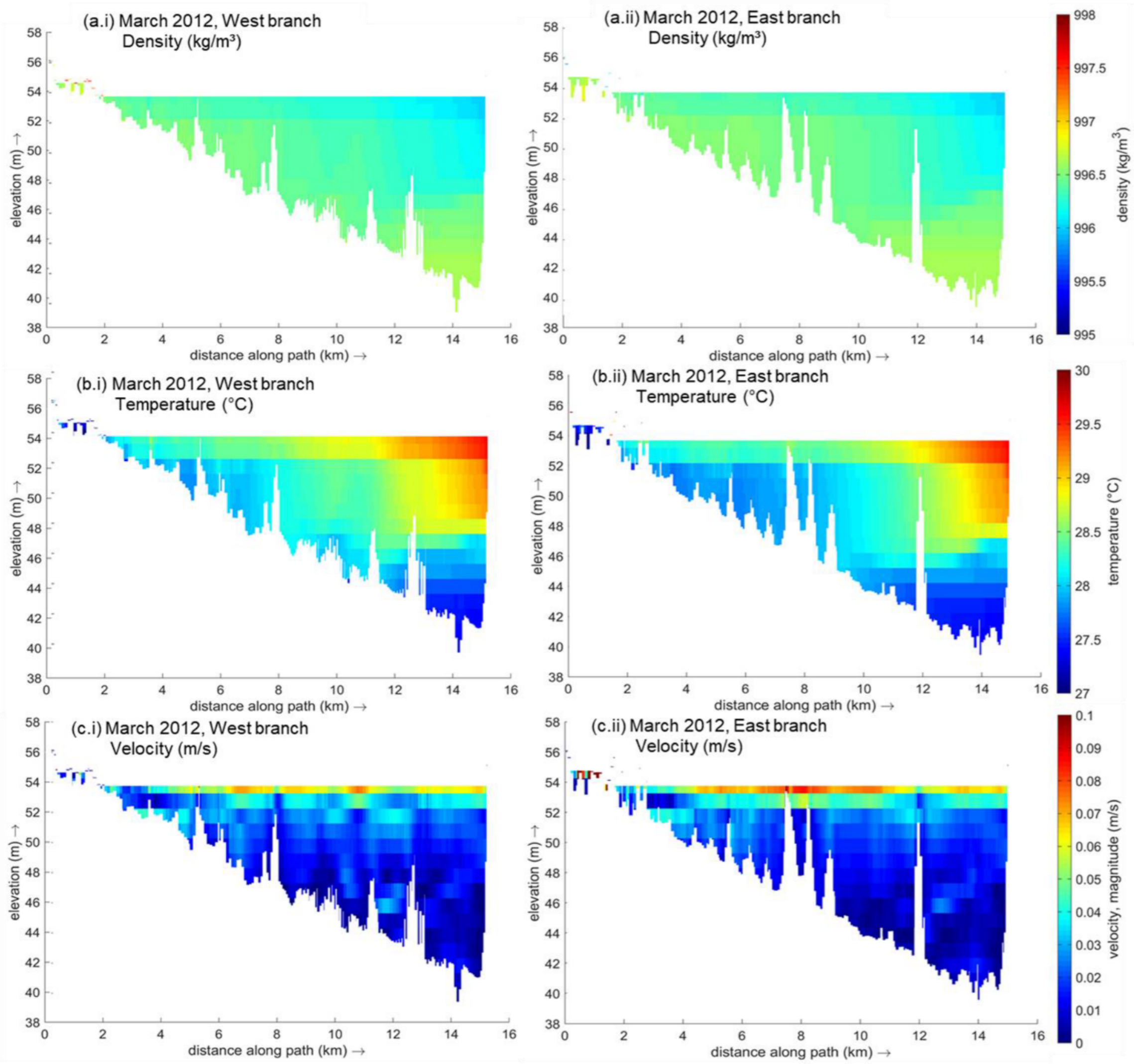

Figure 35 - Magnitude of water density, temperature, and velocity in a typical day of November, 2012 for (a.i), (b.i), (c.i) West and (a.ii), (b.ii), (c.ii) East branches

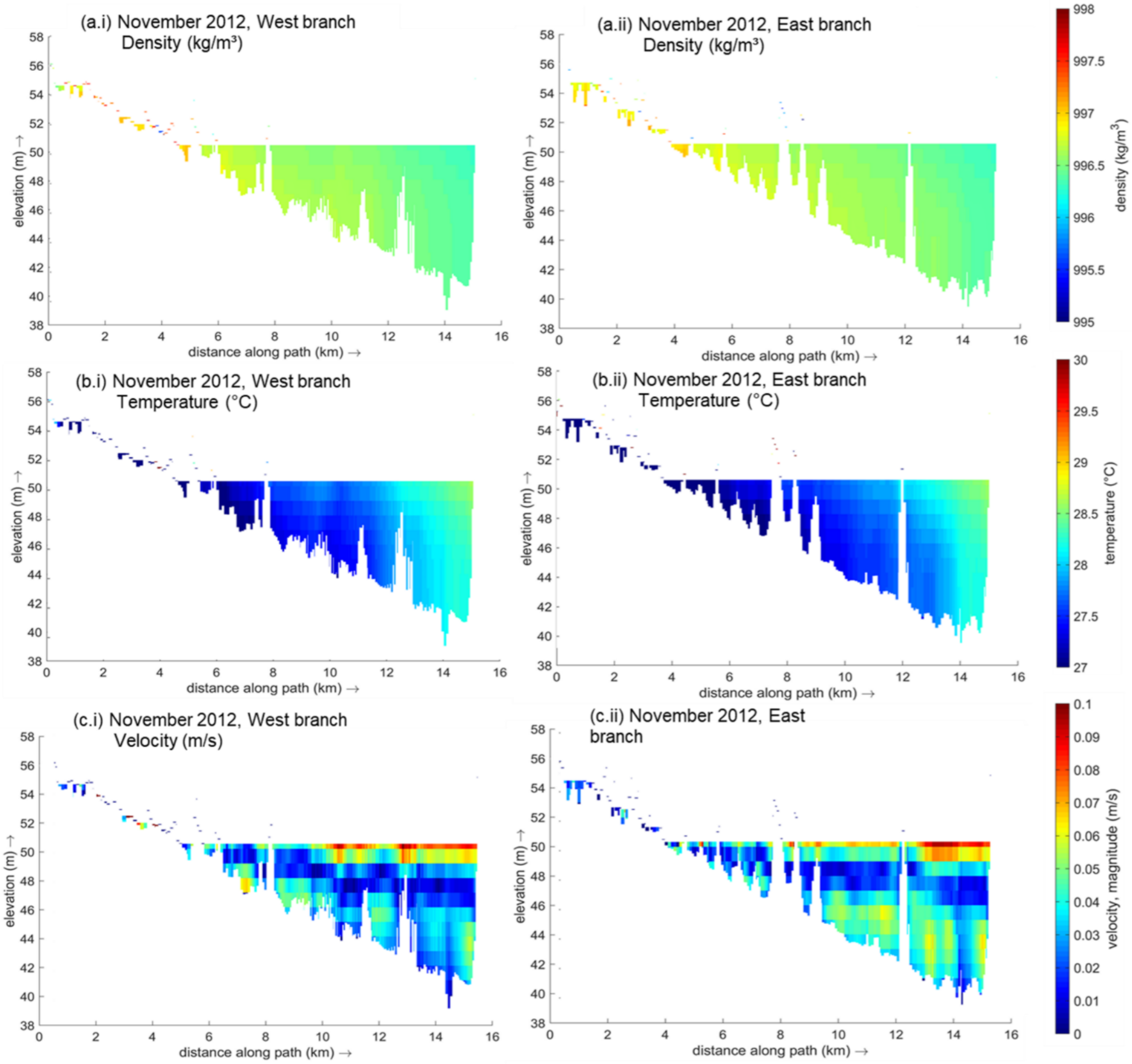

The maps of water density, temperature, and velocity for typical days through all the simulation period can be observed in the Appendix. It can be seen, in the velocity plots, a confined region with higher velocities in the surface layer for all the simulation period. The reservoir's surface shows wind driven currents, notably where the evaporation occurs. Also, a transfer of heat is noted in the surface on the temperature plots. Interestingly, in the wet season it seems that the reservoir remains vertically stratified, with a similar pattern on the horizontal axis. On the other hand, in the dry season a horizontal stratification is developed. A possible reason for this condition is the increase on the wind velocities for this period.

Figure 36 shows the correlation between monthly averaged evaporation rates and PEA for the calibration point of Pentecoste reservoir. It can be seen that the evaporation has an inverse relation with the stability of the water column. Initially this may seem contradictory, as evaporation rates are expected to be higher when the surface temperature increases, scenario that favors stratification events, but from previous discussions the stratification pattern of Pentecoste reservoir is most likely due to the inflow's lower temperatures than because of surface water heating. Even though this scenario is noted in the wet period, in the dry season there is the simultaneous occurrence of higher air temperatures, higher wind speeds, and barely no precipitation and therefore no inflow, which contributes to mixing of the water column along with higher evaporation rates. The previous statement along with the negative relation between evaporation and PEA noted in Figure 36 (b) indicates that the pattern of the wet season overcomes the one observed in the dry period, even though the low correlation coefficient might also point an alternating positive/negative correlation depending on the season.

Finally, it is important to highlight the innovative content of the proposed correlation. Evaporation rates are driven by multiple factors, and showing that 24% of its variability is explained solely by the relationship between the two data, i. e. evaporation rates and PEA, has a notable relevance. In fact, this discussion is supported by Mesquita *et al.*, (2020) results, as a damping in evaporation was noted with high nutrient concentration, and knowing stratification conditions are associated with low water quality, i.e. higher nutrient concentrations (see CHUNG *et al.*, 2014; SHILEI *et al.*, 2020; YANG *et al.*, 2018).

Figure 36 - Correlation between monthly averaged evaporation rates and PEA in (a) line and (b) scatter plots

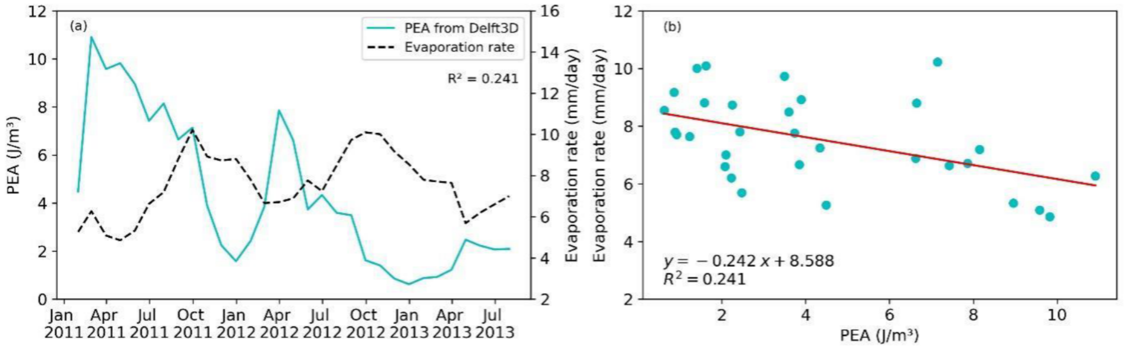

The study of a reservoir approaching both the spatial distribution and the vertical processes of the water column is a potential tool to optimize the location of techniques to reduce evaporation rates, namely air diffusers, floating structures, and floating solar panels, improving water availability and water resources management. In this context, Lima Neto (2019) found an increase on the regulated flow by inducing artificial destratification, that reduced the evaporation rates of a reservoir. Also, Shalaby et al. (2021) assessed the impact of floating covers in evaporation suppression considering water ecology, which could be achievable with the use of computational modeling. To conclude, Rodrigues et al. (2020) evaluates the potential use of floating photovoltaic plant in a tropical reservoir, finding that the damping on evaporation losses could supply around 50,000 people. The tool presented in this study along with a calibration made with more data could be an additional feature to those mentioned researches by bringing the best location to insert those innovative techniques.

5.5 Discussion of uncertainties

Uncertainty is defined as the lack of exact knowledge regardless the cause of it by Uusitalo *et al*. (2015). In fact, although the evaporation model demonstrated good accuracy with respect to the reference data, several sources of uncertainty may be present in this evaluation: i) distance from reference evaporation, ii) meteorological data - vapor pressure, air temperature, relative air humidity and wind speed, iii) interpolation of the meteorological data, iv) remote sensing data - surface temperature of water, as well as v) satellite limitations (TIMMERMANS *et al*., 2014).

Regarding the distance between the reservoirs and the measured evaporation and climatological data, how representative they can be? According to Blaney and Criddle (1950) and Schutgens *et al*. (2017), climatological data can have a large cover area, essentially in equatorial regions where they remain moderately constant.

Several studies estimate (by using hydrological models) and validate reservoir evaporation worldwide, however, only a few disposes of evaporation measures taken very close to the examined reservoir (PINTO, 2009) or even inside it (MASONER *et al*., 2008). In some researches, meteorological data and reference evaporation were measured at 1 km (YAO, 2009), 20 km (LOSGEDARAGH; RAHIMZADEGAN, 2018), or up to 65 km (ALI *et al*., 2008) from the study area; these examples convey how far away a weather station can still represent a region or, sometimes, is the unique manner to check the accuracy of the evaporation modeling.

Uncertainty can also be caused by reference data, such as Class A Pan evaporation. During autumn/winter when the stored heat is released, the reservoir can evaporate more than the Class A Tank, however, during spring/summer, when heat is stored in the reservoir, the evaporation rate derived from the reference data may be higher than the lake (FARNSWORTH *et al*., 1982).

Uncertainties involving the interpolation of the meteorological data in order to fulfill the days without measurements may also affect the final estimations of evaporation using Delft3D. Regan *et al.* (2002) divides uncertainty into six classes: inherent randomness, measurement error, systematic error, natural variation, model uncertainty, and subjective judgement. This brings the importance of fully understanding the limitations of the modeling tools, even the more complex ones as Delft3D. Deterministic models assume that a certain input will always lead to the same output, following a set of equations that theoretically represent the processes in nature. The more assumptions and simplification the model requires, the lower the level of prediction is expected, scenario that is reflected in the coefficient of correlation, as stated by Soares and Calijuri (2021).

When compared to physical and biological models, the hydrodynamics ones present lower complexity and therefore higher coefficient of determination (SOARES; CALIJURI, 2021). In fact, evaporation is strongly related to the reservoir hydrodynamic behavior, and the water temperature is a key aspect to correctly modeling it (DIJK; van VUUREN 2009, ELHAKEEM *et al.*, 2015).

Regarding the surface temperature of the water estimations some uncertainty may arise and have a negative impact in the evaporation estimation. When the satellite scene is captured, the models estimate the surface temperature, but this parameter is not constant throughout the day. Consequently, the daily temperature variability can result considerable changes in evaporation estimations by the Linacre (1977), as this parameter is one of the most sensitive for the model (as surface temperature is used to discover the air temperature in Linacre's model) (ABDELRADY *et al.*, 2016; LINACRE, 1977).

The different resolution of satellite images can also be another source of uncertainty: satellites with high spatial resolution of the thermal band usually have a lower temporal frequency (Landsat 8 – spatial resolution of the thermal band 100 m; temporal resolution 16 days), on the other hand, low spatial resolutions are associated with better temporal resolutions (MODIS - spatial resolution thermal band 1000 m; temporal resolution 1 to 2 days) (KALMA *et al.*, 2008). In addition, the Landsat 5 and 8 moderate spatial resolution can result in a mix of vegetation, water, and exposed soil, in heterogenous environment when using an algorithm to classify and identify objects.

Another limiting factor for remote sensing is the cloud cover. Constant coverage might make the application of methods unusual, as becomes impossible to capture the scenes. In the present study, for example, only 9% of the available images could be used to estimate evaporation because of high incidence of clouds. To overcome this issue, different remote sensing technologies can be used, as reported by Vinukollu *et al*. (2019), the authors estimated evapotranspiration in different regions of the world using a variety of satellites (AIRS, AVHRR, CERES, MODIS and NOAA). In three small reservoirs located in the Brazilian semiarid Coelho *et al*. (2017) used two satellites (Landsat 8 and RapidEye) to estimate Chlorophyll-a, trophic dynamics and the characterization of colored dissolved organic matter. The high-resolution (1 m or less) of Aircraft Light Detection and Ranging, CubeSats and Drones is more suitable for heterogeneous terrains covering and is being considered for the future to assess the impact in forests (land change), reservoirs, urban areas, etc. (JIAO *et al*., 2021).

In summary the uncertainties are inherent in both values, estimated and measured (reference data) ones. In relation to the measurements, the ideal would be the installation of Class A Tanks inside the reservoir under the study (MASONER *et al*., 2008), producing a more accurate evaporation. However, this methodology is more expensive, and requires a higher level of attention from the operator, when compared to the installation on the ground. Lowe *et al.* (2009) also listed detailed sources of uncertainty concerning evaporation estimations in reservoirs.

6 CONCLUSIONS

The main contribution of this study is the assessment of the hydro and thermodynamics of Pentecoste reservoir by calibrating a tridimensional model and evaluating the spatial distribution of evaporation patterns along with mixing conditions of the water column. Another important finding of this research is that the drying and flooding algorithm strategy is fundamental for applying adequately the evaporation model of Delft3D-FLOW. Following this, curves representing the correlation between evaporation rates and air temperature (r^2 of 0.736) and wind speed (r^2 of 0.853) were proposed, which are potential tools for the local water management company.

Additionally, an innovative evaluation was perfomed by comparing evaporation results obtained from 3D modeling and remote sensing, with an overall difference between the two models of less than 5%. Thus, when the spatial distribution of evaporation was evaluated, a retention of heat in the adjacent cells of the model was found associated to the threshold value adopted as a drying criteria. Therefore, the averaged evaporation rates were correctly reproduced by Delft3D. On the other hand, surface variability was underestimated for the dry period, when a strong reduction of the water level was observed.

As a consequence, reservoir cooling occurred, which was consistently reflected on the reservoir thermal structure, with a mixed condition being observed for the period with higher water level drawdown per unit time. In this context, when the PEA of the water column was analyzed, it showed a more stable stratification pattern for the wet season. This process indicated a potential occurrence of an underflow due to the lower inflow temperatures in the rainfall period, followed by the stratification of the water column not by heating of the water surface, but by cooling of its bottom layer. On this basis, the monthly averaged evaporation was found as negatively correlated with the stratification of the water column, even though the low coefficient of correlation might be an indicative of alternating positive/negative relation between evaporation and PEA depending on the season.

Finally, a discussion on the uncertainties involved in the study was made in order to highlight the simplifications inherent to modeling approaches. Those approximations are part of the limitations of the present research. As recommendations for future works, the calibration of the drying and flooding criteria is indicated, along with including inflow rate, temperature and evaporation measurements in field campaigns. In addition, it would be ideal to have multiple sampling points in the reservoir in order to make a spatialized calibration of thermal structure and evaporation.

This study brings an innovative approach which, with more data available for calibration, may be used to optimize the location for techniques that lower evaporation rates, such as air diffusers, shading structures, and floating solar panels. With the tridimensional model, the impacts of floating solar panels on the lake's evaporation and vertical processes may be assessed in order to understand the effects on both hydrodynamics and water quality. The proposed approaches represent potential tools in the process of enhancing water availability for the population and supporting decision making in water resources management.

REFERENCES

ABDELRADY, A., TIMMERMANS, J., VEKERDY, Z., SALAMA, M. “Surface energy balance of fresh and saline waters: AquaSEBS”, **Remote sensing**, 8(7), 583, 2016.

ALAZARD, M., LEDUC, C., TRAVI, Y., et al. "Estimating evaporation in semi-arid areas facing data scarcity: Example of the El Haouareb dam (Merguellil catchment, Central Tunisia)", **Journal of Hydrology: Regional Studies**, v. 3, p. 265–284, 2015. DOI: 10.1016/j.ejrh.2014.11.007. Disponível em: http://dx.doi.org/10.1016/j.ejrh.2014.11.007.

ALI, S., GHOSH, N. C., SINGH, R. "Evaluating best evaporation estimate model for water surface evaporation in semi-arid region, India", **Hydrological Processes**, v. 22, n. November 2008, p. 1093–1106, 2008. DOI: 10.1002/hyp.6664.

ALTHOFF, D., RODRIGUES, L. N., DA SILVA, D. D., et al. "Improving methods for estimating small reservoir evaporation in the Brazilian Savanna", **Agricultural Water Management**, v. 216, n. August 2018, p. 105–112, 2019. DOI: 10.1016/j.agwat.2019.01.028.

AMORIM, L. F., MARTINS, J. R. S., NOGUEIRA, F. F., et al. "Hydrodynamic and ecological 3D modeling in tropical lakes", **SN Applied Sciences**, v. 3, n. 4, p. 1–14, 2021. DOI: 10.1007/s42452-021-04272-6. Disponível em: https://doi.org/10.1007/s42452-021-04272-6.

AVDAN, U., JOVANOVSKA, G. “Algorithm for automated mapping of land surface temperature using LANDSAT 8 satellite data”, **Journal of Sensors**, 2016.

AZADI, F., ASHOFTEH, P. S., CHU, X. "Evaluation of the effects of climate change on thermal stratification of reservoirs", **Sustainable Cities and Society**, v. 66, p. 102531, 2021. DOI: 10.1016/j.scs.2020.102531. Disponível em: https://doi.org/10.1016/j.scs.2020.102531.

BARBOSA, C. C., CALIJURI, M. do C., DOS SANTOS, A. C. A., et al. "Future projections of water level and thermal regime changes of a multipurpose subtropical reservoir (Sao Paulo, Brazil)", **Science of the Total Environment**, v. 770, n. January, p. 144741, 2021. DOI: 10.1016/j.scitotenv.2020.144741. Disponível em: https://doi.org/10.1016/j.scitotenv.2020.144741.

BENZAGHTA, M. A., MOHAMMED, T. A., GHAZALI, A. H., et al. "Validation of Selected Models for Evaporation Estimation from Reservoirs Located in Arid and Semi-Arid Regions", **Arabian Journal for Science and Engineering**, v. 37, n. 3, p. 521–534, 2012. DOI: 10.1007/s13369-012-0194-5.

BIGLARBEIGI, P., GIULIANI, M., CASTELLETTI, A. "Partitioning the Impacts of Streamflow and Evaporation Uncertainty on the Operations of Multipurpose Reservoirs in Arid Regions", **Journal of Water Resources Planning and Management**, v. 144, n. 7, p. 05018008, 2018. DOI: 10.1061/(asce)wr.1943-5452.0000945.

BLANEY, H. F., CRIDDLE, W. D. “Determining water needs from climatological data”, **USDA Soil Conservation Service**. SOS–TP, USA, p. 8-9, 1950.

BRUCE, L. C., FRASSL, M. A., ARHONDITSIS, G. B., et al. "A multi-lake comparative analysis of the General Lake Model (GLM): Stress-testing across a global observatory network", **Environmental Modelling and Software**, v. 102, p. 274–291, 2018. DOI: 10.1016/j.envsoft.2017.11.016.

CAMPOS, J. N. B. "Paradigms and Public Policies on Drought in Northeast Brazil: A Historical Perspective", **Environmental Management**, v. 55, n. 5, p. 1052–1063, 2015. DOI: 10.1007/s00267-015-0444-x.

CAMPOS, JOSÉ N.B., LIMA NETO, IRAN E., STUDART, TICIANA M.C., NASCIMENTO, LUIZ S.V. “Trade-off between reservoir yield and evaporation losses as a function of lake morphology in semi-arid Brazil”, **Anais da Academia Brasileira de Ciências (online)**, v. 88, p. 1113-1126, 2016.

CHANUDET, V., FABRE, V., VAN DER KAAIJ, T. "Application of a three-dimensional hydrodynamic model to the Nam Theun 2 Reservoir (Lao PDR)", **Journal of Great Lakes Research**, v. 38, n. 2, p. 260–269, 2012. DOI: 10.1016/j.jglr.2012.01.008.

CHAPRA, Steven C. **Surface Water-Quality Modeling**. Waveland press, 1997. 844 p.

CHUNG, S. W., IMBERGER, J., HIPSEY, M. R., et al. "The influence of physical and physiological processes on the spatial heterogeneity of a Microcystis bloom in a stratified reservoir", **Ecological Modelling**, v. 289, p. 133–149, 2014. DOI: 10.1016/j.ecolmodel.2014.07.010. Disponível em: http://dx.doi.org/10.1016/j.ecolmodel.2014.07.010.

COELHO, C., HEIM, B., FOERSTER, S., BROSINSKY, A., de ARAÚJO, J. “In situ and satellite observation of CDOM and Chlorophyll-a dynamics in small water surface reservoirs in the Brazilian semiarid region”, **Water**, 9 (12), 913, 2017.

COSTA, A. C., ESTACIO, A. B. S., SOUZA FILHO, F. A., LIMA NETO, I. E. “Monthly and seasonal streamflow forecasting of large dryland catchments in Brazil”, **Journal of Arid Land**, v. 13, p. 205-223, 2021.

CURTARELLI, M. P., ALCÂNTARA, E., RENNÓ, C. D., et al. "Modelling the surface circulation and thermal structure of a tropical reservoir using three-dimensional hydrodynamic lake model and remote-sensing data", **Water and Environment Journal**, v. 28, n. 4, p. 516–525, 2014. DOI: 10.1111/wej.12066.

DE ARAÚJO, J. C., MAMEDE, G. L., DE LIMA, B. P. "Hydrological guidelines for reservoir operation to enhance water governance: Application to the Brazilian Semiarid region", **Water (Switzerland)**, v. 10, n. 11, 2018. DOI: 10.3390/w10111628.

DE ARAÚJO, J. C., PIEDRA, J. I. G. "Comparative hydrology: analysis of a semiarid and a humid tropical watershed", **Hydrological Processes**, v. 23, p. 1169–1178, 2009. DOI: 10.1002/hyp.

DE BOER, G. J., PIETRZAK, J. D., WINTERWERP, J. C. "Using the potential energy anomaly equation to investigate tidal straining and advection of stratification in a region of freshwater influence", **Ocean Modelling**, v. 22, n. 1–2, p. 1–11, 2008. DOI: 10.1016/j.ocemod.2007.12.003.

DELTARES (2020). User manual Delft3D-Flow. Technical report, Deltares, Delft, The Netherlands.

DINGJMAN, S. Lawrence. **Physical hydrology**. Waveland press, 2015. 643 p.

DISSANAYAKE, P., HOFMANN, H., PEETERS, F. "Comparison of results from two 3D hydrodynamic models with field data: internal seiches and horizontal currents", **Inland Waters**, v. 9, n. 2, p. 239–260, 2019. DOI: 10.1080/20442041.2019.1580079.

DO SACRAMENTO, E. M., CARVALHO, P. C. M., DE ARAÚJO, J. C., et al. "Scenarios for use of floating photovoltaic plants in Brazilian reservoirs", **IET Renewable Power Generation**, v. 9, n. 8, p. 1019–1024, 2015. DOI: 10.1049/iet-rpg.2015.0120.

DUGDALE, S. J., HANNAH, D. M., MALCOLM, I. A. “River temperature modelling: A review of process-based approaches and future directions”, **Earth-Science Reviews**, 175, 97-113, 2017.

EHSANI, N., VÖRÖSMARTY, C. J., FEKETE, B. M., et al. "Reservoir operations under climate change: Storage capacity options to mitigate risk", **Journal of Hydrology**, v. 555, p. 435–446, 2017. DOI: 10.1016/j.jhydrol.2017.09.008. Disponível em: https://doi.org/10.1016/j.jhydrol.2017.09.008.

ELHAKEEM, A., ELSHORBAGY, W., BLENINGER, T. "Long-term hydrodynamic modeling of the Arabian Gulf", **Marine Pollution Bulletin**, v. 94, n. 1–2, p. 19–36, 2015. DOI: 10.1016/j.marpolbul.2015.03.020. Disponível em: http://dx.doi.org/10.1016/j.marpolbul.2015.03.020.

FARNSWORTH, R. K., PECK, E. L., THOMPSON, E. S. (1982). **Evaporation atlas for the contiguous 48 United States**. US Department of Commerce, National Oceanic and Atmospheric Administration, National Weather Service.

FISCHER, H. B.; KOH, E. J. R. C. Y.; IMBERGER, J.; BROOKS, N. H. **Mixing in inland and coastal waters**. Academic press, Inc, 1979. 483 p.

FRIEDRICH, K., GROSSMAN, R. L., HUNTINGTON, J., et al. "Reservoir evaporation in the Western United States", **Bulletin of the American Meteorological Society**, v. 99, n. 1, p. 167–187, 2018. DOI: 10.1175/BAMS-D-15-00224.1.

GHAHREMAN, R., RAHIMZADEGAN, M. "Calculating net radiation of freshwater reservoir to estimate spatial distribution of evaporation using satellite images", **Journal of Hydrology**, v. 605, n. November 2021, p. 127392, 2022. DOI: 10.1016/j.jhydrol.2021.127392. Disponível em: https://doi.org/10.1016/j.jhydrol.2021.127392.

GOLYJESWSKI, O. W. **SIMULATION OF THERMAL STRATIFICATION USING THE A 2DV (CE-QUAL-W2) AND A 3D (DELFT3D) MODEL. THE CASE STUDY: PASSAÚNA RESERVOIR**. 2020. Universidade Federal do Paraná, 2020.

GUALTIERI, C., ANGELOUDIS, A., BOMBARDELLI, F., JHA, S., STOESSER, T. “On the Values for the Turbulent Schmidt Number in Environmental Flows”. Fluids, 2, 17. 2017. DOI:10.3390/fluids2020017.

HASTENRATH, S. "Exploring the climate problems of Brazil’s Nordeste: A review", **Climatic Change**, v. 112, n. 2, p. 243–251, 2012. DOI: 10.1007/s10584-011-0227-1.

HELFER, F., ANDUTTA, F. P., LOUZADA, J. A., et al. "Artificial destratification for reducing reservoir water evaporation: Is it effective?", **Lakes and Reservoirs: Research and Management**, v. 23, n. 4, p. 333–350, 2018. DOI: 10.1111/lre.12241.

HOFMEISTER, R., BURCHARD, H., BOLDING, K. "A three-dimensional model study on processes of stratification and de-stratification in the Limfjord", **Continental Shelf Research**, v. 29, n. 11–12, p. 1515–1524, 2009. DOI: 10.1016/j.csr.2009.04.004.

HOUNSOU-GBO, G. A., SERVAIN, J., ARAUJO, M., et al. "SST indexes in the tropical South Atlantic for forecasting rainy seasons in Northeast Brazil", **Atmosphere**, v. 10, n. 6, 2019. DOI: 10.3390/atmos10060335.

HUANG, L., FANG, H., FAZELI, M., et al. "Mobility of phosphorus induced by sediment resuspension in the Three Gorges Reservoir by flume experiment", **Chemosphere**, v. 134, p. 374–379, 2015b. DOI: 10.1016/j.chemosphere.2015.05.009. Disponível em:

http://dx.doi.org/10.1016/j.chemosphere.2015.05.009.

HUANG, L., FANG, H., REIBLE, D. "Mathematical model for interactions and transport of phosphorus and sediment in the Three Gorges Reservoir", **Water Research**, v. 85, p. 393–403, 2015a. DOI: 10.1016/j.watres.2015.08.049. Disponível em: http://dx.doi.org/10.1016/j.watres.2015.08.049.

IBGE (Instituto Brasileiro de Geografia e Estatística). **Produção da pecuária municipal**. Rio de Janeiro, 2020. Disponível em: < https://biblioteca.ibge.gov.br/index.php/biblioteca-catalogo?view=detalhes&id=784 >. Acesso em: 17 abr. 2022.

IMBERGER, J., HAMBLIN, P. F. "Dynamics of Lakes, Reservoirs, and Cooling Ponds.", **Annual Review of Fluid Mechanics**, v. 14, p. 153–187, 1982. DOI: 10.1146/annurev.fl.14.010182.001101.

ISHIKAWA, M., BLENINGER, T., LORKE, A. "Hydrodynamics and mixing mechanisms in a subtropical reservoir", **Inland Waters**, v. 0, n. 0, p. 1–16, 2021. DOI: 10.1080/20442041.2021.1932391. Disponível em: https://doi.org/10.1080/20442041.2021.1932391.

JI, Zhen-Gang. **Hydrodynamics and water quality**. John Wiley & Sons, Inc, 2008. 676 p.

JIAO, W., WANG, L., MCCABE, M. F. “Multi-sensor remote sensing for drought characterization: current status, opportunities and a roadmap for the future”. **Remote Sensing of Environment**, 256, 112313, 2021.

KALMA, J. D., MCVICAR, T. R., MCCABE, M. F. “Estimating land surface evaporation: A review of methods using remotely sensed surface temperature data”. **Surveys in Geophysics**, 29(4-5), 421-469, 2008.

KIRILLIN, G., SHATWELL, T. "Generalized scaling of seasonal thermal stratification in lakes", **Earth-Science Reviews**, v. 161, p. 179–190, 2016. DOI: 10.1016/j.earscirev.2016.08.008. Disponível em: http://dx.doi.org/10.1016/j.earscirev.2016.08.008.

KROL, M. S., DE VRIES, M. J., VAN OEL, P. R., et al. "Sustainability of Small Reservoirs and Large Scale Water Availability Under Current Conditions and Climate Change", **Water Resources Management**, v. 25, n. 12, p. 3017–3026, 2011. DOI: 10.1007/s11269-011-9787-0.

KUNDU, P. K.; COHEN, I. M.; DOWLING, D. R. **Fluid mechanics**. Elsevier Inc., 2016. 921 p.

LEE, R. M., BIGGS, T. W., FANG, X. "Thermal and hydrodynamic changes under a warmer climate in a variably stratified hypereutrophic reservoir", **Water (Switzerland)**, v. 10, n. 9, 2018. DOI: 10.3390/w10091284.

LI, Y., ACHARYA, K., CHEN, D., et al. "Modeling water ages and thermal structure of Lake Mead under changing water levels", **Lake and Reservoir Management**, v. 26, n. 4, p. 258–272, 2010. DOI: 10.1080/07438141.2010.541326.

LIMA NETO, I. E. "Impact of artificial destratification on water availability of reservoirs in the Brazilian semiarid", **Anais da Academia Brasileira de Ciencias**, v. 91, n. 3, p. 1–12, 2019. DOI: 10.1590/0001-3765201920171022.

LIMA NETO, I. E, MEDEIROS, P. H. A., COSTA, A. C., WIEGAND, M. C., BARROS, A. R. M., BARROS, M. U. G. “Assessment of phosphorus loading dynamics in a tropical reservoir with high seasonal water level changes”. **Science of the Total Environment**, v. 815, p. 152875, 2022.

LINACRE, E. T. “A simple formula for estimating evaporation rates in various climates, using temperature data alone”. **Agricultural meteorology**, 18(6), 409-424, 1977.

LIN, B., SHIONO, K. “Numerical modelling of solute transport in compound channel flows”. **Journal of Hydraulic Research**, v. 33, n. 6, 773-788, 1995.

LOSGEDARAGH, S. Z., RAHIMZADEGAN, M. “Evaluation of SEBS, SEBAL, and METRIC models in estimation of the evaporation from the freshwater lakes (Case study: Amirkabir dam, Iran)”, Journal of Hydrology, 561, 523-531, 2018.

LOWE, L. D., WEBB, J. A., NATHAN, R. J., et al. "Evaporation from water supply reservoirs: An assessment of uncertainty", **Journal of Hydrology**, v. 376, n. 1–2, p. 261–274, 2009. DOI: 10.1016/j.jhydrol.2009.07.037.

LOWE, L. D., WEBB, J. A., NATHAN, R. J., ETCHELLS, T., and MALANO, H. M. “Evaporation from water supply reservoirs: An assessment of uncertainty”, **Journal of Hydrology**, 376(1-2), 261-274, 2009.

MADY, B., LEHMANN, P., OR, D. "Evaporation Suppression from Small Reservoirs Using Floating Covers—Field Study and Modeling", **Water Resources Research**, v. 57, n. 4, p. 1–16, 2021. DOI: 10.1029/2020WR028753.

MALARET, E.; BARTOLUCCI, L.A; LOZANO, D.F.; ANUTA, P.E.; MCGILLEM, C.D. “Landsat-4 and Landsat-5 Thematic Mapper data quality analysis”, **Photogrammetric Engineering and Remote Sensing**, v. 51, n. 9, p. 1407-1416, 1985.

MAMEDE, G. L., ARAÚJO, N. A. M., SCHNEIDER, C. M., et al. "Overspill avalanching in a dense reservoir network", **Proceedings of the National Academy of Sciences of the United States of America**, v. 109, n. 19, p. 7191–7195, 2012. DOI: 10.1073/pnas.1200398109.

MAN, X., LEI, C., CAREY, C. C., et al. "Relative performance of 1-D versus 3-D hydrodynamic, water-quality models for predicting water temperature and oxygen in a shallow, eutrophic, managed reservoir", **Water (Switzerland)**, v. 13, n. 1, 2021. DOI: 10.3390/w13010088.

MASONER, J. R., STANNARD, D. I., CHRISTENSON, S. C. “Differences in Evaporation Between a Floating Pan and Class A Pan on Land 1”, **JAWRA Journal of the American Water Resources Association**, 44(3), 552-561, 2008.

DE FRANÇA, M. B., J., CAPELO NETO, J., LIMA NETO, I. E., et al. "Simulação da compartimentação em reservatório no semiárido brasileiro – uso da modelagem hidrodinâmica como ferramenta de gestão", **Revista DAE**, v. 69, n. 231, p. 41–53, 2021. DOI: 10.36659/dae.2021.045.

MESQUITA, J. B. de F., LIMA NETO, I. E., RAABE, A., et al. "The influence of hydroclimatic conditions and water quality on evaporation rates of a tropical lake", **Journal of Hydrology**, v. 590, n. June, p. 125456, 2020. DOI: 10.1016/j.jhydrol.2020.125456. Disponível em: https://doi.org/10.1016/j.jhydrol.2020.125456.

MOLINAS, E., CARNEIRO, J. C., VINZON, S. "Internal tides as a major process in Amazon continental shelf fine sediment transport", **Marine Geology**, v. 430, p. 106360, 2020. DOI: 10.1016/j.margeo.2020.106360. Disponível em: https://doi.org/10.1016/j.margeo.2020.106360.

MORIASI, D. N., GITAU M. W., DAGGUPATI, P. “Hydrologic and water quality models: performance measures and evaluation criteria”, **American Society of Agricultural and Biological Engineers**. 58(6):1763-1785, 2015.

NAKHAEI, N., BOEGMAN, L., MEHDIZADEH, M., et al. "Hydrodynamic modeling of Edmonton storm-water ponds", **Environmental Fluid Mechanics**, v. 19, n. 2, p. 305–327, 2019. DOI: 10.1007/s10652-018-9625-5. Disponível em: https://doi.org/10.1007/s10652-018-9625-5.

NIÑO, Y., TAMBURRINO, A. (2004). Heat balance in lakes and reservoirs. https://www.u-cursos.cl/ingenieria/2005/1/CI71Q/1/material_docente/bajar?id_material=29468. Access Date: 12/01/2021.

OUNI, H., SOUSA, M. C., RIBEIRO, A. S., et al. "Numerical modeling of hydrodynamic circulation in Ichkeul Lake-Tunisia", **Energy Reports**, v. 6, p. 208–213, 2020. DOI: 10.1016/j.egyr.2019.08.044. Disponível em: https://doi.org/10.1016/j.egyr.2019.08.044.

PALMAN, L. E., TRENTO, A. E., ALVAREZ, A. M. "Scalar Dispersion in the Salado River Through Tracers Test and Two-Dimensional Model", **Water**, Air, and Soil Pollution, v. 232, n. 12, 2021. DOI: 10.1007/s11270-021-05436-1.

PEREZ, M., PEREZ, R., FERGUSON, C. R., et al. "Deploying effectively dispatchable PV on reservoirs: Comparing floating PV to other renewable technologies", **Solar Energy**, v. 174, n. April, p. 837–847, 2018. DOI: 10.1016/j.solener.2018.08.088. Disponível em: https://doi.org/10.1016/j.solener.2018.08.088.

PICCIONI, F., CASENAVE, C., LEMAIRE, B. J., et al. "The thermal response of small and shallow lakes to climate change: New insights from 3D hindcast modelling", **Earth System Dynamics**, v. 12, n. 2, p. 439–456, 2021. DOI: 10.5194/esd-12-439-2021.

PINTO, F. A. **Medição da evaporação em tanques classe a instalados em ambientes aquático e terrestre**. 2009. Mater’s Dissertation. Universidade Federal do Ceará.

PLEC, D. F., DAS GRAÇAS SILVA, T. F., VINÇON-LEITE, B., et al. "Thermal functioning of a tropical reservoir assessed through three-dimensional modelling and high-frequency monitoring", **Revista Brasileira de Recursos Hidricos**, v. 26, 2021. DOI: 10.1590/2318-0331.262120200150.

POLLI, B. A., BLENINGER, T. "Comparison of 1D and 3D reservoir heat transport models and temperature effects on mass transport", **Revista Brasileira de Recursos Hidricos**, v. 24, 2019. DOI: 10.1590/2318-0331.241920190023.

PONTES FILHO, J. D., SOUZA FILHO, F. A., MARTINS, E. S. P. R., et al. "Copula-Based Multivariate Frequency Analysis of the", **Water**, v. 12, n. 834, p. 1–22, 2020.

RABELO, U. P., DIETRICH, J., COSTA, A. C., SIMSHAUSER, M. N., SCHOLZ, F. E., NGUYEN, T. V., LIMA NETO, I. E. “Representing a dense network of ponds and reservoirs in a semi-distributed dryland catchment model”, **Journal of Hydrology**, v. 127103, p. 127103, 2021.

RAULINO, J. B. S., SILVEIRA, C. S., LIMA NETO, I. E. "Assessment of climate change impacts on hydrology and water quality of large semi-arid reservoirs in Brazil", **Hydrological Sciences Journal**, v. 66, n. 8, p. 1321–1336, 2021. DOI: 10.1080/02626667.2021.1933491. Disponível em: https://doi.org/10.1080/02626667.2021.1933491.

REGAN, H. M., COLYVAN, M., BURGMAN, M. A. "A taxonomy and treatment of uncertainty for ecology and conservation biology", **Ecological Applications**, v. 12, n. 2, p. 618–628, 2002. DOI: 10.1890/1051-0761(2002)012[0618:ATATOU]2.0.CO;2.

REY, A., MULLIGAN, R., DA SILVA, A. M. F., et al. "Three-Dimensional Hydrodynamic Behavior of an Operational Waste-Stabilization Pond", **Journal of Environmental Engineering**, v. 147, n. 2, p. 05020009, 2021. DOI: 10.1061/(asce)ee.1943-7870.0001834.

ROCHA, M. J. D., LIMA NETO, I. E. "Modeling flow-related phosphorus inputs to tropical semiarid reservoirs", **Journal of Environmental Management**, v. 295, 113123, 2021.

ROCHA, M. J. D., LIMA NETO, I. E. "Phosphorus mass balance and input load estimation from the wet and dry periods in tropical semiarid reservoirs", **Environmental Science and Pollution Research**, v. 29, 10027-10046, 2022a.

ROCHA, M. J. D., LIMA NETO, I. E. "Internal phosphorus loading and its driving factors in the dry period of Brazilian semiarid reservoirs", **Journal of Environmental Management**, v. 312, 114983, 2022b.

ROCHA, S. M. G., MESQUITA, J. B. F., LIMA NETO, I. E. "Modelagem hidrodinâmica e avaliação do decaimento do fósforo em um lago urbano hipereutrófico", Revista AIDIS de Ingeniería y Ciencias Ambientales: Investigación, Desarrollo y práctica, v. 13, n. 2, 530-545, 2020.

ROCHA, S. M. G. **Impacto da variabilidade hidroclimática na hidrodinâmica de um reservatório urbano em Fortaleza/CE**. 2019. Trabalho de Conclusão de Curso. Universidade Federal do Ceará.

RODRIGUES, I. S., COSTA, C. A. G., LIMA NETO, I. E., et al. "Trends of evaporation in Brazilian tropical reservoirs using remote sensing", **Journal of Hydrology**, v. 598, n. November 2020, [S.d.]. DOI: 10.1016/j.jhydrol.2021.126473.

RODRIGUES, I. S., COSTA, C. A. G., RAABE, A., et al. "Evaporation in Brazilian dryland reservoirs: Spatial variability and impact of riparian vegetation", **Science of the Total Environment**, v. 797, p. 149059, [S.d.]. DOI: 10.1016/j.scitotenv.2021.149059. Disponível em: https://doi.org/10.1016/j.scitotenv.2021.149059.

RODRIGUES, I. S., RAMALHO, G. L. B., MEDEIROS, P. H. A. "Potential of floating photovoltaic plant in a tropical reservoir in Brazil", **Journal of Environmental Planning and Management**, v. 63, n. 13, p. 2334–2356, 2020. DOI: 10.1080/09640568.2020.1719824. Disponível em: https://doi.org/10.1080/09640568.2020.1719824.

SCHUTGENS, N. J., TSYRO, S., GRYSPEERDT, E., GOTO, D., WEIGUM, N., SCHULZ, M., STIER, P. "On the spatio-temporal representativeness of observations", **Atmospheric Chemistry and Physics Discussions**, v. 17, 9761-9780, 2017.

SHALABY, M. M., NASSAR, I. N., ABDALLAH, A. M. "Evaporation suppression from open water surface using various floating covers with consideration of water ecology", **Journal of Hydrology**, v. 598, n. October 2020, p. 126482, 2021. DOI: 10.1016/j.jhydrol.2021.126482. Disponível em: https://doi.org/10.1016/j.jhydrol.2021.126482.

SHARAF, N., LEMAIRE, B. J., FADEL, A., et al. "Assessing the thermal regime of poorly monitored reservoirs with a combined satellite and three-dimensional modeling approach", **Inland Waters**, v. 11, n. 3, p. 302–314, 2021. DOI: 10.1080/20442041.2021.1913937. Disponível em: https://doi.org/10.1080/20442041.2021.1913937.

SHILEI, Z., YUE, S., TINGLIN, H., et al. "Reservoir water stratification and mixing affects microbial community structure and functional community composition in a stratified drinking reservoir", **Journal of Environmental Management**, v. 267, n. April, p. 110456, 2020. DOI: 10.1016/j.jenvman.2020.110456. Disponível em: https://doi.org/10.1016/j.jenvman.2020.110456.

SIMPSON, J. H., HUGHES, D. G., MORRIS, N. C. G. "The relation of seasonal stratification to tidal mixing on the continental shelf", **A Voyage of Discovery George Deacon 70th anniversary volume**, n. September 1980, p. 327–340, 1977.

SIRH/Ce. 2020. “Electronic Atlas of Water Resources of Ceará (Atlas Eletrônico dos Recursos Hídricos do Ceará).” http://atlas.srh.ce.gov.br/

SNIS (Sistema Nacional de Informações sobre Saneamento). **Painel de Saneamento**. Brasil, 2020. Disponível em: < http://appsnis.mdr.gov.br/indicadores/web/agua_esgoto/mapa-esgoto/?cod=2302800 >. Acesso em: 17 abr. 2022.

SOARES, L. M. V., CALIJURI, M. do C. "Deterministic modelling of freshwater lakes and reservoirs: Current trends and recent progress", **Environmental Modelling and Software**, v. 144, n. July, p. 105143, 2021. DOI: 10.1016/j.envsoft.2021.105143. Disponível em: https://doi.org/10.1016/j.envsoft.2021.105143.

SOARES, L. M. V., SILVA, T. F. das G., VINÇON-LEITE, B., et al. "Modelling drought impacts on the hydrodynamics of a tropical water supply reservoir", **Inland Waters**, v. 9, n. 4, p. 422–437, 2 out. 2019. DOI: 10.1080/20442041.2019.1596015.

TANNY, J., COHEN, S., ASSOULINE, S., et al. "Evaporation from a small water reservoir: Direct measurements and estimates", **Journal of Hydrology**, v. 351, n. 1–2, p. 218–229, 2008. DOI: 10.1016/j.jhydrol.2007.12.012.

TIMMERMANS, J., SU, Z., VAN DER TOL, C., VERHOEF, A., VERHOEF, W. “Quantifying the uncertainty in estimates of surface-atmosphere fluxes through joint evaluation of the SEBS and SCOPE models”, **Hydrology and Earth System Sciences**, 17(4), 2013.

TOMINAGA, Y., STATHOPOULOS, T. “Turbulent Schmidt numbers for CFD analysis with various types of flowfield”, **Atmospheric Environment**, 41, 8091-8099, 2007. DOI: 10.1016/j.atmosenv.2007.06.054.

UUSITALO, L., LEHIKOINEN, A., HELLE, I., et al. "An overview of methods to evaluate uncertainty of deterministic models in decision support", **Environmental Modelling and Software**, v. 63, p. 24–31, 2015. DOI: 10.1016/j.envsoft.2014.09.017. Disponível em: http://dx.doi.org/10.1016/j.envsoft.2014.09.017.

VALDESPINO-CASTILLO, P. M., MERINO-IBARRA, M., JIMÉNEZ-CONTRERAS, J., et al. "Community metabolism in a deep (stratified) tropical reservoir during a period of high water-level fluctuations", **Environmental Monitoring and Assessment**, v. 186, n. 10, p. 6505–6520, 2014. DOI: 10.1007/s10661-014-3870-y.

VAN DIJK, M., VAN VUUREN, S. J. "Destratifcation induced by bubble plumes as a means to reduce evaporation from open impoundments", **Water SA**, v. 35, n. 2, p. 158–167, 2009. DOI: 10.4314/wsa.v35i2.76731.

VINÇON-LEITE, B., CASENAVE, C. "Modelling eutrophication in lake ecosystems: A review", **Science of the Total Environment**, v. 651, p. 2985–3001, 2019. DOI: 10.1016/j.scitotenv.2018.09.320. Disponível em: https://doi.org/10.1016/j.scitotenv.2018.09.320.

VINUKOLLU, R. K., WOOD, E. F., FERGUSON, C. R., FISHER, J. B. “Global estimates of evapotranspiration for climate studies using multi-sensor remote sensing data: Evaluation of three process-based approaches”, **Remote Sensing of Environment**, 115(3), 801-823, 2011.

WANG, L., YU, Z., DAI, H., et al. "Eutrophication model for river-type reservoir tributaries and its applications", **Water Science and Engineering**, v. 2, n. 1, p. 16–24, 2009. DOI: 10.3882/j.issn.1674-2370.2009.01.002. Disponível em: http://dx.doi.org/10.3882/j.issn.1674-2370.2009.01.002.

WANG, W., XIAO, W., CAO, C., et al. "Temporal and spatial variations in radiation and energy balance across a large freshwater lake in China", **Journal of Hydrology**, v. 511, p. 811–824, 2014. DOI: 10.1016/j.jhydrol.2014.02.012. Disponível em: http://dx.doi.org/10.1016/j.jhydrol.2014.02.012.

WIEGAND, M. C., DO NASCIMENTO, A. T. P., COSTA, A. C., LIMA NETO, I. E. “Trophic state changes of semi-arid reservoirs as a function of the hydro-climatic variability”, **Journal of Arid Environment**, v. 184, p. 104321, 2021.

XING, Z., CHUA, L. H. C., MIAO, H., et al. "Wind Shielding Impacts on Water Quality in an Urban Reservoir", **Water Resources Management**, v. 32, n. 11, p. 3549–3561, 2018. DOI: 10.1007/s11269-018-1980-y.

XU, Z. H., WU, S. H., LIU, M. C., et al. "Effects of water discharge on river-dominated delta growth", **Petroleum Science**, v. 18, n. 6, p. 1630–1649, 2021. DOI: 10.1016/j.petsci.2021.09.027. Disponível em: https://doi.org/10.1016/j.petsci.2021.09.027.

YANG, Z., XU, P., LIU, D., et al. "Hydrodynamic mechanisms underlying periodic algal blooms in the tributary bay of a subtropical reservoir", **Ecological Engineering**, v. 120, n. 28, p. 6–13, 2018. DOI: 10.1016/j.ecoleng.2018.05.003. Disponível em: https://doi.org/10.1016/j.ecoleng.2018.05.003.

YAO, H. X. “Long-term study of lake evaporation and evaluation of seven estimation methods: results from Dickie Lake, South-Central Ontario, Canada”, **Journal of Environmental Protection**, 1(01), 1, 2009.

ZHANG, F., ZHANG, H., BERTONE, E., et al. "Numerical study of the thermal structure of a stratified temperate monomictic drinking water reservoir", **Journal of Hydrology: Regional Studies**, v. 30, n. May, p. 100699, 2020. DOI: 10.1016/j.ejrh.2020.100699. Disponível em: https://doi.org/10.1016/j.ejrh.2020.100699.

ZHANG, H., GORELICK, S. M., ZIMBA, P. V., et al. "A remote sensing method for estimating regional reservoir area and evaporative loss", **Journal of Hydrology**, v. 555, p. 213–227, 2017. DOI: 10.1016/j.jhydrol.2017.10.007. Disponível em: https://doi.org/10.1016/j.jhydrol.2017.10.007.

ZHAO, G., GAO, H. "Estimating reservoir evaporation losses for the United States: Fusing remote sensing and modeling approaches", **Remote Sensing of Environment**, v. 226, n. March, p. 109–124, 2019. DOI: 10.1016/j.rse.2019.03.015. Disponível em: https://doi.org/10.1016/j.rse.2019.03.015.

ZHAO, Q., REN, Y., WANG, J. X. L. "Temporal and spatial characteristics of potential energy anomaly in Lake Taihu", **Environmental Science and Pollution Research**, v. 25, n. 24, p. 24316–24325, 2018. DOI: 10.1007/s11356-018-2204-y.

ZIAIE, R., MOHAMMADNEZHAD, B., TAHERIYOUN, M., et al. "Evaluation of Thermal Stratification and Eutrophication in Zayandeh Roud Dam Reservoir Using Two-Dimensional

CE-QUAL-W2 Model", **Journal of Environmental Engineering**, v. 145, n. 6, p. 05019001, 2019. DOI: 10.1061/(asce)ee.1943-7870.0001529.

APPENDIX A – ADDITIONAL DELFT 3D MAP RESULTS

Figure A. 1 - Magnitude of water density, temperature, and velocity in a typical day of March, 2011 for (a.i), (b.i), (c.i) West and (a.ii), (b.ii), (c.ii) East branches

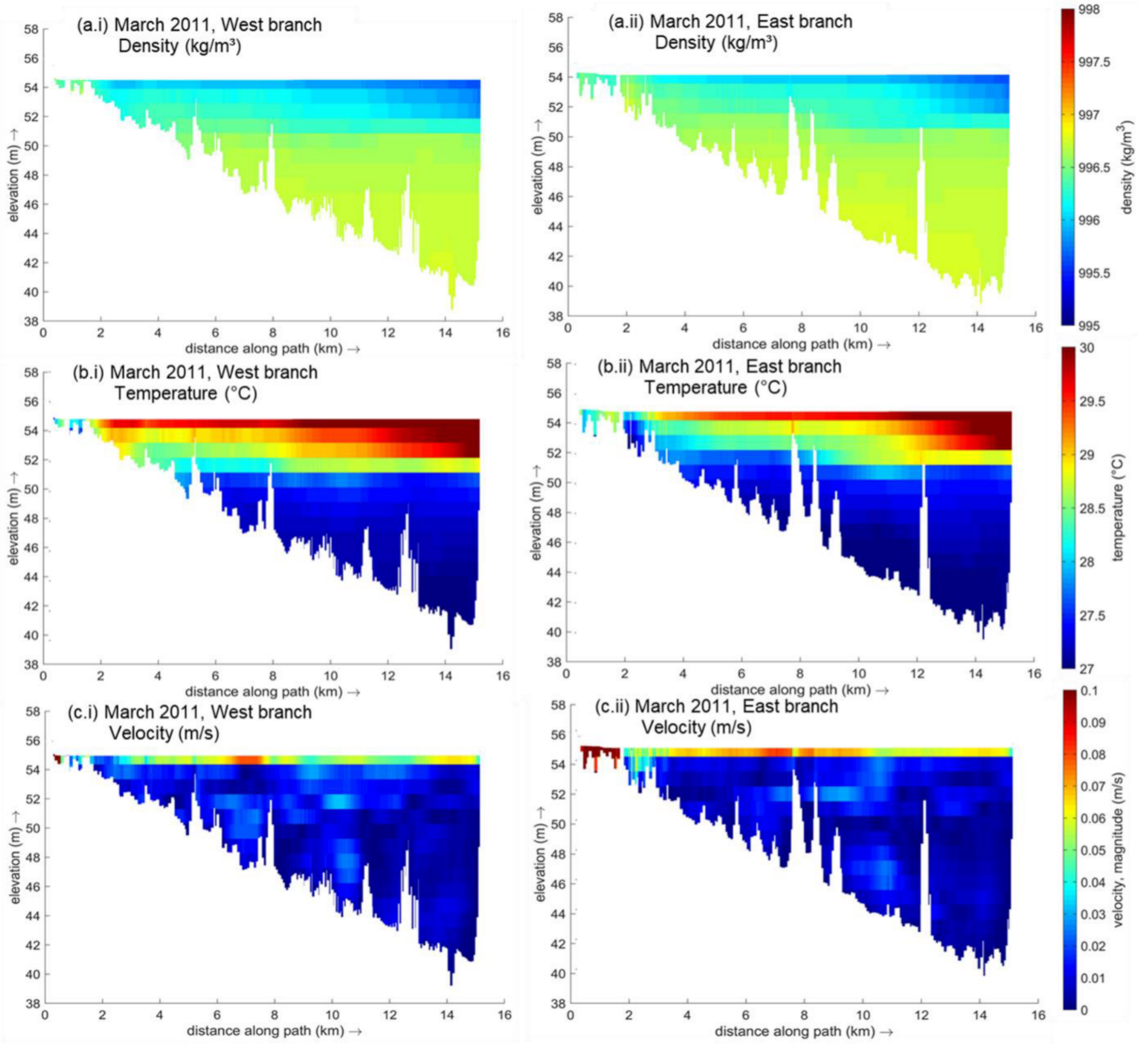

Figure A. 2 - Magnitude of water density, temperature, and velocity in a typical day of July, 2011 for (a.i), (b.i), (c.i) West and (a.ii), (b.ii), (c.ii) East branches

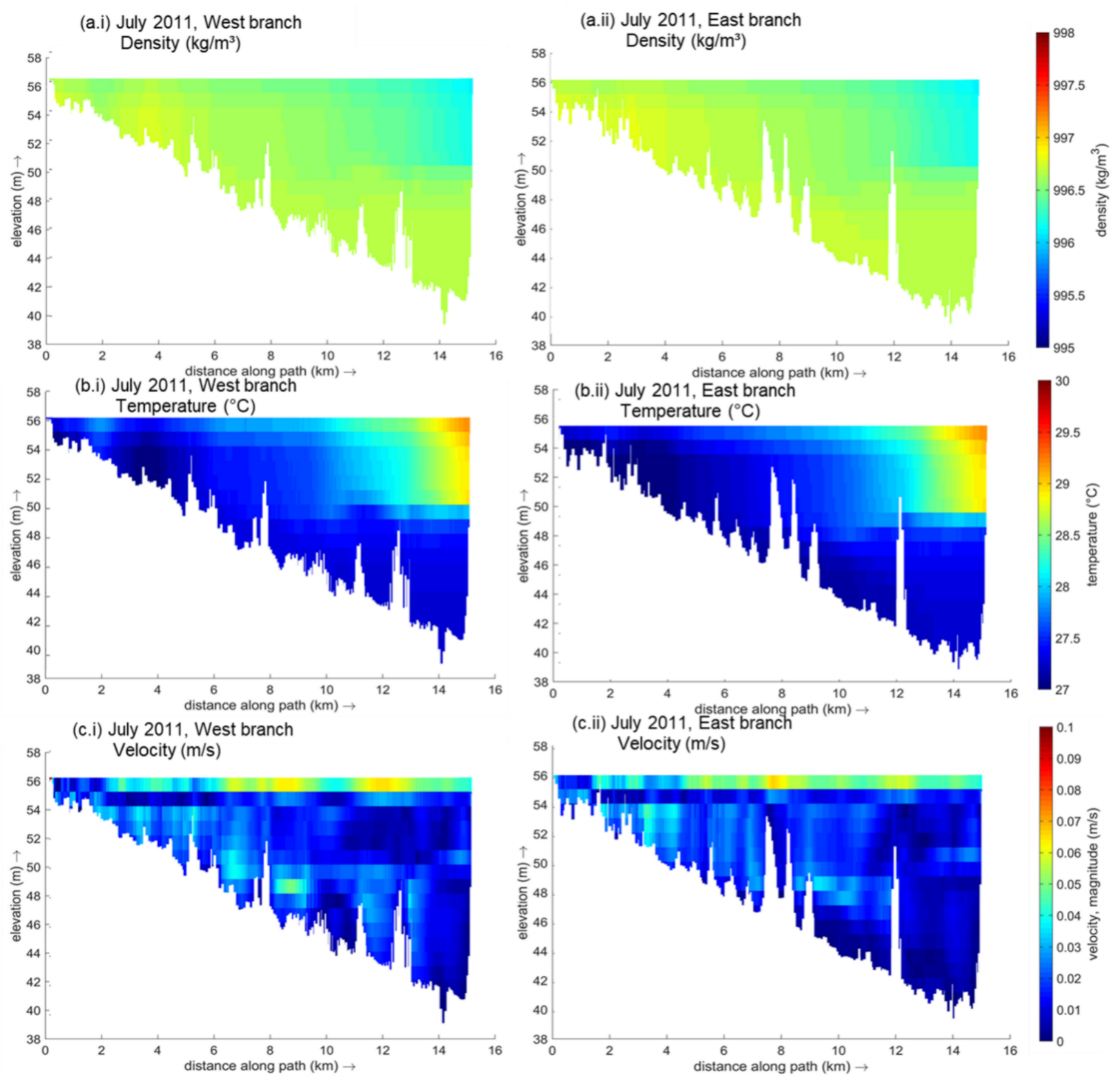

Figure A. 3 - Magnitude of water density, temperature, and velocity in a typical day of November, 2011 for (a.i), (b.i), (c.i) West and (a.ii), (b.ii), (c.ii) East branches

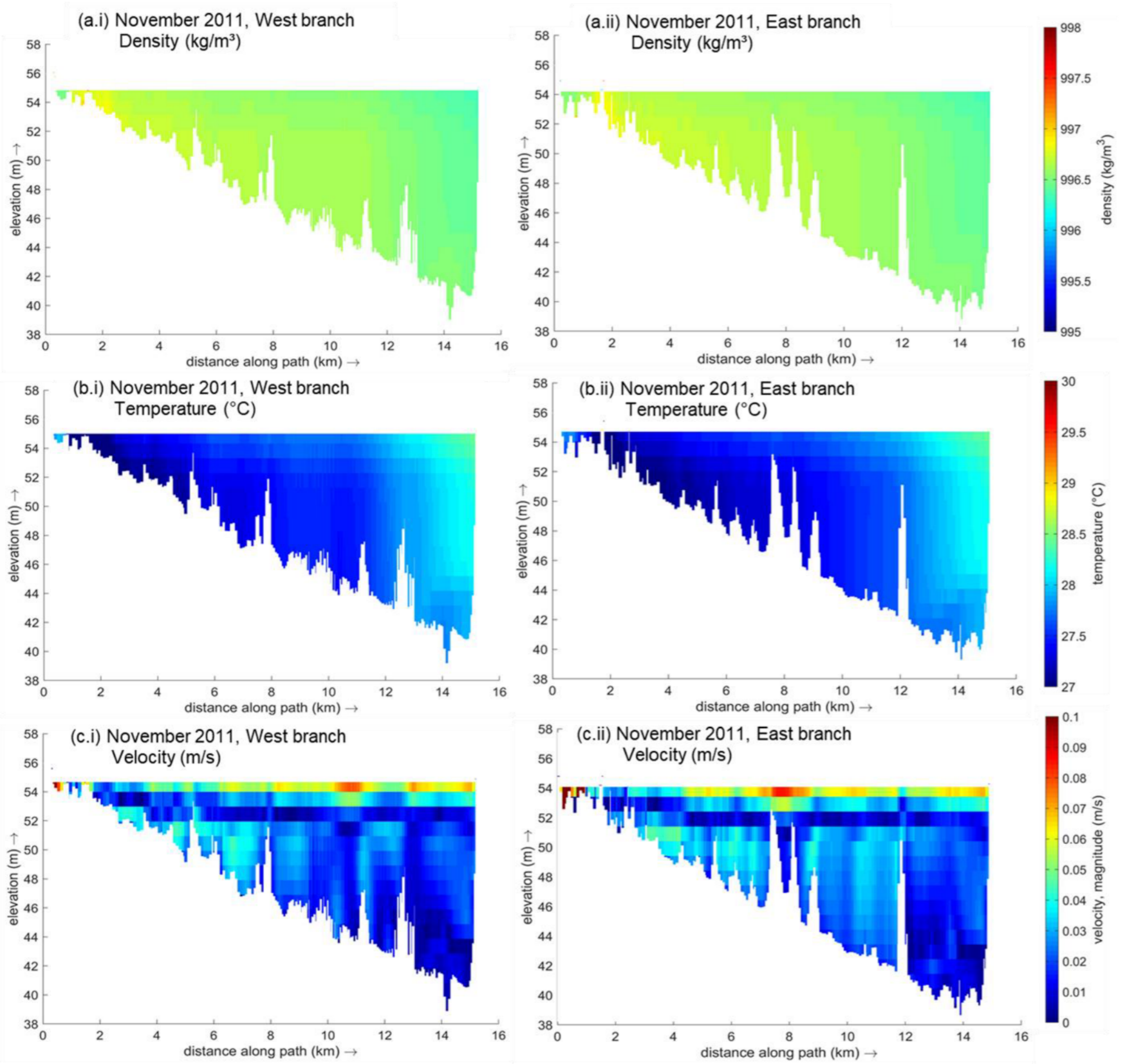

Figure A. 4 - Magnitude of water density, temperature, and velocity in a typical day of March, 2012 for (a.i), (b.i), (c.i) West and (a.ii), (b.ii), (c.ii) East branches

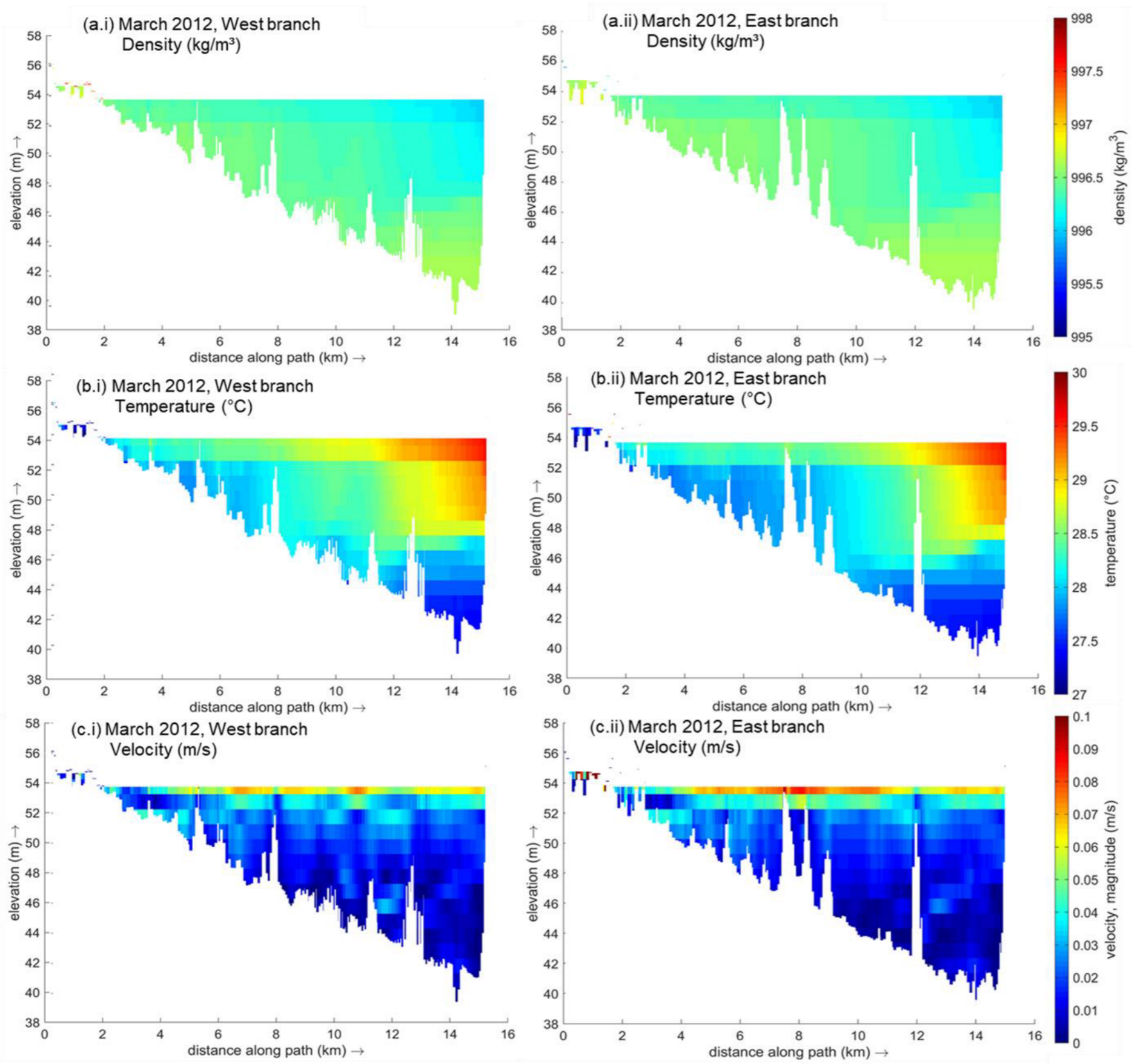

Figure A. 5 - Magnitude of water density, temperature, and velocity in a typical day of July, 2012 for (a.i), (b.i), (c.i) West and (a.ii), (b.ii), (c.ii) East branches

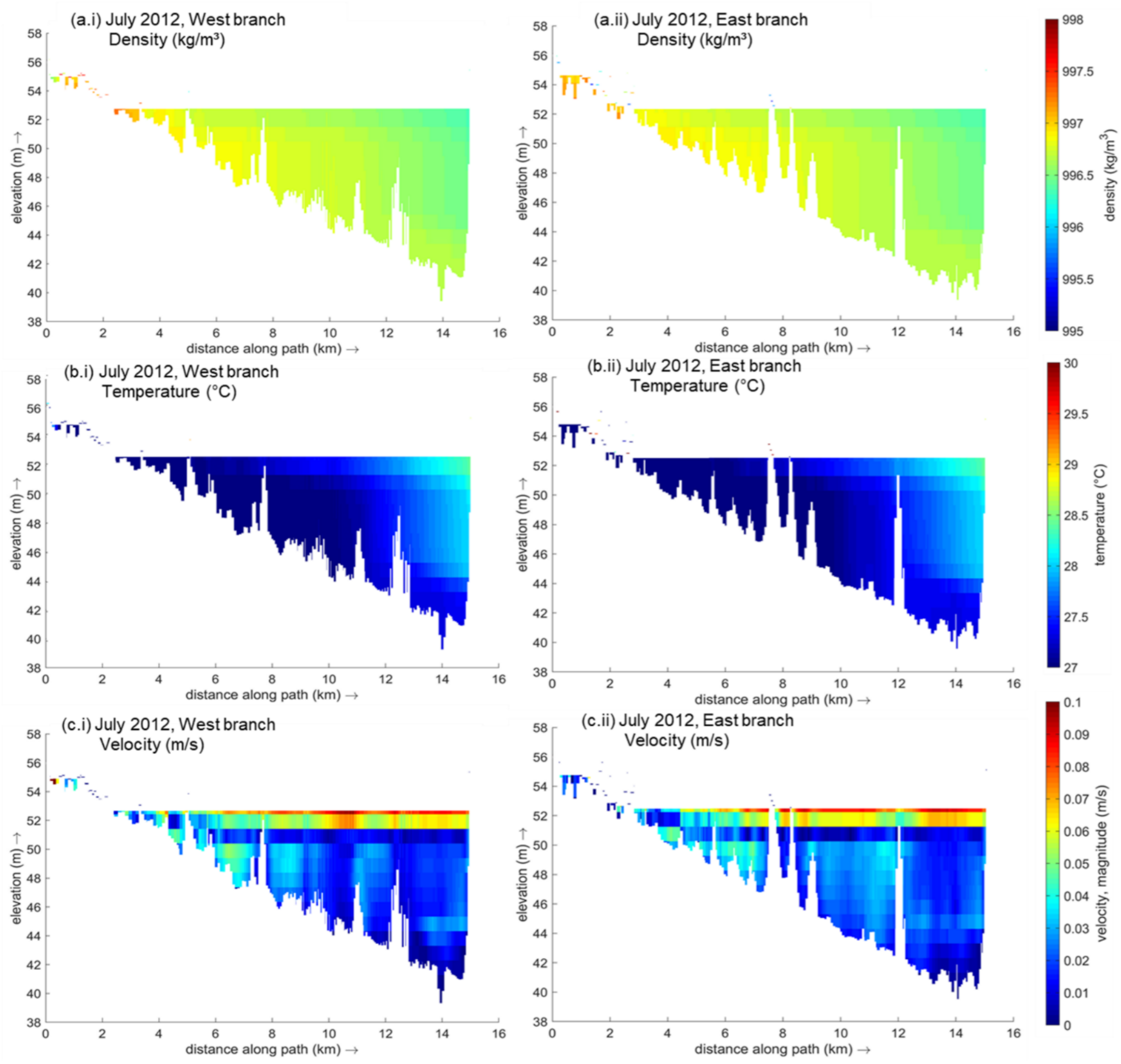

Figure A. 6 - Magnitude of water density, temperature, and velocity in a typical day of November, 2012 for (a.i), (b.i), (c.i) West and (a.ii), (b.ii), (c.ii) East branches

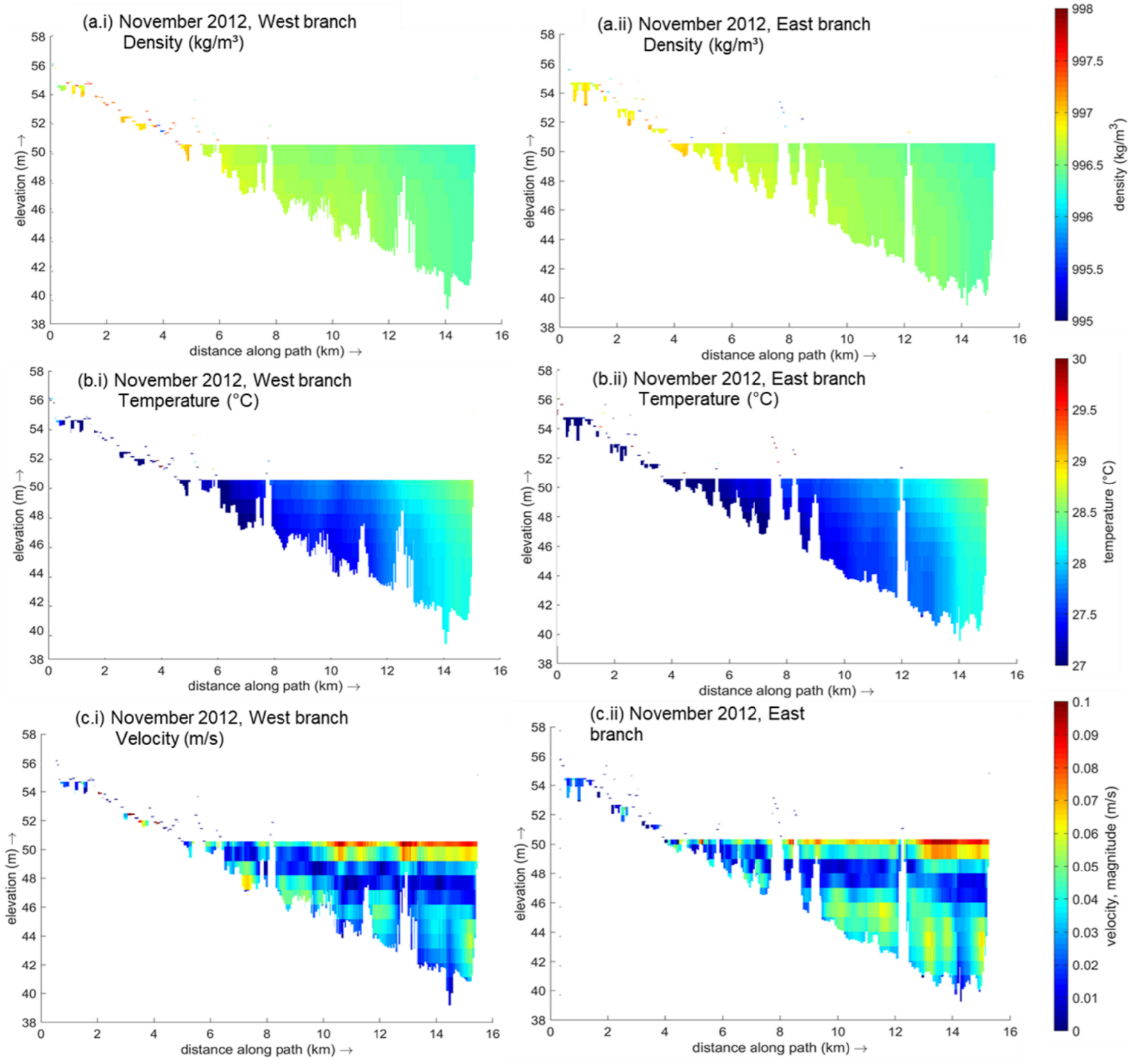

Figure A. 7 - Magnitude of water density, temperature, and velocity in a typical day of March, 2013 for (a.i), (b.i), (c.i) West and (a.ii), (b.ii), (c.ii) East branches

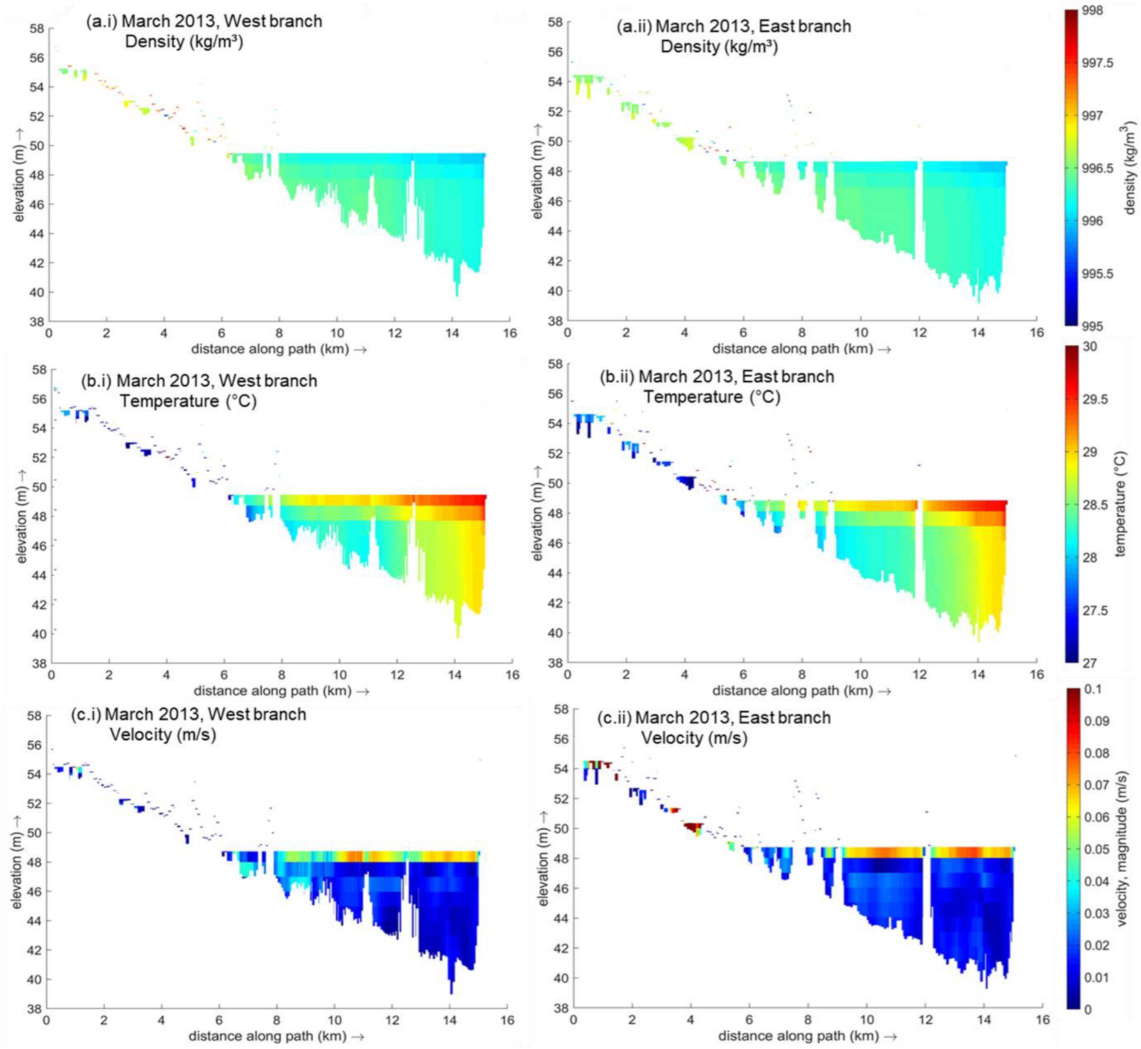

Figure A. 8 - Magnitude of water density, temperature, and velocity in a typical day of July, 2013 for (a.i), (b.i), (c.i) West and (a.ii), (b.ii), (c.ii) East branches